Unravelling the Matrix - On the Interplay of Microenvironment and Cellular Mechanoresponse

Die Matrix entschlüsseln - über das Zusammenspiel von Mikroumgebung und zellulärer Mechanoantwort

Zur Erlangung des akademischen Grades einer

Doktorin der Naturwissenschaften
(Dr. rer. nat.)

von der KIT-Fakultät für Chemie und Biowissenschaften
des Karlsruher Instituts für Technologie (KIT)

genehmigte

Dissertation

von

M. Sc. Magdalena Fladung

1. Referent:	Prof. Dr. Martin Bastmeyer
2. Referent:	Prof. Dr. Martin Wegener
Tag der mündlichen Prüfung:	6. Dezember 2024

Erklärung

Der experimentelle Teil der vorliegenden Arbeit wurde in der Zeit von April 2021 bis Oktober 2024 am Zoologischen Institut in der Abteilung für Zell- und Neurobiologie des Karlsruher Instituts für Technologie (KIT) durchgeführt.

Ich versichere hiermit, dass ich diese Arbeit selbstständig verfasst habe und keine anderen als die angegebenen Quellen und Hinweise verwendet habe. Wörtlich oder inhaltlich übernommene Stellen sind als solche gekennzeichnet und die Satzung des KITs zur Sicherung guter wissenschaftlicher Praxis habe ich in der gültigen Fassung beachtet. Diese Arbeit wurde in keiner Form einer anderen Prüfungsbehörde vorgelegt. Ich versichere außerdem, dass die beigelegte elektronische Version der Arbeit mit der schriftlichen übereinstimmt.

Karlsruhe, den _____

Datum, Unterschrift

Abstract

The microenvironment plays a crucial role in a multitude of different cellular processes such as polarisation, cell migration or embryonic development. As cells interact with their surroundings, they experience a variety of chemical or biophysical cues from the microenvironment. By now, numerous complexes involved in the mechanoresponse to the cellular microenvironment have been identified, including focal adhesions and the actomyosin network comprising actin fibres and non-muscle myosin II (NM II). On the microenvironmental side, substrate stiffness was broadly discussed in the past. However, biological tissues exhibit a range of material properties such as auxetic behaviour or viscoelasticity, which are rare or hard to recreate *in vitro*. Thus, accurately replicating various aspects of the cellular microenvironment remains a challenge.

Within this work, a novel approach to access rare material properties was explored. For this, a new material class termed metamaterials was employed, which results from altering mechanical properties of materials by appropriate microstructuring. Metamaterials with different Poisson's ratios and Young's moduli served as cell culture substrates during live cell imaging. From these timeseries, cellular forces were determined with unprecedented spatiotemporal resolution. Comparison of mesenchymal stem cells and fibroblasts revealed a different sensitivity to metamaterials, rooted in contractility-dependent stiffness sensing postulated by the molecular clutch model.
In the second part of this thesis, the effect of substrate micropatterning on cell morphology and polarisation was analysed. For this, aligned and random gelatine nanofibres were fabricated by electrospinning. To determine the ambiguously reported role of contractility in more detail, cells possessing a knock-out of NM IIA or NM IIB were subjected to these nanofibre substrates. In agreement with the inherently different dynamic properties of these isoforms, NM IIA was identified as the main driver of morphological adaptation whereas NM IIB regulated NM IIA activity to prevent overshooting responses. The effect on polarisation was assessed by Golgi apparatus localisation and morphology. Either knock-out led to altered Golgi apparatus morphology but only marginally affected localisation. Thus, while being dispensible for initiating polarisation, the interplay of both isoforms is needed to prevent dispersion or compaction of the Golgi apparatus. Additionally, the same analysis was conducted within commercially available parallel and orthogonal 3D collagen fibres. Here, the morphological effects of NM IIB KO appeared dampened and thus were partially compensated by the collagen fibre arrangement. On the other hand, polarisation was more sensitive to fibre orientation for both knock-outs, while wt cells behaved the same on either fibre substrate. These results imply a central role of NM IIA and NM IIB in regulating polarisation in 2D and 3D which goes beyond facilitating contractility.
In the last section, an experimental setup is presented to study the transition from mesenchymal to amoeboid migration under increasing confinement during live cell imaging.

Together, this thesis explored different approaches to analyse the cellular mechanoresponse to different aspects of the microenvironment, including the development of a novel metamaterial-based analysis of cellular force fields. Further, beyond providing contractility, NM II was characterised as a mediator of Golgi apparatus morphology and sensitivity to 3D environment organisation.

Zusammenfassung

Die Mikroumgebung beeinflusst maßgeblich zelluläre Prozesse wie Polarisation, Migration oder Embryonalentwicklung durch chemische und biophysikalische Reize. An der zellulären Mechanoantwort sind zahlreiche Komplexe beteiligt. Hierzu zählen Fokalkontakte oder das Aktomyosinnetzwerk, bestehend aus Aktinfasern sowie nicht-muskulärem Myosin II (NM II). Während der Einfluss von Substratsteifigkeit ausgiebig untersucht wurde, bleiben andere Materialeigenschaften biologischer Gewebe wie Auxetizität oder Viskoelastizität *in vitro* schwer nachzubilden. Die Modellierung solcher Aspekte stellt demnach bis heute eine Herausforderung dar.

In dieser Arbeit wurde ein neuartiger Ansatz zum Einbringen von seltenen Materialeigenschaften untersucht. Dieser nutzt sogenannte Metamaterialien, welche durch das Anpassen von Materialeigenschaften mittels Mikrostrukturierung gebildet werden. Metamaterialien mit unterschiedlichen Poissonzahlen oder Elastizitätsmoduli wurden als Kultursubstrate für Lebendzellmikroskopie verwendet. Zelluläre Kräfte wurden aus diesen Zeitreihen mit bisher unerreichter räumlich-zeitlicher Auflösung bestimmt. Der Vergleich von mesenchymalen Stammzellen mit Fibroblasten ergab eine unterschiedliche Sensitivität für Metamaterialien. Diese entsteht durch die kontraktilitätsabhängige Wahrnehmung der Substratsteifigkeit, wie vom "molecular clutch model" postuliert.
Im zweiten Teil dieser Thesis wurde der Einfluss von Substratmikrostrukturierung auf Zellmorphologie und -polarisation untersucht. Hierfür wurden ausgerichtete und zufällig verteilte Gelatine-Nanofasern mittels Elektrospinnen hergestellt. Um die umstrittene Rolle von Kontraktilität genauer zu bestimmen, wurden Zelllinien mit einem Knockout für NM IIA oder NM IIB auf diesen Substraten kultiviert. NM IIA wurde als Hauptregulator der morphologischen Adaptation identifiziert, während NM IIB vorwiegend dessen Aktivität reguliert. Der Einfluss auf die Zellpolarisation wurde anhand der Morphologie und Lokalisation des Golgi-Apparats bestimmt. Beide Knockouts führten zu einer veränderten Morphologie, beinflussten die Lokalisation allerdings nur marginal. Demnach ist das Zusammenspiel beider NM II-Isoformen essentiell, um Kompaktion oder Verteilung des Golgi-Apparats zu unterbinden, jedoch ist dieses nicht notwendig, um Polarisation zu initiieren. In kommerziellen parallelen und orthogonalen 3D-Kollagenfasernetzwerken zeigten sich die Effekte des NM IIB Knockouts nur abgeschwächt, welches auf eine Kompensation durch die Fasernetzwerke hindeutet. Die Zellpolarisation beider Knockout-Zelllinien war durch die unterschiedlichen Faserausrichtungen stärker betroffen, während Wildtypzellen keine Reaktion zeigten. Diese Ergebnisse implizieren eine zentrale Rolle von NM IIA und NM IIB in der Polarisationsregulation in 2D- und 3D-Umgebungen, die über Kontraktilität hinaus geht.
Im letzten Abschnitt wird ein Experimentsetup beschrieben, welches zur Untersuchung des Übergangs von mesenchymaler zu amoeboider Migration unter steigender räumlicher Begrenzung mittels Lebendzellmikroskopie eingesetzt werden kann.

Zusammenfassend werden in dieser Thesis unterschiedliche Ansätze zur Untersuchung der zellulären Mechanoantwort auf verschiedene Aspekte der Mikroumgebung präsentiert. Diese beinhalten die Entwicklung einer neuartigen Metamaterial-basierten Analyse zellulärer Kraftfelder. Weiterhin wurde für NM II eine zusätzliche Rolle als Mediator der Golgi-Morphologie sowie in der Regulation der Sensitivität für die Organisation von 3D-Umgebungen bestimmt.

Contents

Chapter 1

Introduction

In 1971, the psychologist B.F. Skinner described the influence of the environment on human nature as follows: 'A person does not act upon the world, the world acts upon him' (Skinner, 1971). While it is debatable whether this holds true to its full extent, one certainly can not deny that mankind is influenced by all kind of environmental factors. Indeed, even our cells are influenced by their environment as early as during embryonic development and continuously need to adapt to their microenvironment.

The cellular microenvironment comprises a mutitude of factors of biochemical and biophysical nature. On the biochemical side are a variety of small molecules, such as growth factors and proteins, which are part of the extracellular matrix (ECM). The ECM itself is a network of proteins like collagens or fibronectin, which provide binding sites for the attachment of cells. Apart from providing biochemical cues, the ECM can adopt different stiffnesses depending on the composition and density of the matrix, thus also modulating the biophysical environment. Both the biochemical and biophysical microenvironment were shown to affect the fate of stem cells, highlighting the importance of microenvironmental control in embryonic development (Engler et al., 2006; Lutolf et al., 2009). While the determination of stem cell fate is an impressive example of how the microenvironment can affect cells, microenvironmental factors also play a role in a multitude of other processes like cell polarisation and migration, proliferation or even remodelling of the ECM (Faurobert et al., 2015; Mierke, 2021; Rehfeldt et al., 2007). Although today it is widely accepted that not only biochemical but also biophysical factors can influence cell behaviour, the field of mechanobiology is still considered an emerging discipline. First clues on the biophysical control of cells were already published in 1917, but due to the lack of the technical methods only gained more attention towards the end of the 1900s (T. J. Kim, 2021). With the development of powerful techniques like atomic force microscopy or traction force microscopy, we now can characterise biophysical cues like matrix stiffness and measure cellular forces in response to them. While the role of matrix stiffness was and still is thoroughly investigated, the influence of other parameters, such as substrate geometry, dimensionality (2D and 3D culture) or other mechanical characteristics, only gained more attention in the recent years. This is partly due to technical advancements in manufacturing of structured substrates for cell culture and the availability of new materials to shape material properties to the desired needs.

With the rise of more flexible and advanced substrate designs, the experimental approaches became more diverse. Thus, quite a few mechanisms and models of cellular mechanosensing have

been discovered. In the following, a brief overview of the current understanding of how cells sense and react to their mechanical microenvironment is given, together with an introduction to fabrication techniques for substrates manipulating the cellular microenvironment.

1.1 Cellular Components

A variety of different proteins and complexes are involved in the cellular mechanoresponse. Amongst those are the actin cytoskeleton, providing a scaffold for contractile units; the motor protein non-muscle myosin II (NM II), which generates forces; and focal adhesions, anchoring the cell to a substrate and connecting the ECM to the cytoskeleton. As these components play central roles in the sensing, relaying and adaptation to mechanical stimuli, they are briefly introduced in the following.

1.1.1 Actin Cytoskeleton

The cytoskeleton comprises three different types of filamentous structures: microtubules, intermediate filaments and actin fibres. Of these three, actin fibres form the smallest filaments with a diameter of 7 nm, while being one of the most abundant proteins in eukaryotic cells (Desroches & Harris, 2023; Dominguez & Holmes, 2011). Globular actin monomers, so-called G-actin, polymerise in a non-covalent manner to form filamentous actin or F-actin. Such actin fibres exhibit a structural polarity, due to preferential polymerisation of adenosine triphosphate (ATP)-G-actin at the plus (or barbed) end. Simultaneously, bound actin monomers dissociate from the opposite end, referred to as minus (or pointed) end. This leads to a process called treadmilling, in which actin fibres grow fast at the plus-end while slowly depolymerising at the minus-end, resulting in overall growth of actin filaments (Dominguez & Holmes, 2011; Pollard, 1986). F-actin assembly is controlled by a variety of proteins like the actin-related protein (Arp)2/3 complex, acting as a nucleation site, or formins, enhancing polymerisation at the plus-end (Lappalainen et al., 2022). Contrary to that, capping proteins compete with G-actin polymerisation, thus efficiently blocking filament growth upon binding (Edwards et al., 2014). One of the key regulators of actin polymerisation and depolymerisation is the Rho-signalling pathway. By activation of downstream effectors *via* Rho-associated coil kinase (ROCK), actin-binding proteins associated with depolymerisation, such as cofilin, are inhibited, thus blocking actin depolymerisation and stabilising the formed actin network (T. Lin et al., 2003; Maekawa et al., 1999).
Over time, the individual actin filaments are connected by crosslinking proteins like α-actinin or NM II, forming a defined network rather than branched actin filaments. The latter are found in regions of high actin turnover such as the lamellipodium at the cell periphery, whereas the lamellum exhibits more defined actin bundles (Tojkander et al., 2012). Thick bundles of α-actinin-crosslinked actin filaments are referred to as stress fibres, which can be divided in dorsal or ventral stress fibres and transverse arcs, depending on their location (Pellegrin & Mellor, 2007). Actin filaments contribute to intracellular forces in two ways: they either directly push outward against the cell membrane during controlled polymerisation, leading to protrusion of the membrane, or

enable contractility in the form of stress fibres due to the associated NM II units. Thus, especially the actomyosin network plays a central role in the cellular mechanoresponse.

1.1.2 Non-Muscle Myosin II

The motorprotein NM II can exert forces on actin fibres which generates the necessary contractility for a variety of cellular processes. Amongst those are the stabilisation of leading edge protrusions and retraction of the cell rear in cell migration, mediation of contractility in cytokinesis and influencing cell morphology by regulating actin organisation (Cai et al., 2010; Conti & Adelstein, 2008; Sato et al., 2020; Shutova et al., 2017; Yamamoto et al., 2019). Furthermore, it plays a central role in embryogenesis, during which NM II mediates proliferation and supports spatial organisation of cells (Ladoux & Mège, 2017; Vogel & Sheetz, 2006; Zenker et al., 2018). Due to its crucial role in establishing cellular forces, defects in NM II are associated with a vast number of diseases, such as Alzheimer's disease, atherosclerosis or cancer (Newell-Litwa et al., 2015).

Structure and Organisation

The functional units of NM II proteins are hexamers and comprise two heavy chains (HCs), two essential light chains (ELCs) and two regulatory light chains (RLCs) as depicted in Figure 1.1. In mammals, three isoforms exist, namely non-muscle myosin IIA (NM IIA), non-muscle myosin IIB (NM IIB) and non-muscle myosin IIC (NM IIC). Whereas the light chains are similar, the heavy chains are different for each isoform but follow the same structure. The heavy chains possess a conserved N-terminal motor-domain with ATPase-activity divided into a globular head region, which binds to F-actin, and a hinge or neck region, associated with both light chains. The C-terminal α-helical rod domain provides a dimerisation site for the second HC, forming a coiled-coil structure (Vicente-Manzanares et al., 2009). The coiled-coil structure is followed by a non-helical tailpiece (NHT), which exhibits a high divergence between isoforms, and together with the assembly competent domains (ACDs) along the rod domain plays a regulatory role in the formation of higher order NM II units (Dulyaninova & Bresnick, 2013; Nakasawa et al., 2005; Shutova & Svitkina, 2018; Vicente-Manzanares et al., 2009).

Such higher order units are formed from stacks of NM II hexamers and are called minifilaments. These stacks are formed by parallel and anti-parallel interactions of the rod domains, leading to the formation of bipolar filaments with head groups located on either side. Minifilaments can either comprise one isoform, thus being homotypic, or different isoforms, referred to as heterotypic. Homotypic NM IIA and NM IIB minifilaments can contain up to 30 molecules, whereas NM IIC minifilaments do not exceed 14 molecules (Billington et al., 2013; Niederman & Pollard, 1975). All three isoforms additionally assemble into heterotypic minifilaments, which are less well characterised and their potential combinations are not yet fully determined (Beach et al., 2014; Shutova et al., 2014). As NM IIC still remains largely uncharacterised, in the following only the two main isoforms NM IIA and NM IIB are discussed. From here on, the term NM II refers only to these two isoforms.

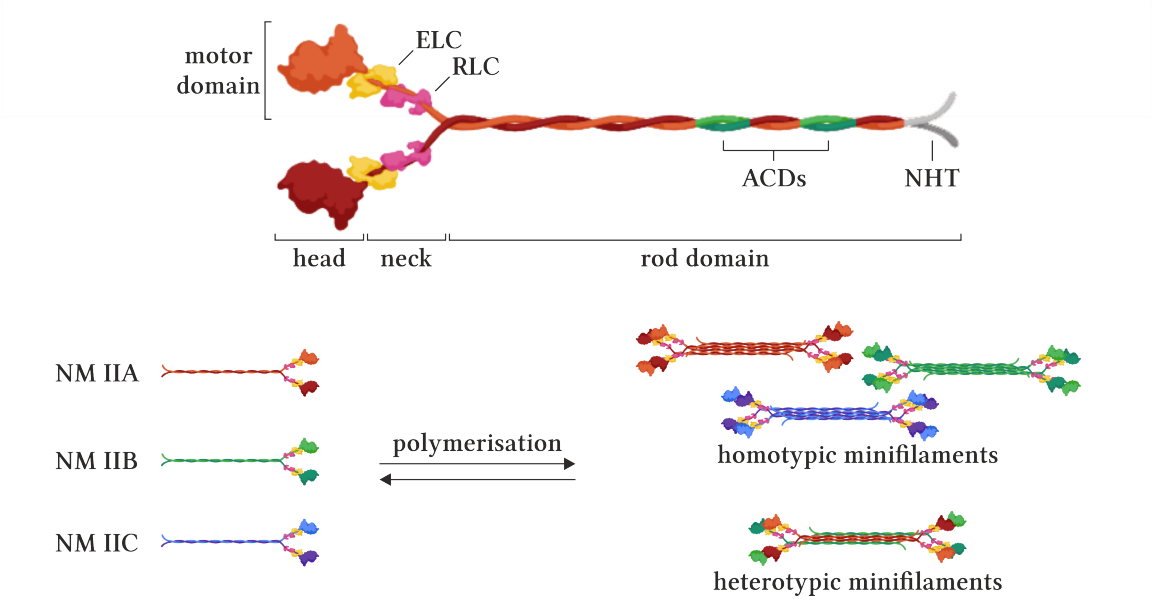

Figure 1.1: Structure of NM II hexamers and minifilaments.
The NM II hexamer comprises two HCs, two ELCs and two RLCs. The N-termini of the two HCs form globular head domains with ATPase activity, followed by flexible neck regions onto which the four light chains can bind. The complex of head and neck domain together with the light chains is commonly referred to as the motor domain. The rod domain is formed by both HCs which dimerise into a coiled-coil helical structure. The rod domain acts as an interaction site for other rod domains and possesses two ACDs and a NHT, which take on regulatory functions in minifimalent formation. The three NM II isoforms can polymerise into homotypic minifilaments, containing only hexamers of one isoform, or heterotypic minifilaments, comprising different isoforms. Created with BioRender.com.

The Myosin Cross-Bridge Cycle

In order to generate forces, NM II molecules hydrolyse ATP which provides the driving force for conformational changes and the so called powerstroke, during which force is exerted on the actin filament. This cross-bridge cycle is schematically depicted in Figure 1.2.
In the initial nucleotide-free rigor conformation, the head domain is tightly bound to F-actin. Once ATP binds to the corresponding binding site, the affinity for F-actin is lowered leading to release of the filament. After release of the filament, ATP is hydrolised into adenosine diphosphate (ADP) and P_i and a conformational change moves the head domain to a position further down the actin filament. In the ADP-bound state, the affinity for F-actin is increased, resulting in binding to actin fibres. During the powerstroke, the motor domain reverts to the initial rigor conformation. In doing so, the myosin pulls on the bound actin fibre, pushing it backward (Hwang & Lang, 2009; Vale & Milligan, 2000). Thus, myosins can exert forces on actin fibres. Repeated execution of this cycle results in the so called retrograde actin flow, which is directed towards the cell center, opposite to the polymerisation of actin directed against the cell membrane (C. H. Lin et al., 1996).

Kinetics and Intracellular Distribution of NM IIA and NM IIB

The kinetic properties of NM II can be described by the duty ratio and ATPase rate. The former describes the proportional time NM II stays attached to F-actin, whereas the ATPase rate deter-

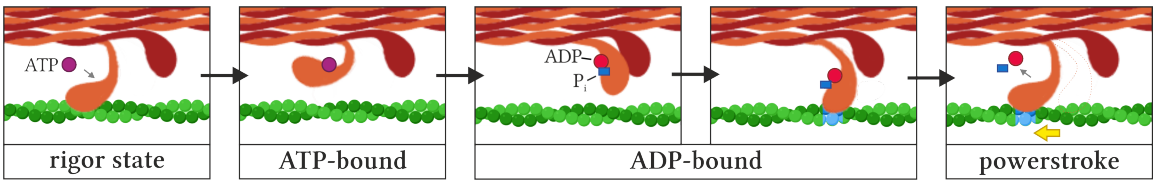

Figure 1.2: Myosin cross-bridge cycle.
In the nucleotide-free rigor state, the head domain is bound to actin. Upon ATP-binding, the head detaches and undergoes a conformational change, moving the head further up the actin fibre. In this process, ATP is hydrolised, resulting in an ADP-bound state. In this state, binding to actin is facilitated by an increased affinity for F-actin. This is followed by the powerstroke, during which forces are exerted on the actin fibre and ADP and P_i are released. For better visualisation, the binding position on actin is highlighted in blue. Created with BioRender.com.

mines the ATP turnover and thus motor activity. Although the heavy chain sequences of the three isoforms exhibit over 80% similarity, they differ in these kinetic properties (Golomb et al., 2004). NM IIA is characterised by its high ATPase rate and low duty ratio, resulting in fast initiation of the powerstroke cycle and high turnover rates (Kovács et al., 2003; F. Wang et al., 2000). NM IIB on the other hand exhibits a high affinity for ADP and thus a high duty ratio. Together with the low ATPase rate, this allows NM IIB molecules to maintain mechanical forces on longlived actin fibres (Rosenfeld et al., 2003; F. Wang et al., 2003).
Regarding the formation of minifilaments, both isoforms exhibit the same integration rates as these are determined by the highly conserved ACDs. Yet, in fluorescence recovery after photobleaching (FRAP) experiments, NM IIA molecules show faster recovery rates and higher mobile fractions than NM IIB (Weißenbruch et al., 2022). In addition to the individual dynamics, this difference in turnover was attributed to altered dissociation rates from minifilaments, facilitated by the highly divergent C-terminal NHT domains of the isoforms (Breckenridge et al., 2009).
These differences in overall dynamics result in isoform-specific distributions of NM IIA and NM IIB. While they are equally distributed within *de novo* assembled actomyosin networks, over time NM IIB gets enriched in the central or posterior region of the cell, depending on its polarisation state. For NM IIA, a uniform distribution within the cell is found (Kolega, 2003; Maupin et al., 1994). In 2017, Shutova and colleagues postulated a self-sorting mechanism based on monomer availability and turnover rates, which leads to this distinct distribution (Shutova et al., 2017). In newly assembled minifilaments, both isoforms are incorporated at the same rates. Due to the longer retention period of NM IIB within minifilaments, over time the minifilaments are enriched in NM IIB, which simultaneously depletes the pool of available NM IIB hexamers. Thus, together with the inherently higher turnover of NM IIA, newly formed minifilaments are enriched in NM IIA due to its higher availability. This leads to the distinctly different distribution of the isoforms, following the retrograde actin flow.

1.1.3 Focal Adhesions

Focal adhesions are protein complexes which comprise a multitude of components. They do not only mechanically anchor the cell to the substrate, but act as signalling platforms which relay extracellular stimuli to the cell interior. Over 150 different proteins were reported to associate

with focal adhesions, stressing their function as signalling platforms (Kuo et al., 2011). The bridging of extracellular and intracellular space is mainly facilitated by a class of heterodimeric transmembrane proteins called integrins. Within focal adhesions, the extracellular domain of integrins binds to the ECM *via* different binding motifs such as RGD or LDV, found along many ECM components like fibronectin or collagen (Pang et al., 2023). On the intracellular side, they exhibit binding sites for scaffolding and signalling proteins. In the context of mechanobiology, especially the scaffold proteins talin, vinculin and paxillin are often mentioned. Talin possesses a protein 4.1, ezrin, radixin and moesin (FERM) domain for binding to integrins and connects them to the actin cytoskeleton. Upon application of tensile forces, up to 13 binding sites for vinculin are exposed with increasing forces (Hytönen & Wehrle-Haller, 2016). This characteristic renders talin a mechanosensitive protein, taking a role in sensing of mechanical aspects of the cellular environment, such as substrate stiffness. Vinculin itself can bind to F-actin and is tightly associated with focal adhesion stabilisation and maturation (Humphries et al., 2007). Other binding partners include cyotskeletal components like α-actinin and Arp2/3 or focal adhesion components like paxillin (Carisey & Ballestrem, 2011). Despite its relatively small size of 68 kDa, paxillin contains a variety of binding sites for other proteins. It is subject to phosphorylation by tyrosine kinases activated upon integrin signalling, such as focal adhesion kinase (FAK). This phosphorylation creates SH2-binding sites for SH2-SH3 adaptor proteins or the non-receptor tyrosine kinase Csk, to name a few of the interacting partners. Further phosphorylations of serine and threonine residues were associated with mitogen-activated protein kinase (MAPK) activation. Together with its linkage to Rho-signalling *via* PKL, paxillin demonstrates the important role of focal adhesion components in intracellular signalling (Turner, 2000).

1.2 Cellular Mechanotransduction

The term mechanotransduction refers to the translation of mechanical stimuli into intracellular signals. In general, the signal transduction can be divided into reception of the extracellular signal, its transduction *via* intracellular signalling, which induces an according cellular response, and ending the signalling. In the case of mechanotransduction, the extracellular signal takes the form of a mechanical stimulus, rather than a biochemical signalling molecule. Within the past decades, the role of the mechanical microenvironment in processes like cell migration, remodelling of the ECM or even differentiation of stem cells was brought to attention and remains a focus of current research. The following section provides a brief insight into mechanisms involved in sensing, adapting and reacting to such mechanical stimuli.

1.2.1 Mechanosensing and Signal Transduction at Focal Adhesions

The high complexity of focal adhesion complexes is reflected in the multitude of signalling events in which they play a role. One of the most prominent and earliest identified signalling proteins is FAK, which is activated upon binding to focal adhesion complexes. In its active form, FAK can bind to other kinases like Src. This complex facilitates phosphorylation of p130Cas or paxillin, both associated with the regulation of cell migration *via* their downstream effectors (Turner, 2000; X.

Zhao & Guan, 2011).

In addition to activation of signalling pathways, focal adhesions can transfer mechanical stimuli to the cell interior. This is facilitated by mechanosensitive proteins like talin. In 2014, Yao and colleagues identified a positive feedback mechanism based on their characterisation of talin-vinculin-interactions which is described in the following (Yao et al., 2014). Talin binds to the intracellular domain of integrins *via* its FERM domain and connects them to the actin cytoskeleton. Due to the actin retrograde flow, the integrin is brought into an active form by tensile forces which leads to binding to the ECM. This anchoring to the ECM in turn increases the tensional forces, strengthening the integrin-ECM binding in a catch-bond manner and unfolding mechanosensitive domains of talin revealing binding sites for other adhesion proteins such as vinculin. Vinculin itself can bind to a variety of other proteins, such as actin and paxillin. In this scaffolding function, vinculin is involved in force transmission and clustering of integrins. This positive feedback, e.g. further unfolding of talin which leads to increased recruitment of scaffolding proteins and thus clustering of integrins, leads to maturation of focal adhesions in a force-dependent manner. Above a force threshold of roughly 25 pN at the adhesion site, this positive feedback is terminated by a helix-to-coil transition of talin, leading to displacement of vinculin. Beyond this point, no further maturation of the adhesion is observed. The mechanism is schematically depicted in Figure 1.3.

From these mechanisms it is apparent that the tensile forces needed for focal adhesion maturation and signalling are influenced mainly by two factors: the resistance of the ECM in the extracellular lumen and the contractility of the actomyosin network within the cell (Hytönen & Wehrle-Haller, 2016). The generation and regulation of the latter is addressed in the next section.

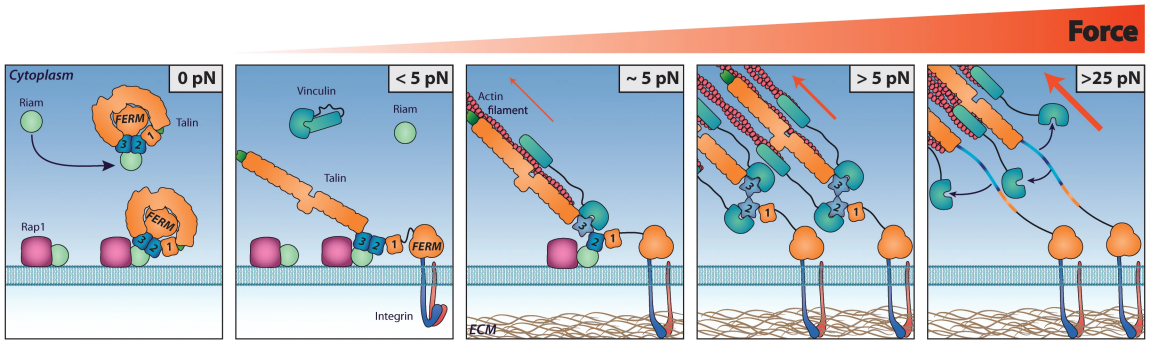

Figure 1.3: Mechanosensing at focal adhesions (Yao et al., 2014).
Talin connects integrins to the actin cytoskeleton, leading to activation of the integrin by forces generated by the retrograde actin flow. This facilitates binding of the integrin to the ECM, further increasing tensile forces. This leads to unfolding of mechanosensitive domains of talin, allowing for recruitment of vinculin to the focal adhesion complex. Vinculin itself possesses binding sites for actin and other focal adhesion proteins, further stabilising the focal adhesion until fully matured. Above a tensional threshold of 25 pN, talin undergoes a helix-to-coil transition, resulting in displacement of vinculin, thus terminating the positive feedback of increasing force.

1.2.2 Generation of Cellular Contractility

Following the sensing of the mechanical microenvironment, cells can generate intracellular forces to counteract these stimuli or even reshape their environment. While focal adhesions anchor a cell

to a substrate to withstand for example stretch or shear flow, cells can actively contract to counteract or overcome such stimuli. This cellular contractility is mainly exerted by the actomyosin network, with NM II minifilaments as active contractile units. Their regulation and the dedicated roles of NM IIA and NM IIB are described in the following.

Activation of NM II-Mediated Contractiliy

Within the cell, NM II hexamers undergo a continuous circle of activation and inactivation, as depicted in Figure 1.4. In general, the hexamers can switch between an autoinhibitory 10S state and an assembly-competent 6S state. In the latter, hexamers can be incorporated into bipolar minifilaments, acting as contractile units of the actin cytoskeleton. By phosphorylation, this incorporation and activation can be reversed, leading to a return to the 10S conformation. Switching between the activated and inactivated state, as well as the turnover of minifilaments, is regulated by various phosphorylations, which are briefly described in the following.

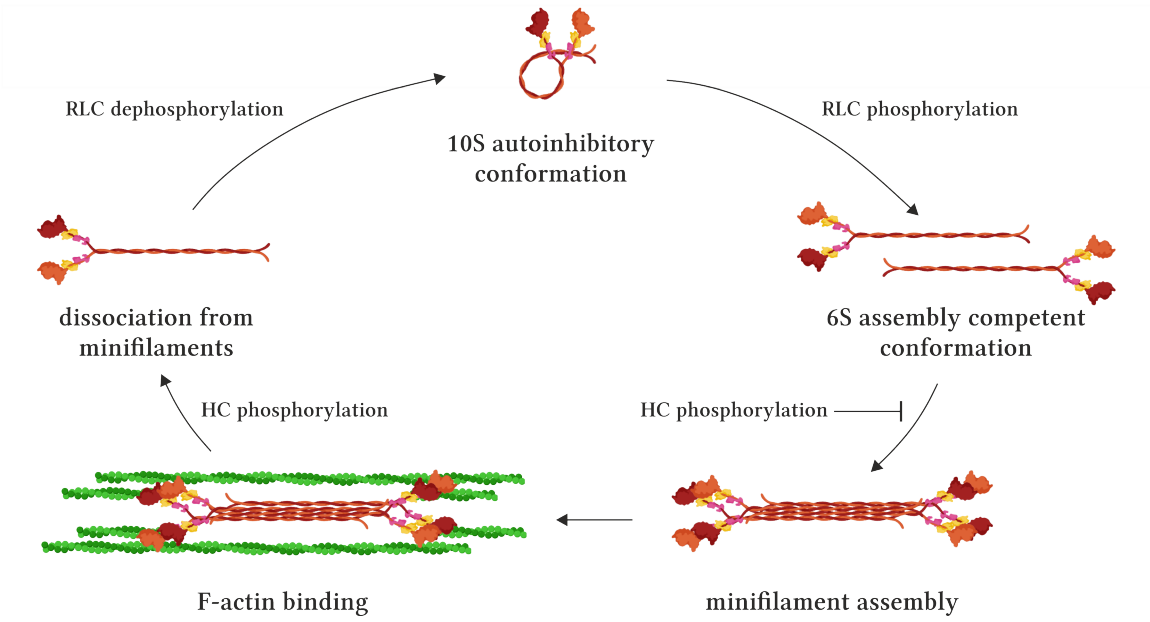

Figure 1.4: NM II activation and turnover.
Initially, NM II hexamers take a 10S autoinhibitory conformation. Upon phosphorylation of the RLCs, the rod domain is released, resulting in a transition to the 6S assembly-competent conformation. In this state, different NM II hexamers can polymerise into bipolar minifilaments. Minifilaments act as contractile units within the actin network, bundling F-actin into stress fibres and exerting forces on these fibres. Upon phosphorylation of isoform-specific residues on the HC, hexamers dissociate from the minifilament. This phosphorylation additionally inhibits incorporation into minifilaments. Upon dephosphorylation of the pRLC, the hexamer returns to the folded, autoinhibitory 10S conformation. Created with BioRender.com.

As indicated by their name, RLCs are regulators of NM II hexamers. When unphosporylated, they force the hexamer into a folded, inactive 10S conformation. This autoinhibition is resolved by Ser19 phosphorylation of the RLCs, leading to release of the rod domain and transition to the 6S conformation (Matsumura, 2005; Vicente-Manzanares et al., 2009). Additional phosphorylation of Thr18 leads to increased ATPase activity (Ikebe et al., 1988). As RLCs are conserved between the

individual NM II isoforms, this activation occurs in a isoform-independent manner. As solely the phosphorylation of Ser19 is sufficient for transition from 10S to 6S, this phosphorylation of RLCs is referred to as pRLC. Apart from activity regulation, pRLC formation plays a role in efficient NM II turnover and recycling. The two main kinases involved in the formation of pRLC are myosin light chain kinase (MLCK) and ROCK, which specifically phosphorylate the Ser19 residue (Amano et al., 1996; Heissler & Sellers, 2016; Ikebe & Hartshorne, 1985). Additionally, ROCK inhibits myosin light chain phosphatase (MLCP), thus preventing dephosphorylation of pRLC and hence inactivation of NM II by this phosphatase. Further, as ROCK is a central kinase in Rho-signalling, it is involved in cytoskelal remodelling events like stabilisation of the actin cytoskeleton. Thus, ROCK directly and passively enhances NM II activity, rendering it a potential key regulator of actomyosin derived contractility (Hwang & Lang, 2009; Totsukawa et al., 2000).
Following transition to the 6S conformation, hexamers can assemble into minifilaments which act as the contractile units in the actomyosin network. The incorporation and dissociation of individual hexamers is regulated by a variety of C-terminal phosphorylation sites and kinases. For NM IIA, phosphorylation of Ser1916 or Ser1943 by protein kinase C (PKC)β and casein kinase II (CKII), respectively, leads to disassembly of minifilaments or inhibition of their formation (Dulyaninova & Bresnick, 2013; Vicente-Manzanares et al., 2009). In case of NM IIB, phosphorylation of Ser1937 by PKCζ slows filament assembly (Even-Faitelson & Ravid, 2006). The different sites stem from differences in the HCs, thus, together with the aforementioned NHT domains, these phosphorylation sites facilitate isoform-specific regulation of activity and localisation.

NM IIA and NM IIB Mediate Different Aspects of Contractility

In 2021, Weißenbruch and colleagues further characterised the roles of NM IIA and NM IIB in generation of cellular forces in structured environments (Weißenbruch et al., 2021). They applied a dynamic tension-elasticity model to cells seeded on cross shaped pattern, from which they concluded the roles of NM IIA and NM IIB in maintaining tension. In their model, NM IIA acts as a highly dynamic regulator of tension, in agreement with its high turnover rate and low duty ratio, whereas NM IIB is necessary to elastically stabilise the generated tension.
Further, using a 3D microscaffold-based approach published by Hippler and colleagues, initial contractile forces of NM II knock-out (KO) cell lines were determined and their response to a mechanical stretch analysed (Hippler et al., 2020). The initial forces of NM IIA KO cells were close to zero, while NM IIB KO cells exhibited forces equal to the wildtype (wt). Even after repeated mechanical stretch, NM IIA KO cells failed to counteract the stretch by contraction, as observed for wt cells. As before, NM IIB KO showed a response similar to the wt. However, when cellular forces were calculated from these experiments and compared to initial forces, the increase in forces of NM IIB KO cells was significantly lower than for wt cells. As for the tension-elasticity models, these results highlight the role of NM IIA in initiating contractility, while NM IIB acts as a elastic stabiliser of forces on a longer time scale (Weißenbruch et al., 2021). This initiating role of NM IIA was further confirmed by dynamics studies published the year thereafter (Weißenbruch et al., 2022).
These different roles in generating and maintaining cellular forces are also reflected on the cellular

level. NM IIA knock-out leads to a drastic reduction of stress fibres and focal adhesions as well as an irregular morphology. Thus, this phenotype emphasizes the role of NM IIA in focal adhesion maturation, stress fibre formation and stabilisation of the cell shape (Sandquist et al., 2006; Vicente-Manzanares et al., 2007; Vicente-Manzanares et al., 2011). However, the phenotype can be partly rescued in a structured environment which provides guidance cues. For NM IIB knock out, only a slight disturbances of stress fibre and focal adhesion formation as well as cell shape are observed (Weißenbruch et al., 2021).

1.2.3 Control of Gene Expression *via* YAP/TAZ

In order to adapt to the altered microenvironment, gene expression can be altered upon sensing and relaying mechanical cues to the cellular interior. Two key effectors of this trancriptional regulation are the transcriptional co-activators Yes-associated protein (YAP) and transcriptional co-activator with PDZ-binding motif (TAZ). Despite being structurally different, both can bind to and accordingly activate transcriptional enhanced associated domain (TEAD) proteins which act as transcription factors for a multitude of genes. This is reflected in the numerous processes affected by TEAD-regulated gene expression, such as embryonic development, loss of contact inhibition or cell death (Fu et al., 2022; Panciera et al., 2017). In the past decade it has become clear that YAP and TAZ take on distinct roles in addition to their shared functions, summarised in detail in a review by Reggiani and colleagues (Reggiani et al., 2021). However, in the field of mechanobiology they are regarded as paralogs with congruent functions and thus will be used interchangeably in this work.
Corresponding to the key role of YAP/TAZ in a multitude of processes, they are targets of many different signalling pathways, but can also be activated solely through mechanical cues. Both the biochemical and mechanical activation are briefly described in the following.

Biochemical Regulation of YAP/TAZ

Probably the most prominent molecular regulator of YAP/TAZ activity is the Hippo pathway. This pathway is a known modulator of organ growth, proliferation, differentiation and cell survival, reflected in a variety of diseases associated with dysregulation of Hippo signalling (Kodaka & Hata, 2015; Panciera et al., 2017; Zanconato et al., 2015). The Hippo pathway inactivates YAP/TAZ by phosphorylation, leading to cytoplasmic retention of the transcriptional co-activators and thus inhibiting expression of associated target genes. In mammals, the phosphorylation is facilitated directly by large tumor suppressor (LATS) kinase, which in turn is activated by mammalian Ste20-like kinase (MST), the ortholog of the namegiving Hippo protein found in *Drosophila* (Dasgupta & McCollum, 2019). A simplified signalling cascade is depicted in Figure 1.5. Canonical signalling is induced by many different receptors and protein complexes located at the cell membrane, such as G-protein coupled receptors (GPCRs), E-cadherins or tight and adherens junctions (Low et al., 2014).

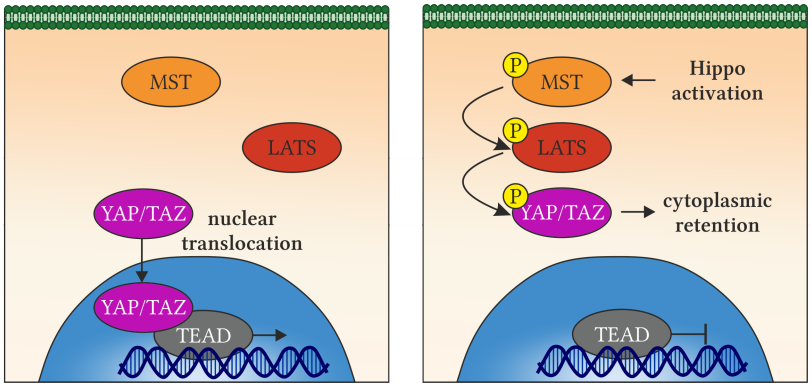

Figure 1.5: Schematic depiction of canonical Hippo signalling in mammalian cells.
When Hippo signalling is inactive, YAP/TAZ can freely translocate to the nucleus. There they bind to TEAD, which induces transcription of associated genes. Upon Hippo signalling activation, the mammalian Hippo ortholog MST is activated and in turn activates LATS. This kinase phosphorylates YAP/TAZ, which results in cytoplasmic retention and thus inhibition of gene expression.

Reflected in the variety of receptors and protein complexes associated with Hippo signalling, many different cues affect this pathway. A detailed overview of Hippo pathway activation was published in a review by Fu and colleagues in 2022 (Fu et al., 2022). Mechanical cues affecting the Hippo pathway and subsequently YAP/TAZ are as diverse as ECM stiffness, cell geometry, shear forces or cytoskeletal tension (Panciera et al., 2017). Especially the latter is known to be mediated by Rho-signalling, which plays a key role in NM II regulation, stressing the complex interplay of pathways in the cellular mechanoresponse. Unsurprisingly, the detailed molecular mechanism by which mechanical cues affect the Hippo pathway are yet to be fully understood.

Mechanoregulation of YAP/TAZ Localisation

In addition to regulation of YAP/TAZ by different signalling pathways, translocation of these transcriptional co-activators is regulated by mechanical cues. Within confluent cell layers, Hippo signalling is activated to regulate contact inhibition. Yet, Pathak and colleagues could demonstrate that YAP/TAZ localised to the nucleus upon stretch of the cell layer, indicating a Hippo-independent regulation of the transcriptional co-activators (Pathak et al., 2014). In 2017, Elosegui-Artola and colleagues investigated a force-based mechanism of YAP/TAZ nuclear translocation *via* nuclear pores (Elosegui-Artola et al., 2017). They again demonstrated that mere force application is sufficient for the transcriptional co-activators to enter the nucleus. Due to the coupling of extra- and intracellular space through focal adhesions, for example substrate stiffness can be translated into cellular tension *via* F-actin. More precisely, above a stiffness threshold of 5 kPa, unfolding of talin by contractile forces of the actomyosin network leads to reinforcement of the actin cytoskeleton with stress fibres and subsequent nuclear localisation of YAP. However, lack of stress fibres upon deletion of talin or blockage of the linker of nucleoskeleton and cytoskeleton (LINC) complex, anchoring the cytoskeleton to the nuclear laminar, abrogated this effect. They proposed that this is due to the increase in cellular tension and thus flattening of the nucleus, resulting in the mechanical opening of nuclear pores. This allows the otherwise too large YAP/TAZ to enter

the nucleus and activate expression of target genes.
Due to this mechanoregulation of YAP/TAZ, their localisation emerged as an indicator for mechanical activation of cells. Further, this purely mechanical based mechanism of trancriptional regulation demonstrates how the interplay of the mechanical microenvironment affects cells on a molecular level.

1.2.4 Durotaxis and Cell Migration

Just like signalling molecules secreted by infected cells can guide immune cells to regions of infection, also the mechanical microenvironment can help cells navigate. This guidance of migration by mechanical cues is referred to as durotaxis and was first discovered in the year 2000: by using polyacrylamide sheets with discontinuing concentration of crosslinker and thus softer regions, Lo and colleagues found that fibroblast cells preferentially migrate towards stiffer regions and are susceptible to strains applied to the sheets (Lo et al., 2000). Since then, this durotactic behaviour was determined in many different cell types, including mesenchymal stem cells (MSCs), cancer cells or immune cells (Sunyer & Trepat, 2020). In some cases, even negative durotaxis, the preferential migration towards softer substrates, was observed (Huang et al., 2022; Isomursu et al., 2022). However, the precise mechanisms in which cells establish durotaxis is not fully understood to date, but some of the regulating influencers have been identified.
Due to their close proximity to the substrate and the function as mechanosensitive signalling platforms, different focal adhesion-associated proteins have been identified as key regulators of durotaxis (Ji & Huang, 2023; Plotnikov et al., 2012; Rens & Merks, 2020). This linkage was termed molecular clutch by Mitchison and Kirschner in 1988, analogous to shafts in a mechanical engine (Mitchison & Kirschner, 1988). The molecular clutch model proposes a model rooted in cell-ECM adhesion, NM II-based force generation and its transmission across the cytoskeleton and was comprehensively reviewed by several articles (Elosegui-Artola et al., 2018; Fortunato & Sunyer, 2022; Sunyer & Trepat, 2020). Due to the retrograde actin flow and the connection of the actin cytoskeleton to focal adhesions, cells experience inward facing forces on each adhesion site. Analogous to a skater holding onto an immobilised stiff and soft spring in either hand, when pulling on each of them with the same force, the skater will move towards the stiffer spring (Sunyer & Trepat, 2020). The same imbalance of forces occurs when cells migrate along a stiffness gradient: due to the higher resistance of the stiff surface at the leading edge and the larger retraction of the cell rear on the soft substrate, it experiences a net forward movement towards the stiffer region.
However, NM IIA and NM IIB exhibit different kinetic properties and intracellular distributions and thus affect migration and durotaxis in different ways. To name one example, durotaxis of MSCs was more sensitive to knock-down of NM IIB compared to NM IIA (Raab et al., 2012). The roles of both isforms in stiffness-dependent migration was addressed in several studies, which all observed distinct functions. To this end, NM IIA is believed to be an initiator of cell migration, involved in stabilisation of protrusions and initiation of minifilaments, while NM IIB takes on a role in establishing front-rear polarity and contributes to maintainance of traction forces (Kuragano et al., 2018; Peng et al., 2022; Shutova et al., 2017).

1.3 Adaptation to Substrate Organisation

Cells are not only susceptible to the mechanical properties of their microenvironment, but also react to the organisation of their surroundings. Already in 1997, Curtis and Wilkinson reviewed the effect of substrate topography on adaptation mechanisms like cell orientation or migration, adding to the discussion whether topography or the chemical environment guides cells (Curtis & Wilkinson, 1997). Roughly 10 years later in 2006, Théry and colleagues demonstrated an effect of substrate geometry on cell shape, polarisation and organisation of the actin cytoskeleton (Théry, Pépin, et al., 2006; Théry, Racine, et al., 2006). Again 10 years later, Fee and colleagues connected the orientation of fibroblast cells on gelatine nanofibres to expression of focal adhesion and actin-related genes (Fee et al., 2016). Only a few years ago, Leclech and colleagues demonstrated a topographical guidance of cortical neurons using a PDMS-pillar array (Leclech & Villard, 2020). While those are just a few examples, today various different publications on the interplay of cell orientation and substrate geometry are available. In general, the orientation of cells along topological features is referred to as contact guidance. When characterising topographic features, one can distinguish between isotropic (random) orientation and anisotropic (unequally distributed) orientation. *In vivo*, such anisotropic cues are provided for example by ordered fibre networks in the ECM or other cells, such as radial glia which guide cortical neurons (Casingal et al., 2022; Diller & Tabor, 2022; Teixeira et al., 2003). While individual cellular components affected by or involved in the adaptation to such networks have been identified, the detailed processes are not yet understood.

1.3.1 Underlying Mechanisms of Contact Guidance

A comprehensive review of how contact guidance is facilitated was published by Leclech and Barakat in 2021, which served as a guideline for this section (Leclech & Barakat, 2021).
One model, which aims at explaining alignment of cells to topological features, was published by Ray and colleagues in 2017 and is centred around focal adhesions (Ray et al., 2017). Essentially, the geometry of the substrate guides protrusions and spatially restricts focal adhesion formation. In the case of aligned fibres, focal adhesions and protrusions are formed along the fibres, restricting both in the orthogonal direction. This geometry-based sorting of focal adhesions results in increased formation of parallel actin stress fibres. The correlation between stress fibre organisation and substrate topography was experimentally demonstrated by culturing cells on substrates with switchable orientation, leading to re-orientation of their actin cytoskeleton once the substrate orientation was altered (Linke et al., 2019). The formation of highly parallel stress fibres leads to anisotropic cellular forces and tension, with contractility being directed along these stress fibres. This in turn generates compressive forces perpendicular to the fibre direction. Together with the spatial restriction of focal adhesions, this leads to orientation and elongation of the cell along the substrate. Whether focal adhesion formation or stress fibre alignment induce the cell orientation is yet to be determined. In any case, the importance of focal adhesion formation and their directional restriction was demonstrated by limiting focal adhesion size and culturing cells in grooves of varying width, respectively (Ray et al., 2017).

Despite these strong implications of focal adhesions as central sensors of substrate geometry, contact guidance is also present in cells with reduced focal adhesions, like neurons or amoeboid cells. As such, amoeboid-like T-cells, followed the direction of nanogrooves when apically confined, while also being able to exert adhesion based guidance (Kwon et al., 2012; Wolf et al., 2003). In case of leukocytes, the actin retrograde flow was shown to direct cell migration (Reversat et al., 2020). This implies the presence of further adhesion-independent mechanisms of contact guidance, between which cells can switch according to their needs.
Although NM II-mediated contractility is strongly intertwined with actin stress fibres, its role in contact guidance was ambiguously reported. While in some cases perturbation of actomyosin contractility affected cell orientation, other studies reported no such effects (Kubow et al., 2017; Lee et al., 2016; J. Wang & Schneider, 2017; Zhovmer et al., 2019). To date, if and how actomyosin contractility modulates cell orientation remains a topic of scientific discourse.

1.3.2 Excursus: Golgi Apparatus Localisation and Cell Polarisation

The guided orientation of cells is often accompanied by polarisation of the cell which is a key requirement for directional migration. In mesenchymally migrating cells, not only is the cytoskeleton polarised to create protusions at the leading edge and retract the cell body at the trailing edge, but also the Golgi apparatus was shown to take a distinct position towards the leading edge within migrating cells as depicted in Figure 1.6 (Ridley et al., 2003).

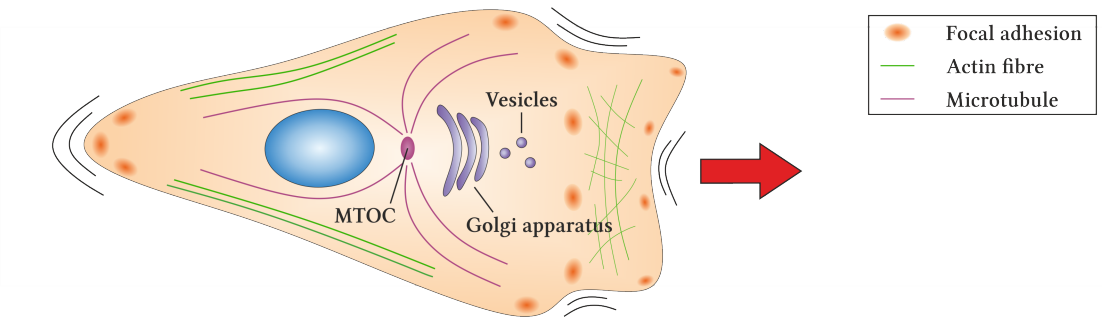

Figure 1.6: Localisation of Golgi apparatus in migrating cells. (adapted from Ridley et al., 2003)
Mesenchymally migrating cells establish a front-rear polarity in the direction of migration (red arrow). The leading edge exhibits enhanced actin polymerisation, leading to the formation of a branched network which pushes the cell membrane outward. Newly formed focal adhesions stabilise these membrane protrusions and act as anchoring points to pull the cell forward. The Golgi apparatus is located in front of the microtubule organising centre (MTOC) and nucleus, further helping with maintaining polarisation by delivering necessary components towards the leading edge by directed vesicle transport. At the trailing edge, matured focal adhesions and strong actin stress fibre bundles are present. The latter provide the contractility necessary to pull the cell rear forward once the focal adhesions are dissolved.

Interestingly, this positioning is affected by the substrate geometry. For example, cells on teardrop shapes localised their Golgi apparatus towards the blunt end which also acted as the preferred migratory direction (Jiang et al., 2005). Furthermore, cells cultured on fibronectin stripes showed a preferential localisation of the Golgi apparatus towards the trailing edge in dependency of stripe

width (Pouthas et al., 2008). In 2013, Chen and colleagues demonstrated that cell shape and spreading area dictate Golgi orientation as well as directionality of migration, which do not necessarily correspond. While Golgi orientation in front of the nucleas was true for prolonged migration, it does not determine front-rear polarity. Rather, the Golgi positioning is adapted to the migratory direction over time, resulting in the textbook orientation in front of the nucleus in direction of migration (Chen et al., 2013).
As the Golgi apparatus is a hub for vesicular transport, its positioning might play a role in maintaining and/or establishing polarisation by directing delivery of compounds to the respective cell end, thus providing spatial control (Yadav et al., 2009). The Golgi apparatus itself is linked to the cytoskeleton by adaptor proteins which connect the Golgi membrane to microtubules and actin filaments (Gurel et al., 2014; Ravichandran et al., 2020). Microtubules were shown to play a crucial role in assembling and orienting the Golgi apparatus. Further, in addition to the centrosome as main organiser of microtubules, the Golgi apparatus can act as a nucleation site for microtubules providing a network for directed vesicular transport (Rivero et al., 2009; Zhu & Kaverina, 2013). Indeed, this transportation network proved crucial for cell polarisation and polarised migration (Miller et al., 2009; Rivero et al., 2009). But also the actin cytoskeleton plays a role in Golgi apparatus organisation and *vice versa*. Perturbation of the actin network is associated with defects in Golgi apparatus localisation and morphology as well as retrograde Golgi-to-endoplasmatic reticulum vesicular transport (Di Campli et al., 1999; Valderrama et al., 1998; Valderrama et al., 2001). On the other hand, the presence of actin crosslinkers and Rho-GTPases at the Golgi apparatus implicate a close coupling of actin polymerisation and organisation as well as actomyosin contractility with the Golgi apparatus (Egea et al., 2013). Further, NM II was shown to play a role in actin-associated vesicular transport (Durán et al., 2003; Müsch et al., 1997; Valderrama et al., 2001).

1.3.3 Confinement in 3D

In addition to 2D substrate topography, the available overall space in 3D influences cellular behaviour. When migrating through dense fibre networks, cells may need to squeeze through tight pores. When confined in such a way, cells switch their mode of migration as demonstrated by Liu and colleagues in 2015 (Y. J. Liu et al., 2015). Upon confinement up to a degree where the nucleus appeared deformed and additional passivation of the surface, typically mesenchymal dermal fibroblasts adapted a mostly rounded morphology with continuous blebbing of the membrane. Further, a fraction of the hence confined cells started to migrate fast while exhibiting an amoeboid-like morphology. Following this observation, they subjected a total of 20 cell types to these conditions and found that nearly all of them were able to undergo such a transition to amoeboid-like migration. From this, they concluded that confinement and low adhesion are sufficient to induce a mesenchymal-to-amoeboid transition (MAT), leading to the observed change in migratory behaviour. A few years later in 2019, Holle and colleagues demonstrated that cancer cells entering narrow microchannels switch from mesenchymal, adhesion-dependent migration to a fast migration mode, exhibiting increased membrane-blebbing and a simultaneous reduction in focal adhesion and stress fibre formation (Holle et al., 2019). Their results indicate that in some

cases confinement alone can be enough to self-induce MAT.
Both experimental approaches impose conditions under which the cell nucleus is deformed. As the largest intracellular compartment, the nucleus limits the migration in dense spaces. In 2020, Lomakin and colleagues found that the nucleus not simply serves as a limiting factor in navigating dense networks but rather acts as an active mechanosensor of confinement (Lomakin et al., 2020). Depending on the tension along the nuclear envelope, for example increased due to confinement, stretch-sensitive proteins are activated, which in turn increase actomyosin contractility. They concluded that the nucleus serves as a 'ruler' for available space, inducing downstream effects upon reaching a certain threshold.
In all of these experiments, blebbing of the cell membrane was observed, which in terms of cell migration is associated with a certain type of amoeboid-like migration. The switch between membrane blebbing and formation of lamellipodia, as observed in mesenchymal migration, depends on the degree of NM II activation (Ghosh et al., 2021). Regarding the role of the individual isoforms in this, NM IIA was described to play a role in formation as well as retraction of blebbs, whereas overexpression of NM IIC favours formation of lamellipodia (Dey et al., 2017; Taneja & Burnette, 2019). Despite the overall role of NM II activity in adapting cell migration to environmental restrains like confinement being largely clear, specific functions of the individual isoforms in these processes are implicated but not yet fully understood.

1.4 Controlling the Cellular Environment

The majority of the findings described here were obtained by manipulation of the mechanical microenvironment of cells. Overall cell culture substrate properties like stiffness can be altered by varying the degree of crosslinking of hydrogels, to name one example (Giuseppe et al., 2018; Ishihara et al., 2023; Tirella et al., 2012). Using specialised fabrication methods, hydrogels with stiffness gradients can be fabricated to allow for a step-wise change of stiffness (Hakeem et al., 2023; Lavrentieva et al., 2020; Sunyer et al., 2012). Other approaches to alter stiffness take advantage of the correlation of bendability of columns and the effective stiffness. Shorter columns are harder to bend and thus exhibit a higher effective stiffness as experienced by cells. Thus, by fabricating column arrays of different height, gradients in stiffness can be obtained which additionally allow for precise control of adhesion geometry (Doss et al., 2020; Q. Li et al., 2015; Schoen et al., 2010). Such column arrays can be cast from moulds fabricated by techniques like UV lithography or reactive ion etching. Both offer the advantage of geometric control of the substrate and can also be employed to manufacture stamps for microcontact printing (Doss et al., 2020; Handrea-Dragan et al., 2022). This allows creation of 2D adhesive or passivating patterns by controlled application of surface coatings *via* microcontact printing and is used in studies focussing on geometric influences or impact of adhesive proteins on the cellular response (Bachmann et al., 2020; Lehnert et al., 2004).
Although all of these techniques allow generation of defined 2D or 2.5D substrates, generation of true 3D environments is harder to realise. With the development of 3D laser microprinting, another technique for fabrication of arbitrary 3D structures became available. This technique can be

employed to generate so-called bio-metamaterial scaffolds for cell culture, which exhibit altered material properties due to their microstructure (Flamourakis et al., 2020; Munding et al., 2023; C. Wang et al., 2022; W. Zhang et al., 2013). In the following, the underlying concepts of 3D laser microprinting and metamaterials are briefly introduced.

1.4.1 3D Laser Microprinting for Fabrication of 3D Environments

Modern 3D laser microprinting is based on the absorption of photons by a photosensitive resist, which subsequently induces polymerisation in a confined space, the voxel (Fischer & Wegener, 2013; Yang et al., 2019). Typically, femtosecond-pulsed lasers are used as a source of photons (LaFratta et al., 2007). By tightly focusing the laser beam into a liquid photoresist and moving the laser focus in 3D space, almost arbitrary 3D structures can be fabricated (Barner-Kowollik et al., 2017; Maruo et al., 1997). While the process of absorbing photons to initiate polymerisation appears simple, a fully 3D spatial control of the reaction is only possible due to the requirement of the simultaneous or step-wise absorption of two (or more) photons by the photoresist (Fischer & Wegener, 2013; Hahn et al., 2021). Early attempts of this two-photon polymerisation were already made in 1965, but only proved sucessful by the end of the 1900s due to the availability of powerful lasers and sensitive photoresists (Maruo et al., 1997; Pao & Rentzepis, 1965). Today, commercial setups together with a variety of photoresists are available, allowing for the fabrication of 3D scaffolds with geometries and material properties specifically tailored to the respective requirements.

Radical Polymerisation and Two-Photon Absorption

Although many different photoresists have been developed, they all contain a monomer and a photoinitiator, which creates radicals upon absorption of photons (Bagheri & Jin, 2019; J. Zhang & Xiao, 2018). In common photoresists, these radicals induce a chain reaction called radical polymerisation, which propagates until chain termination occurs (Decker & Jenkins, 1985; O'Halloran et al., 2023). Depending on the length of the obtained polymer chain, its solubility is decreased and it eventually solidifies. While the individual chains can form weak interactions with each other, they do not necessarily form a mechanically stable network. This can be solved by using monomers with more than one reactive group or the introduction of crosslinkers, which both lead to crosslinks between the individual polymer chains and thus a stable three-dimensional polymer network (Baldacchini, 2015).
One might wonder why two photons need to be absorbed to initiate the polymerisation, when radicals can also be formed by one-photon absorption (1PA). Two-photon absorption (2PA) is an unlikely process, which exhibits a probability proportional to the squared light intensity (Fischer & Wegener, 2013). This allows for precise spatial control of the polymerisation reaction, as polymerisation is restricted to the focal region of the laser, which exhibits the highest probability for 2PA. While the latter is also true for the way more common 1PA, here the probability of absorption is linearly proportional to the light intensity and thus still high outside of the focal point (Fischer & Wegener, 2013). The different absorption probabilities are depicted in a simplified scheme in Figure 1.7A.

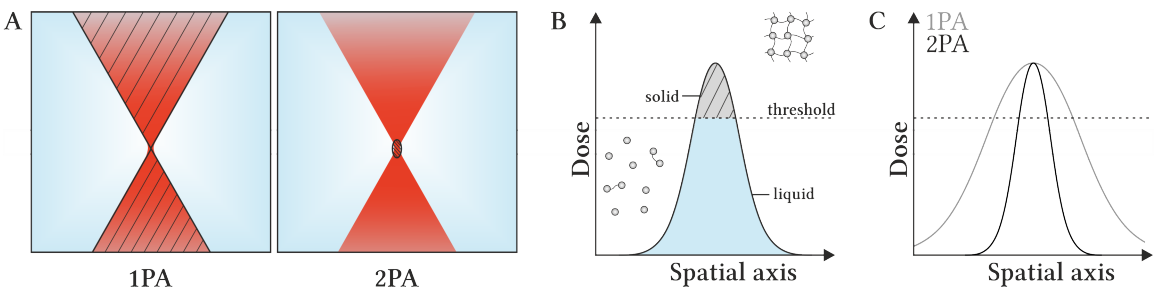

Figure 1.7: Schematic polymerisation behaviour 1PA and 2PA.
A Difference in photon absorption probability for 1PA and 2PA. For 1PA, the probability of photon absorption is high in the whole lightpath of the laser, with the highest probability at the focal region. Due to the nonlinearity of 2PA, the absorption probability is drastically decreased outside of the focal region. **B** Exposure dose and polymerisation. Below the threshold dose, the photoresist is not stably polymerised and crosslinked. When the exposure dose exceeds the threshold, the resulting polymerisation and crosslinking are sufficient to create a stable polymer network. **C** Schematic dose profiles of 2PA (black) and 1PA (grey). Due to its narrower profile, 2PA can achieve smaller polymerised features than 1PA for the same dose.

As the radical polymerisation is induced by light, the power and scan speed of the laser play a crucial role in regulating polymerisation and crosslinking density. Their respective proportionality to the dose, reflecting the amount of photons, is given in Equation 1.1 (Kiefer et al., 2020).

$$D \propto \frac{P^N}{v} \tag{1.1}$$

with D = dose, P = laser power, N = nonlinearity and v = scan speed.

According to the threshold model, a certain threshold dose is needed in order to obtain a stable polymer, which persists after removal of unpolymerised resist during development, visualised in Figure 1.7B (Kiefer et al., 2020). The dose profile for 1PA is comparably broader than the one for 2PA. Thus, while limiting polymerisation only to the focal area is also possible for 1PA when choosing a sufficiently small dose, 2PA can achieve smaller polymerised features for the same dose. The difference is schematically depicted in Figure 1.7C.

Feature Size and Resolution

Now that the basic principle of 3D laser microprinting is understood, the question arises what structures can be realised. Two characteristics indicating this are feature size and resolution. While feature size describes the smallest volume of structure that can be fabricated, resolution determines the smallest distance at which two features can be distinguished (or resolved) from each other. The feature size directly correlates with the voxel size, which is related to the exposure dose. In theory, the feature size can become infinitesimally small once an exposure dose is chosen whose maximum lies infinitesimally close to the polymerisation threshold. Resolution on the other hand is limited due to optical constraints. The resolution limit in lateral direction as formulated by Ernst Abbe and the adaptation to the axial direction are given in Equation 1.2 and Equation 1.3, respectively (Abbe, 1873; Fischer & Wegener, 2013).

$$d_{x,y} = \frac{\lambda}{2n\sin(\alpha)} = \frac{\lambda}{2\mathrm{NA}} \tag{1.2}$$

$$d_z = \frac{\lambda}{n - \sqrt{n^2 - \mathrm{NA}^2}} \tag{1.3}$$

with d = resolution limit, λ = wavelength, n = refractive index of medium, α = opening half angle and NA = numerical aperture.

From these equations it is apparent, that the axial resolution limit is at least doubled compared to the lateral one. Thus, the voxel takes an ellipsoid shape, elongated along the axial direction.
Another approach to describe resolution is the Sparrow's criterion. Here, two points are considered resolvable if they exhibit a local minimum. In case of 3D laser microprinting, this translates to a local minimum below the threshold dose. As mentioned above, the probability of 2PA is proportional to the squared light intensity, rendering it a non-linear process. This results in a narrower shape of dose profiles compared to the linear 1PA and hence an increase in resolution in the sense of Sparrow's criterion. To reflect this, the previously given Abbe's formulas need to be modified as given in Equation 1.4 and Equation 1.5 (Baldacchini, 2015).

$$d_{x,y} = \frac{1}{\sqrt{N}} \times \frac{\lambda}{2\mathrm{NA}} \tag{1.4}$$

$$d_z = \frac{1}{\sqrt{N}} \times \frac{\lambda}{n - \sqrt{n^2 - \mathrm{NA}^2}} \tag{1.5}$$

with N = nonlinearity.

For linear processes with $N = 1$, the original Abbe's formula is obtained. However, the 2PA in 3D laser microprinting leads to a factor $1/\sqrt{2}$ smaller resolution limit, as $N = 2$ for this process. In this work, all 3D laser microprinting was performed using a set up with an excitation wavelength $\lambda = 780\,\mathrm{nm}$ equipped with an objective with a $\mathrm{NA} = 1.4$ and photoresists exhibiting a refractive index around 1.5. According to the modified formulas, this results in lateral and axial resolutions of roughly 200 nm and 600 nm, respectively.
All of these considerations apply to 2PA as well as 1PA, which leads to the question why 2PA is considered superior in the context of 3D laser microprinting. When exposing points in close spatial proximity, their dose profiles overlap due to a phenomenon termed dose accumulation. According to the accumulation model, the total dose equals the sum of individual dose profiles, as the photoresist 'memorises' each exposure (Kiefer et al., 2020). Thus, even doses below the polymerisation threshold contribute to polymerisation. The consequence is schematically depicted in Figure 1.8. While the orange dose alone is not sufficient to cross the polymerisation threshold, the overlap with the blue dose results in a larger polymerisation area (green).
With this in mind, let's take a look at the implications for 1PA and 2PA, schematically depicted in Figure 1.8B and C, respectively. For 1PA, due to the linear correlation of dose with light intensity, the resulting dose profile is relatively broad. Thus, the effect of dose accumulation persists over a larger spatial distance than for 2PA with its smaller dose profiles. This results in polymerisation further away from the focal point, effectively reducing resolution by reducing minima below

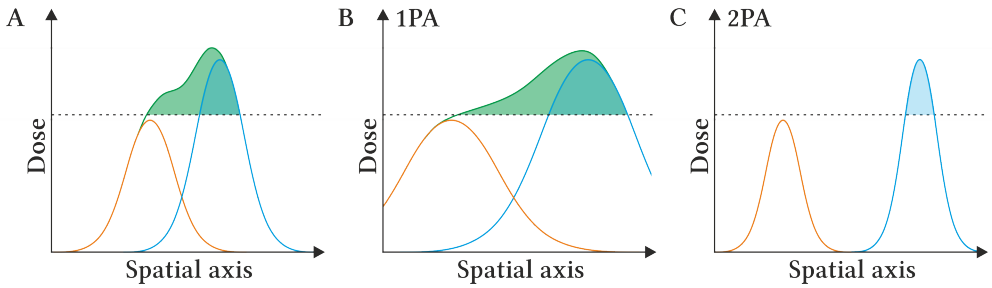

Figure 1.8: Dose accumulation during 1PA and 2PA.
A Exemplary dose accumulation for two spatially close doses. While the blue dose is sufficient to cross the polymerisation threshold, exposure with the orange dose alone does not yield a polymerised feature. However, due to the overlap of both doses, their combined doses lead to an increased polymerisation areal (green) according to the accumulation model. **B -C** Dosis accumulation for 1PA and 2PA, respectively. Although both doses are equally spatially separated, the dose profiles for 1PA overlap. This leads to accumulation of doses and a hence enlarged polymerisation areal (green). Due to the narrower dose profile of 2PA, both doses remain separated. Thus, 2PA enables higher spatial control compared to 1PA.

the polymerisation threshold. For 2PA, the overlap of dose profiles is comparably reduced, thus preserving the local minimum and achieving higher resolution.

1.4.2 Metamaterials Provide Access to Rare Material Properties

Apart from providing a detailed 3D architecture, 3D laser microprinted structures can also provide different mechanical properties. By using different photoresists and varying the degree of crosslinking, the stiffness of the obtained polymer can be influenced. However, the majority of photoresists produce rather stiff polymers. Due to the increased interest in 3D cell culture and mimicking the *in vivo* microenvironment, in the recent years more efforts have been made to develop softer photoresists for applications in tissue culture. By now, a few commercial and custom resists with lower stiffness are available (De Bellis et al., 2021; Ovsianikov et al., 2011; Vazquez-Martel et al., 2024).
Despite the multitude of available resists, the printed scaffolds are mostly stiffer than natural tissue and often exhibit swelling when transferred into aqueous environments, which interferes with the precise control of geometry. Further, to change the stiffness of the scaffold one needs to screen for other suitable photoresists and adapt the printing process to the new material which can turn into a tedious and time-consuming task. Only recently, a new material class which enables modifying material properties without actually changing the material itself became available. These so-called metamaterials exhibit an additional set of material properties based on their microstructure. While the above mentioned column arrays of different height in a sense can be considered metamaterials, another way to achieve metamaterial behaviour is to rationally design periodic patterns of unit cells and introduce this microstructuring to bulk materials, for example by 3D laser microprinting. Metamaterials find application in a variety of fields, as they can aim at different properties such as optical or acoustical behaviour. In the following, more insight into the field of mechanical metamaterials is provided, as the focus of this thesis is set on the mechanical microenvironment of cells.

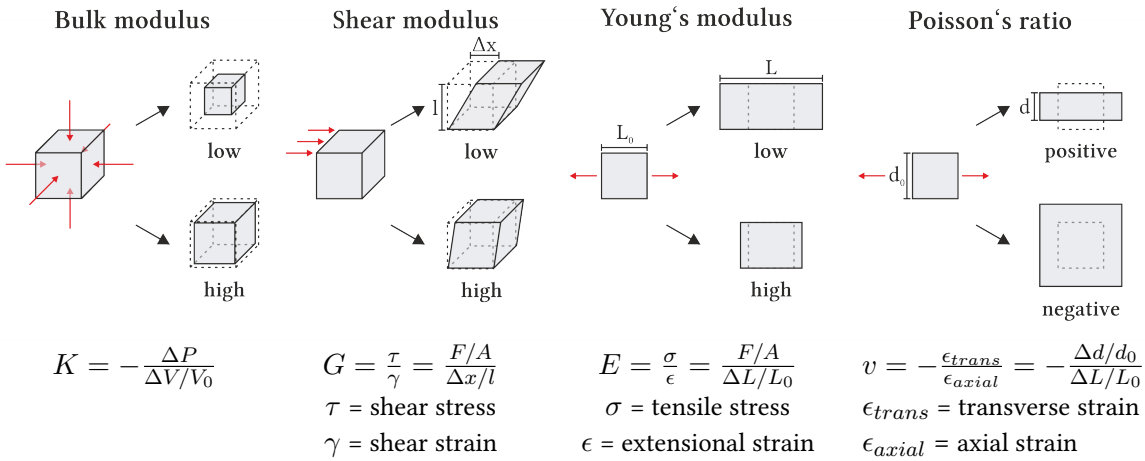

Figure 1.9: Schematical depiction of different descriptors of material properties.
Applied forces and initial geometries are indicated by red arrows and dotted lines, respectively. The bulk modulus acts as an indicator for compressibility, whereas the shear modulus describes deformability. Young's modulus and Poisson's ratio focus on the response to uniaxial stress. While the Young's modulus characterises the resistance to deformation in the axis of applied force, the Poisson's ratio gives a measure of the deformation perpendicular to the axis of stress. The corresponding mathematical descriptions are given below each visual representation, with ΔP = change in pressure, ΔV = change in volume, V_0 = initial volume, F = force, A = area parallel to applied force, $\Delta L = L - L_0$ and $\Delta d = d - d_0$.

For the ease of understanding, basic descriptors of mechanical material characteristics are given in Figure 1.9. The bulk and shear moduli serve as indicators of compressibility and deformability, respectively. The latter is calculated by the ratio of shear stress to shear strain, thus considering the force acting on a certain area and its lateral shearing. In case of the bulk modulus, the amount of pressure required to obtain a certain change in volume is calculated. Both descriptors are measured in Pascal. The Young's modulus is probably the most commonly cited material characteristic and describes the material's resistance along the axis of applied force. In biology, it is often used as an indicator of material stiffness. The Poisson's ratio on the other hand focuses on the relative deformation of the material perpendicular to the axis of applied force. Most materials exhibit a positive Poisson's ratio, resulting in thinning of the material under uniaxial stretch. However, a few biological tissues, like skin or tendons, were characterised to exhibit negative Poisson's ratio behaviour (Gatt et al., 2015; Lees et al., 1991).
Such so-called auxetic materials are relatively rare and thus harder to access for biological studies. Nonetheless, in the recent years attempts have been made to fabricate auxetic materials. In the context of cell culture, these materials were shown to affect processes like stem cell differentiation or cell alignment (Flamourakis et al., 2020; Yan et al., 2017). On a macroscopic scale, auxetic materials have been explored for medical applications, comprehensively reviewed by Lvov and colleagues (Lvov et al., 2022), and just recently were identified as candidates for more durable cardiac patches (Dong et al., 2024). All of these materials rely on a certain microstructure to obtain this auxetic behaviour and thus can be considered as metamaterials. How microstructuring can be applied to achieve e.g. auxetic behaviour by rational material design is schematically depicted in Figure 1.10.

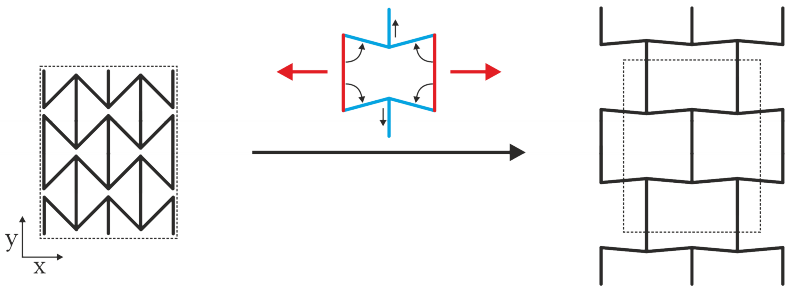

Figure 1.10: Schematic depiction of mechanics of an auxetic bowtie metamaterial.
When a bowtie unit cell is stretched along the x-axis as indicated by the red arrows, sides a (red) are pulled outwards. This leads to straightening of the angled sides b (blue), which in the process push out sides c (blue). This results in expansion of the material along the axis of stretch as well as the perpendicular direction. For better visualisation, the initial size of the material is indicated by dotted lines in the stretched version.

Granted that the bulk material, from which the metamaterial is fabricated, can be deformed by the applied force, the sides a are moved outwards. This leads to straightening of the sides b, which in turn push out side c. Thus, the individual unit cell expands perpendicular to the axis of stretch. As the metamaterial comprises a periodic pattern of these unit cells, the expansion is propagated throughout the material, leading to overall expansion and thus alters the bulk materials initial mechanical material characteristics. However, the metamaterial properties do not override the ones of the bulk material but rather are combined in the effective material properties.
In the last decade, a few publications explored such bowtie geometries for mechanobiological cell studies. They confirmed auxetic behaviour of their metamaterials and found that fibroblasts as well as MSCs were able to deform the structures, even in case of hard and stiff resists (Flamourakis et al., 2020; C. Wang et al., 2022; W. Zhang et al., 2013). This demonstrates, that metamaterials can be applied as powerful tools to access rare material properties, thus providing a new and interesting material class for shaping the cellular microenvironment.

Chapter 2

Aim of the Thesis

The influence of the cellular environment on many intracellular processes is a continuous topic of scientific discourse. The composition and organisation of the microenvironment influences a multitude of processes ranging from cellular contractility to embryonic environment (Rehfeldt et al., 2007; Tenney & Discher, 2009). Thus, alterations of the microenvironment have been associated with a wide range of diseases like cancer or fibrosis (de Visser & Joyce, 2023; Faurobert et al., 2015; Iozzo & Gubbiotti, 2018). To further the understanding on how the microenvironment regulates cell fate and behaviour, scientists are trying to recreate chemical and physical aspects of it *in vitro* to study the impact of individual parameters.

In order to understand the effect of different materials, physical material characteristics like the Young's modulus have been discussed broadly in the past (Discher et al., 2005; Janmey et al., 2020; Mao et al., 2016). Apart from the Young's modulus, the Poisson's ratio was identified as a promising new target for mechanobiological studies. Especially negative Poisson's ratio (or auxetic) materials were shown to influence stem cell differentiation (Yan et al., 2017). While some biological tissues can exhibit such auxetic behaviour, negative Poisson's ratio materials are relatively rare and thus harder to access (Gatt et al., 2015; Lees et al., 1991; Pagliara et al., 2014). Only recently, metamaterial-based approaches emerged to tackle this issue (Flamourakis et al., 2020; C. Wang et al., 2022; W. Zhang et al., 2013). By the use of such metamaterials, which exhibit an addtional set of parameters due to microstructuring of the bulk material, unusual mechanical behaviour, like auxeticity, can be achieved by rational material design. Thus, they pose a promising opportunity for studying the effect of defined material properties on the cellular mechanoresponse.

Although metamaterials primarily focus on generating new material properties, they may unintentionally influence cells by other means due to their design. As they rely on microstructuring, the effect of substrate geometry needs to be considered, as it can affect the orientation and polarisation of cells (Belay et al., 2023; Callens et al., 2020). How cells sense and adapt to the substrate geometry is not fully understood in detail, but a multitude of components are already identified. This encompasses sensory focal adhesion complexes, intracellular signalling cascades that transmit the received cues and ultimately parts of the contractile machinery, which facilitate parts of the cellular response. Belonging to the latter, the motorprotein NM II, of which three isoforms are decribed, is known to play a role in polarisation of cells. While inhibition of NM II causes defects in cell polarisation and migration, the role of individual isoforms in adaptation to different substrate organisations is yet unclear.

While substrates for studying the effect of geometry are often structured in 2D or comprise furrows or grooves, cells *in vivo* also need to navigate crowded 3D environments. However, with the advances in 3D scaffold fabrication and 3D culture techniques it became clear that cells not necessarily adapt to 3D networks in they same way they do to 2D substrates. This is partially due to the dense packing of ECM and other cells, both leading to confinement, which is not present in 2D. Confinement of cells was shown to affect cell migration, introducing a migration mode termed amoeboid migration in various cell types (Y. J. Liu et al., 2015). This migration mode occurs independent of cell adhesion and the formation of a pronounced actomyosin network, which both are crucial intracellular structures for adhesion-dependent mesenchymal migration dominating in non-confined spaces. However, both actin and NM II, which form the actomyosin network, appear to be necessary for transitioning from mesenchymal to amoeboid migration. As for the sensing of substrate organisation, whether individual NM II isoforms take on different functions in this process is not yet understood.

Within this work, the effect of the mechanical microenvironment on the cellular mechanoresponse is adressed in three approaches, focussing on the arisen research questions:

(i) A metamaterial-based system was developed for the extraction of cellular forces. This system was used to characterise the cellular mechanoresponse, supported by the analysis of biological markers.

(ii) To address the cellular response to substrate geometry with respect to NM II, 2D and 3D substrates with different organisation of gelatine or collagen fibres were employed. By the use of knock-out cell lines of the isoforms NM IIA and NM IIB, their role in adaptation to the substrates was analysed.

(iii) For studying the effect of increasing confinement, a microchannel-based approach based on the work of Holle and colleagues is presented (Holle et al., 2019). By monitoring migration of different NM II knock-out cell lines within these microchannels, conclusions on the role of the individual isoforms can be drawn.

Together these approaches allow for a comprehensive study of the effect of the mechanical microenvironment on the cellular mechanoresponse.

Chapter 3

Materials and Methods

3.1 Materials

3.1.1 Chemicals and Solutions

All chemicals were stored according to the manufacturer's recommendation and diluted if necessary. Solutions for tissue cultures were handled under sterile conditions and sterile filtered where necessary.

Table 3.1: Reagents for 3D laser microprinting.

Substance	Supplier Order Nr.	Application
3-(trimethoxysilyl)propyl-methacrylate	Sigma-Aldrich M6514-25ML	Silanization of substrates for 3D printing
Acetone	Carl Roth 5025.1	Development of printed scaffolds
IP-PDMS	Nanoscribe	Photoresist for fabrication of metamaterial scaffolds
IP-S	Nanoscribe	Photoresist for fabrication of migration channels
Irgacure819	Ciba AG 024475001PS04	Photoinitiator for 3D printing
Isopropanol	Carl Roth 6752.2	Development and washing of printed scaffolds
Pentaerythritol triacrylate (PETA)	Sigma-Aldrich 246794-500G	Monomer for 3D printing
Propylene glycol methyl ether acetate (PGMEA)	Carl Roth 7966.1	Development of migration channels
Toluene	Carl Roth 9558.3	Solvent for silanization agent

Substance	Supplier Order Nr.	Application
Trimethylolpropane ethoxylate triacrylate (TPETA)	Sigma-Aldrich 412171-250ML	Monomer for 3D printing

Table 3.2: Reagents for electrospinning.

Substance	Supplier Order Nr.	Application
N-(3-Dimethylaminopropyl)-*N*'-ethylcarbodiimide hydrochloride	Sigma-Aldrich 03450-25G	Crosslinking of gelatine nanofibres
N-Hydroxysuccinimide	Sigma-Aldrich 130672-25G	Crosslinking of gelatine nanofibres
Acetic acid	Nacalai tesque 00212-85	Preparation gelatine nanofibres
Acetone	Nacalai tesque 00310-53	Cleaning of cover slips
Ethanol	Nacalai tesque 14713-53	Cleaning of cover slips, solvent for crosslinking agents
Ethylacetate	Nacalai tesque 14747-65	Preparation gelatine nanofibres
Gelatine type A	Sigma-Aldrich G1890	Preparation gelatine nanofibres
Methanol	Nacalai tesque 21914-03	Cleaning of cover slips

Table 3.3: Tissue culture materials.

Solution	Supplier Order-Nr.	Application
Fetal bovine serum (FBS)	Hyclone SH30541.03	Additive for culture medium
DMEM (Dulbecco's Modified Eagle's Medium)	PAN Biotech P04-03590	Culture medium for tissue culture

Solution	Supplier Order-Nr.	Application
DMEM with HEPES, without phenol red	ThermoFisher Scientific 21063029	Culture medium for live cell imaging
Dimethyl sulfoxide (DMSO)	Sigma-Aldrich D2650	Cryopreservation of cells
Fibronectin	Sigma-Aldrich F1056-2MG	Coating of cell culture substrates
PBS (phosphate buffered saline)	PAN Biotech P04-36500	Washing solution for tissue cultures without Calcium and Magnesium
Penicillin/Streptomycin (Pen/Strep)	Gibco 15140-122	Additive for imaging medium
Trypsin/EDTA	Gibco 15400-054	Detaching of cells

Table 3.4: Other materials.

Substance	Supplier Order-Nr.	Application
Fluorescein-5(6)-isothiocyanat	Sigma-Aldrich 46950-50MG-F	Characterisation of gradient formation in chemotaxis chamber
Tris-HCl	Carl Roth 9090.3	Solvent for Fluorescein

3.1.2 Reagents for Immunocytochemistry, Dye-Conjugated Affinity Probes and Antibodies

All antibodies and affinity probes were reconstituted and stored according to the manufacturer's protocol.

Table 3.5: Reagents for immunocytochemistry.

Substance	Supplier Order Nr.	Application
Bovine serum albumin (BSA)	Sigma-Aldrich A4509-100G	1% in PBS, blocking agent for immunocytochemistry
Mowiol 4-88	Merck Millipore 475904	Preservation medium for immunostained samples
Para-formaldehyde (PFA)	Merck Millipore 30525-89-4	4% in PBS, fixing of cells
PBS	Pan Biotech P04-53100P	Washing solution
Triton X-100	Carl Roth 3051.1	0.1% in PBS, cell permeabilisation

Table 3.6: Affinity proteins.

Target	Probe Conjugate	Stock concentration Working dilution	Supplier Order-Nr.
F-actin	Phalloidin AlexaFluor 488	n.a. 1:200	Molecular Probes A12379
F-actin	Phalloidin AlexaFluor 568	n.a. 1:200	Molecular Probes A12380
F-actin	Phalloidin AlexaFluor 647	n.a. 1:100	Molecular Probes A22287
Nucleic acids	DAPI	5 mg/mL 1:500	Roth

Table 3.7: Primary antibodies and specification.

Antigen	Organism Isotype	Stock concentration Working dilution	Supplier Order-Nr.
GM130	mouse monoclonal	250 µg/mL 1:500	BD Biosciences 610822
NM IIA	rabbit polyclonal	1 mg/mL 1:500	Biolegend 909801
NM IIB	rabbit polyclonal	1 mg/mL 1:500	Biolegend 909901

Antigen	Organism Isotype	Stock concentration Working dilution	Supplier Order-Nr.
Paxillin	rabbit polyclonal	200 µg/mL 1:300	Santa Cruz sc-5574
Vinculin	mouse monoclonal	0.5 mg/mL 1:100	Invitrogen 14-9777-82
YAP	mouse monoclonal	100 µg/mL 1:300	Santa Cruz sc-101199

Table 3.8: Secondary antibodies and specification.

Antigen	Organism Conjugate	Stock concentration Working dilution	Supplier Order-Nr.
Mouse IgG	donkey AlexaFluor 488	n.a. 1:200	Jackson ImmunoResearch 715-545-151
Mouse IgG	goat AlexaFluor 488	2 mg/mL 1:200	Molecular Probes A11029
Mouse IgG	donkey Cy3	n.a. 1:200	Jackson ImmunoResearch 715-165-151
Mouse IgG	goat Cy3	n.a. 1:500	Jackson ImmunoResearch 115-165-146
Rabbit IgG	donkey AlexaFluor 568	2 mg/mL 1:200	Invitrogen A10042
Rabbit IgG	donkey Cy5	n.a. 1:200	Jackson ImmunoResearch 711-175-152

3.1.3 Technical Equipment and Microscopes

Table 3.9: Technical equipment and microscopes.

Device	Objective	Manufacturer	Application
AxioObserver Z1	CP-Achromat 10×/0.25 Ph1 Plan Apochromat 20x/0.8 Ph2 M27 Plan Apochromat 40×/1.4 oil DIC (UV) VIS-IR M27	Carl Zeiss	Imaging of living cells, with heated incuabtion chamber

Device	Objevtive	Manufacturer	Application
LSM 800 with Airyscan	Plan Apochromat 40×/1.4 oil DIC (UV) VIS-IR M27 Plan Apochromat 63×/1.4 oil DIC II	Carl Zeiss	Confocal laser scanning microscope with Airyscan-technology for superresolution
Nanoscribe Photonic Professional GT	Plan Apochromat 63×/1.4 oil	Nanoscribe	Printing of 3D scaffolds
NANON-01B	-	MECC Nanofiber	Electrospinning of gelatine nanofibres
Quantum X	LCI Plan-Neofluar 25×/0.8 Imm Korr Ph2 M27	Carl Zeiss	Printing of 3D scaffolds

3.2 Substrate Fabrication and Preparation

All substrates for cell culture application were sterilised by UV-light exposure immersed in 70% ethanol, unless indicated differently, for at least 30 min prior to cell seeding.

3.2.1 3D Scaffolds

All 3D scaffolds were fabricated by 3D laser microprinting in an ISO 7 clean room environment under yellow light to prevent preliminary polimerisation of the photoresists. Silanised substrates were used for all printing. For the sake of expediency, used custom resists are referred to by the name of the monomer.

3.2.1.1 Silanisation

To facilitate strong attachment of printed structures to the glass substrates, 22×22 mm high precision cover slips with a thickness of 170 µm ± 5 µm were functionalised with 3-(trimethoxysilyl)propylmethacrylate. For this, cover slips were cleaned with isopropanol and plasma-treated for 10 min. Treated cover slips were immediately transferred to a 1.7 mM solution of 3-(trimethoxysilyl)propylmethacrylate in toluene for 1 h at room temperature. Functionalised cover slips were rinsed with water, blow dried with pressurised nitrogen and stored until further use.

3.2.1.2 Metamaterials

Scaffolds with metamaterial characteristics were fabricated using a Photonic Professional GT equipped with a 63× oil immersion objective (NA = 1.4) in conventional mode. The scaffolds consisted of stiff supporting beams atop a passivating base plate and nets with metamaterial geometries. To achieve this, two sequential printing steps using two different resists were performed as schematically depicted in Figure 3.1.

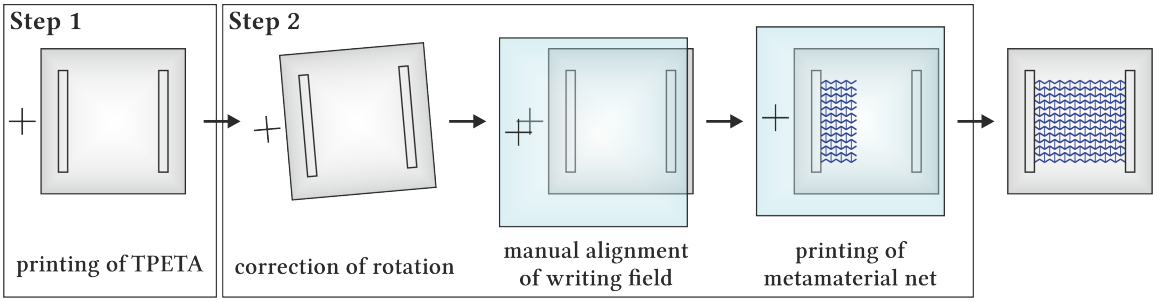

Figure 3.1: Schematic depiction of metamaterial printing process.
In the first step, stiff supporting beams are printed from trimethylolpropane ethoxylate triacrylate (TPETA) together with a passivating baseplate and an alignment marker. After development, the second printing step is performed. Before printing, rotations introduced by sample transfer are corrected. The correct positioning of the nets is ensured by manual alignment of the writing field (blue) with the printed structure based on the alignment markers and metamaterial nets are printed between the supporting beams.

First, stiff supporting beams together with a passivating base plate and alignment markers were printed from trimethylolpropane ethoxylate triacrylate (TPETA) with 2% (w/w) Irgacure819 as photoinitiator. Printing was performed at a scan speed of 5000-15000 µm/s and a powerscaling of 100%. Printed scaffolds were developed in a 1:1 mixture of acetone and isopropanol at least over night, rinsed with isopropanol and blow dried with pressurised nitrogen.
Prior to the second writing step, o-rings with an inner diameter of 8 mm and a height of 1 mm were glued around the printed structure. Nets with metamaterial geometries were printed between the stiff beams from IP-PDMS or pentaerythritol triacrylate (PETA) with 2% (w/w) Irgacure819 as photoinitiator. Printing was performed using a powerscaling of 65-70% and scan speeds of 1000 µm/s or 10000 µm/s, respectively. To ensure correct placement of the nets, x- and y-rotations were corrected *via* the built in tranformation tool and writing fields were aligned manually using the previously printed alignment marker. Samples printed using PETA were first developed in a 1:1 mixture of isopropanol and acetone for at least 30 min before being transferred to isopropanol. IP-PDMS scaffolds were directly developed in isopropanol. Scaffolds were kept in isopropanol for at least 2 d, exchanging the developer at least once. From this point on, especially the scaffolds made from IP-PDMS were always kept in solution to avoid collapse of the net. This was ensured by the o-ring acting as a reservoir, thus preventing drying of the scaffold during later handling steps.
One day prior to use in cell culture, scaffolds were transferred to water. Remaining organic solvent was removed by washing three times for 10 min with ddH_2O before UV sterilisation.

3.2.1.3 Migration Channels

Migration channels were printed from IP-S using a Quantum X equiped with a 25× immersion correction objective (NA = 0.8). Printed samples were developed by washing two times with PGMEA for 10 min and two times with isopropanol for 5 min. Developed samples were rinsed with isopropanol and blow dried using pressurised nitrogen.

3.2.2 Gelatine Nanofibres

Aligned gelatine nanofibres (aGNF) and random gelatine nanofibres (rGNF) were fabricated at the Center for Integrative Medicine and Physics (Institute for Advanced Study, Kyoto University, Kyoto) during a research stay at the group of Prof. Dr. Motomu Tanaka. A NANON-01B electrospinner was used for preparation of gelatine nanofibres. To ensure reliable fibre distribution and density, humidity and temperature during electrospinning did not exceed 25% and 23 °C, respectively. Before use in cell culture, nanofibres were washed at least three times for 10 min with 70% ethanol and PBS each.

3.2.2.1 Cleaning of Substrates

Round cover slips with Ø25 mm were cleaned by washing with acetone, followed by ethanol, methanol and ddH_2O in an ultrasonic bath for 3 min each. Washed samples were dried under vacuum and stored until further use.

3.2.2.2 Gelatine Solution

The gelatine solution for electrospinning consisted of 10% (w/w) gelatine, 42% (w/w) acetic acid, 28% (w/w) ethylacetate and 20% (w/w) ddH_2O. The components were dissolved under constant stirring over night at room temperature. Solution was always prepared fresh.

3.2.2.3 Preparation of Aligned Nanofibres

For preparation of aGNF, the electrospinner was equipped with a drum collector onto which the substrates were fixed with adhesive tape. The gelatine solution was loaded into a syringe with a 22 gauge blunt end needle which was positioned 10 cm above the drum collector. The drum collector was accelerated to a speed of 2300 rpm and a voltage of 15 kV was applied to the needle. aGNF were obtained by dispersing the solution at a flow rate of 0.2-0.3 mL/h for 15 min.

3.2.2.4 Preparation of Random Nanofibres

For preparation of rGNF, substrates were fixed to a flat surface with adhesive tape and gelatine solution loaded into a syringe with a 22 gauge blunt end needle, positioned 14 cm above the substrates. A voltage of 16 kV was applied to the needle. rGNF were obtained by moving the needle horizontally across the substrates at a speed of 20 mm/s and dispersing the gelatine solution at a flow rate of 0.5 mL/h for 1 min.

3.2.2.5 Crosslinking of Fibres

Electrospun fibres were crosslinked in 0.2 M *N*-(3-Dimethylaminopropyl)-*N*'-ethylcarbodiimide hydrochloride and 0.2 M *N*-Hydroxysuccinimide in 99.9% ethanol for 4 h at room temperature. Samples were washed three times for 5 min with 99.9% ethanol and left to dry.

3.2.3 3D Collagen Fibres

Aligned and orthogonal 3D collagen fibres were purchased from 3D BioFibR Inc. Following the suppliers instructions, dried fibres were prehydrated in an incubator over night before hydration with PBS for 30 min at room temperature. Hydrated fibres were checked for defects prior to use in cell culture.

3.2.4 Chemotaxis Chambers

Chemotaxis chambers were fabricated by Alexandra Moritz and Marc Schneider (Korvink group, Institute of Microstructure Technology, KIT, Karlsruhe) *via* hot embossing of cyclic olefin copolymer. Chambers were washed with 70% ethanol for 2 d to remove any soluable residues of the polymer before use in cell culture.

3.3 Cell Culture

In this work, immortalised cell lines originating from rat embryonic fibroblasts (REF52) or bone osteosarcoma cells (U2OS) were used (see Table 3.10). Both cell types exhibit an adherent phenotype with either fibroblast-like or epithelial morphology, respectively. Different NM II KO cell lines were previously generated from U2OS wt cells (Weißenbruch et al., 2021). Due to their prominent actomyosin network and polarised phenotype, U2OS cells were chosen for studies focusing on the organisation of the actin cytoskeleton and cellular polarisation (Beach et al., 2014; Hotulainen & Lappalainen, 2006).

Table 3.10: Used cell lines.

Cell line	Organism	Origin	Supplier
REF52 wt	rat	fibroblast cells from embryonic tissue	Olivier Pertz, Basel
U2OS wt	human	osteosarcoma cells from tibia	ATCC, #HTB-96
U2OS NM IIA KO	human	U2OS cells lacking NM IIA expression	Kai Weißenbruch
U2OS NM IIB KO	human	U2OS cells lacking NM IIB expression	Kathrin Stricker

All work with tissue culture was performed under sterile conditions.

3.3.1 Cultivation

Cell cultures were kept in a sterile bactericidal incubator at 37 °C, 98% humidity and 5% CO_2. All cell lines were cultivated in DMEM containing 10% FBS, referred to as feeding medium, and passaged every second to third day once a confluency of 90% was reached to allow for constant growth.

For passaging, cells were rinsed with 5 mL PBS without Ca^{2+} and Mg^{2+} and detached with 150 µL trypsin/EDTA during 2-3 min incubation at 37 °C. The reaction was inhibited by addition of fresh feeding medium and remaining trypsin/EDTA as well as dead cells removed by centrifugation

for 5 min at 1000×g. The obtained cell pellet was resuspended in fresh feeding medium and an appropriate fraction transferred to a new flask. Passaging ratios for REF52 cells usually ranged from 1:5 to 1:10; U2OS cell lines were passaged at ratios of 1:3 to 1:6.

3.3.2 Cell Revival and Cryopreservation

Cryopreserved cells were thawed as quickly as possible at 37 °C using a waterbath and immediately transferred into a tube containing 4 mL prewarmed feeding medium. Remaining DMSO, a preservation agent, was removed by centrifugation for 5 min at 1000×g. The obtained cell pellet was resuspended in fresh prewarmed feeding medium and the suspension transferred into a T-25 flask. The following day, medium was exchanged and the cultures were passaged once 90% confluency was reached.
For cryopreservation, cell cultures were expanded to T-75 culture flasks and cells were collected once confluency was reached as described above. The obtained cell pellet was resuspended in 2 mL feeding medium containing 10% DMSO as a preservation agent and 1 mL transferred to each cryovial. The cryovials were frozen at -80 °C using an isopropanol chamber for controlled freezing and transferred to a liquid nitrogen tank for long term storage.

3.3.3 Cell Seeding

Where necessary, substrates for cell culture were coated with 10-20 µg/mL fibronectin in PBS for 1 h at room temperature. Coated substrates were rinsed with feeding medium prior to seeding of cells.
Cell suspensions were obtained as decribed above and their respective concentrations determined using a Neubauer counting chamber. The amount of cells seeded on the individual substrates are given in Table 3.11.

Table 3.11: Substrates, coatings and cell seeding amounts.

Substrate	Dimension	Fibronectin coating	Seeding amount
3D collagen fibres	Ø10 mm	-	30000 cells (orthogonal)
	15×15 mm	-	35000 cells (parallel)
Metamaterials	8 mm ($Ø_{inner}$ O-ring)	20 µg/mL	5000 cells
	22×22 mm (cover slip)		
Glass cover slip	Ø18 mm	10 µg/mL	40000 cells
Gelatine nanofibres	Ø25 mm	-	80000 cells
Migration channels	22×22 mm	10 µg/mL	40000 cells

3.4 Live Cell Imaging

For live cell imaging, cells were seeded and left to adhere for at least 3 h or over night to ensure full spreading. Live cell imaging was performed using an AxioObserver Z1 microscope with a heated

incubation chamber. Heating was turned on at least 1 h before imaging.
To minimise phototoxicity during imaging, the feeding medium containing phenol red as pH-indicator was exchanged against imaging medium, consisting of DMEM without phenol red and 10% FBS. To maintain a constant pH-value, the imaging medium contained 25 mM HEPES as a CO_2-independent buffer substance.

3.4.1 Metamaterials

For analysis of cellular forces on 3D structures with metamaterial properties, cell cultures were imaged using differential interference contrast (DIC) microscopy. This method was chosen over phase contrast microscopy to ensure clear visualisation of the metamaterial net which proved crucial for later analysis. Images were acquired every 30 s for 1 h using a 40× oil immersion objective (NA = 1.4).

3.4.2 Cell Migration in Migration Channels

Prior to imaging, the inner reservoir of the migration chamber was filled with 100 µL imaging medium. Square 22×22 mm cover slips with seeded cells were taken out of the culture medium and the cell-free side dried on a paper towel. On the cell-side, roughly 2 mm from each edge were dried with a paper towel to ensure tight sealing of the chamber. The hence prepared cover slip was carefully lowered on the chamber, avoiding formation of air bubbles in the inner reservoir, as well as spillage of the medium outside of the reservoirs. The cover slip was secured in place with adhesive tape and roughly 120 µL of imaging medium was added to the outer reservoir *via* the drilled openings, again avoiding the formation of air bubbles. Once the chamber was sufficiently filled, the openings were sealed with adhesive tape and the chamber used for imaging.
Phase contrast microscopy was used to observe migrating cells. Images were acquired in 15 min intervals for 20 h using a 10× objective (NA = 0.25).

3.5 Immunocytochemistry

Immunocytochemical staining was used to visualise intracellular structures. Cells were left to adhere for at least 3 h to over night after seeding to ensure complete spreading. All steps were performed in a darkened humidity chamber to avoid drying of the samples or bleaching of the flourophors. To reduce unspecific binding of staining agents, all antibodies and affinity probes were diluted to the appropriate working concentration in 1% BSA in PBS.
Cells were fixed by incubation with 4% PFA for 10 min and permeabilised by washing three times for 5 min with PBS containing 0.1% Triton-X100 (PBS-T). Subsequently, the samples were incubated with primary antibodies for 1 h at room temperature or 4 °C over night. Following the first staining step, samples were again washed three times for 5 min with PBS-T and incubated with secondary antibodies as well as affinity probes for 1 h at room temperature or 4 °C over night. Unbound staining agents were removed by washing three times for 5 min with PBS. To avoid the

formation of salt crytals, remaining PBS was rinsed off with ddH_2O and samples were embedded in 20% (w/v) Mowiol in PBS:glycerine (2:1). The Mowiol was left to harden at room temperature over night and the samples stored at 4 °C until imaging.

3.6 Evaluation and Quantitative Analysis

All data was analysed using Fiji (Schindelin et al., 2012), OriginPro® 2023 and Microsoft Excel 2019. Unless indicated differently, significance niveaus were determined using a two-sample t-test. Differences in variation were determined using a two-sample test for variance. The significance level was defined as $\alpha = 0.05$. All box plots represent the 25-75% range indicated by the box, as well as the median and mean values, indicated by a solid line and square, respectively. Whiskers correspond to the 5-95 percentile range.
Maximum intensity projections of z-stacks, acquired every 0.5 µm, were used for analysis of immunocytochemical stainings.

3.6.1 Metamaterials

To analyse the behaviour of cells cultured on substrates with metamaterial characteristics, cellular forces, morphology and mechanical activation was evaluated. As the force field analysis forms one of the key developments of this work, it is described in detail in Section 4.1.
Only cells with minimal contact to the stiff beams, the passivating base plate or other cells were chosen for analysis to limit the influence of other factors than the metamaterial characteristics.

3.6.1.1 Analysis of Cell Shape

Two descriptors of cellular morphology were chosen for analysis: cell spreading area and aspect ratio. Immunocytochemical staining of the actin cytoskeleton was used to determine the cell area. For this, a threshold was applied to obtain a mask following the outline of the cell as visualised in the top panel of Figure 3.2. From this mask, cell area and aspect ratio were calculated.

3.6.1.2 YAP Distribution

The nuclear to cytoplasmic ratio of the transcriptional co-activator YAP was determined following the procedure published by Kuroda and colleagues (Kuroda et al., 2017). Here, the nuclear area is determined by creating a mask based on the DAPI staining and the mean intensity measured within, whereas the mean cytoplasmic intensity is derived from seven circular areas with a diameter of 10 µm in close proximity to the nucleus. The procedure is depicted in the bottom panel of Figure 3.2.

3.6.2 Polarisation on Structured Substrates

The effect on cells cultured on structured substrates like aligned nanofibres or 3D orthogonal collagen fibres was analysed based on cell morphology, as well as Golgi apparatus positioning and distribution.

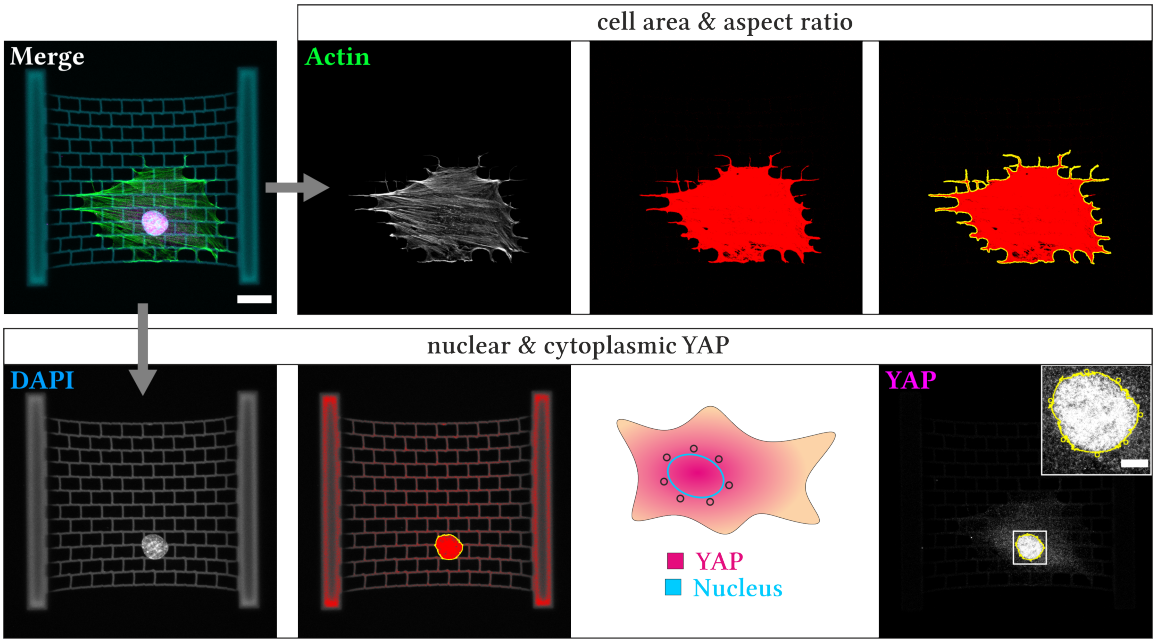

Figure 3.2: Analysis of cell area, aspect ratio and YAP distribution.
Top panel: Cell spreading area and aspect ratio were calculated from a mask (yellow), derived from the thresholded (red) immunocytochemical staining of the actin cytoskeleton.
Bottom panel: Mean nuclear and cytoplasmic YAP intensities were measured within masks (yellow) encircling the nucleus derived from the thresholded (red) DAPI staining and seven circular areas in close proximity to the nucleus, respectively. For better visibility, the measured areas within the indicated region are enlarged in the last image. Scale bar: 20 µm, magnification: 5 µm.

To limit other influencing factors, only cells with no contact to other cells were chosen for analysis. For aligned gelatine nanofibres, preferably regions with denser fibres were chosen.

3.6.2.1 Ordering of Actin Fibres

The relative orientation of actin fibres with respect to gelatine nanofibre orientation was analysed in collaboration with Danny Egic (Tanaka group, Institute of Physical Chemistry, Heidelberg University, Heidelberg). For this, a self-written image processing macro by Dr. Philipp Linke, employed in previous publications, was used (Inoue et al., 2015; Yoshikawa et al., 2013). In brief, actin fibres were identified, segmented and their orientation relative to the vertical axis of the image determined. To match this with the orientation of aligned gelatine nanofibres, images were rotated prior to analysis such that the main fibre direction corresponds to the vertical image axis. In case of random fibres, no additional image preparation was necessary.

3.6.2.2 Analysis of Cell Shape

As decribed in Section 3.6.1, cell spreading area and aspect ratios were measured by creating a mask from the immunocytochemical actin staning as depicted in the top panel of Figure 3.3.

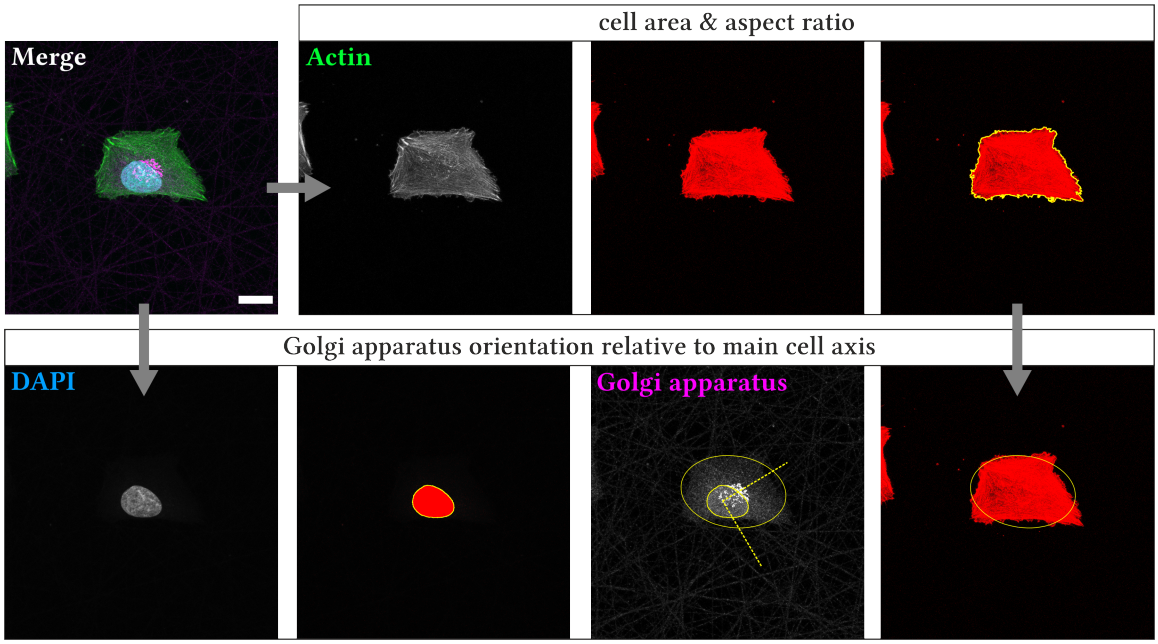

Figure 3.3: Analysis of cell area, aspect ratio and golgi apparatus orientation.
Top panel: Cell spreading area and aspect ratio were calculated from a mask, derived from the immunocytochemical staining of the actin cytoskeleton.
Bottom panel: For determination of the orientation of the golgi apparatus, an ellipse was fitted to the mask encircling the cell shape to identify the main cell axis. For the localisation of the nucleus, a mask was created from the DAPI staining. Golgi apparatus orientation was then determined with respect to the main cell axis and nucleus position. If the focus of the golgi apparatus was located parallel to the main cell axis and within a $+/-45°$ angle originating from the centre of the nucleus as indicated, it was assumed to be aligned. Scale bar: 20 µm.

3.6.2.3 Alignment of Golgi Apparatus with Main Cell Axis

In analogy to the approach published by Chen and colleagues (Chen et al., 2013), the alignment of the Golgi apparatus with the main cell axis was determined. Based on the mask encircling the cell area, an ellipse was fitted to the cell shape to determine the main cell axis for analysis of the Golgi apparatus orientation (see bottom panel Figure 3.3). Additionally, the nuclear area was determined based on the DAPI staining. Using these two masks, the orientation of the Golgi apparatus was determined with respect to the main cell axis and cell nucleus and categorised as described in Table 3.12.

Table 3.12: Categories for Golgi apparatus orientation.

Category	Criteria
aligned	centre of Golgi apparatus located parallel to main cell axis and within an angle of +/- 45°, originating from the centre of the nucleus. Schematically depicted in bottom panel of Figure 3.3
not aligned	centre of Golgi apparatus located perpendicular to main cell axis and outside of the +/- 45° area, originating from the centre of the nucleus
not defined	centre of Golgi apparatus located within nuclear area

3.6.2.4 Golgi Apparatus Distribution

In addition to the Golgi apparatus localisation, its distribution was analysed in collaboration with Danny Egic (Tanaka group, Institute of Physical Chemistry, Heidelberg University, Heidelberg). As before, cell shape, nucleus localisation and Golgi apparatus distribution was determined by thresholding the image and creating a mask. Images were rotated so the main cell axis was parallel to the x-axis. Originating from the centre of mass of the nucleus, the image was segmented in 10° segments in a radius of 600 px, corresponding to 46.3 µm. The area occupied by the Golgi apparatus staining in each segment was measured and plotted in a polar diagram.

Chapter 4

Results

In this chapter, the results of the individual projects are described, beginning with the development of a metamaterial-based approach to study the cellular mechanoresponse in Section 4.1. Following this, Section 4.2 focusses on the influence of structured environments on the morphological adaptation and polarisation of cells. The chapter concludes with the introduction of a setup to investigate the effect of confinement, an additional mechanical restriction of 3D environments, in Section 4.3.

4.1 Development of a Metamaterial-Based Approach to Study the Cellular Mechanoresponse

One modulating factor of cellular contractility is the stiffness of the cellular environment. Like most material properties, this factor is largely influenced by the chemical structure of the substrate. Thus, to generate cell culture substrates with a variety of physical properties, screening for different chemical components was necessary. However, once an appropriate microstructure is introduced, these properties can be altered despite using the same chemical compound. Additionally, previously inaccessible or rare parameters like the Poisson's ratio can be targeted. Such materials can be referred to as metamaterials which exhibit different effective parameters than the bulk material due to the added dimension of metamaterial properties. Thus, by eliminating the need for compound screening and enabeling the manipulation of previously inaccessible material properties, mechanical metamaterials form an interesting class of materials for the study of the cellular mechanoresponse. In the course of this work, a 3D microscaffold-based approach was developed to test the effect of different metamaterials on the cellular mechanoresponse, which was published as a proof-of-principle in 2023 (Munding et al., 2023).

4.1.1 Scaffold Design and Characterisation

Based on the work of Zhang and colleagues in 2013, Dr. Marc Hippler (previously Zoological Institute and Institute of Applied Physics, KIT, Karlsruhe) designed and developed a fabrication process for 3D scaffolds with metamaterial properties. While Zhang and colleagues fabricated scaffolds solely from a polyethylene glycol diacrylate (PEGDA) based resist (W. Zhang et al., 2013), his process includes the use of two different resists with different mechanical properties. Figure 4.1A

schematically depicts the design of the scaffold: a net with metamaterial geometry made from IP-PDMS is suspended between two stiff beams located atop a baseplate. IP-PDMS, a highly elastic PDMS-based photoresist, only became commercially available in the last years. When in aqueous environment, it exhibits a low Young's modulus of 700 kPa, which renders it more than three orders of magnitude softer than other commonly used resists like IP-S or PETA (Munding et al., 2023). Thus, together with its good optical properties and low cytotoxicity, this resist is a promising material for mechanobiological studies. Beams as well as the baseplate below are fabricated from protein-repellent TPETA, which helps to restrict seeded cells mainly to the metamaterial net. With a Young's modulus of 12.7×10^3 kPa in aqueous environment, it is considered a stiff and non-deformable material, suitable as a support structure (Hippler et al., 2020). The metamaterial net is freely hanging between the beams, as visible in the 3D reconstruction in Figure 4.1B. For the initial tests, three different metamaterial geometries were chosen as depicted in Figure 4.1D-F, termed bowtie, brickstone and honeycomb, respectively.

In order for the biological cell to experience the effective metamaterial properties rather than the local microstructure, unit cell sizes were set to be 3-5 times smaller than the biological cell. As the cellular contractility is influenced by the available adhesion area, filling fractions of the individual geometries were kept as close as possible.

The different geometries aim at achieving different behaviour under x-axial compression or stretch, as visualised in Figure 4.1C. When bowtie geometries are pulled along the x-axis, they expand perpendicular to the axis of stretch; an effect associated with negative Poisson's ratio also known as auxeticity. Honeycomb geometries, on the other hand, contract perpendicular to the axis of expansion, thus exhibiting positive Poisson's ratio behaviour common in many materials. For brickstone geometries, neither expansion nor contraction is observed, thus exhibiting a Poisson's ratio of zero. However, as cells do not only concentrate their contractility on a singular axis, the individual Poisson's ratios and Young's moduli were calculated in dependency of the angle of applied force by Dr. Yi Chen (Wegener group, Institute of Applied Physics, KIT, Karlsruhe). The results are visualised in Figure 4.1G-I. While the Poisson's ratios for bowtie geometries are as expected for an angle of 0 ° and 180 °, equaling compression or stretch along the x-axis, they differ for other angles, some even reaching into positive values for the Poisson's ratio. For brickstone geometries, a value of 0 is only achieved for applying force along the y-axis and remains in the positive regime for all other angles. Solely honeycomb geometries show a mainly constant Poisson's ratio of 0.8-1 for all angles. For the Young's modulus, an angle-dependency can be observed for all three geometries. With a maximum value below 25 kPa, bowtie structures exhibit the smallest Young's moduli of the three geometries, with the highest values along the x- and y-axis. On the other hand, brickstone geometries exhibit the largest Young's modulus of up to 160 kPa along the x-axis. Unlike before, also honeycomb geometries exhibit an uneven distribution with the largest Young's moduli for diagonal stretch or compression, indicated by the highest values lying just below 50 kPa for 45 °, 135 °, 225 ° and 315 °.

This uneven distribution of Young's moduli and Poisson's ratios renders all three geometries anisotropic. Thus, the angle-dependency should be considered when analysing potential effects observed over the whole biological cell.

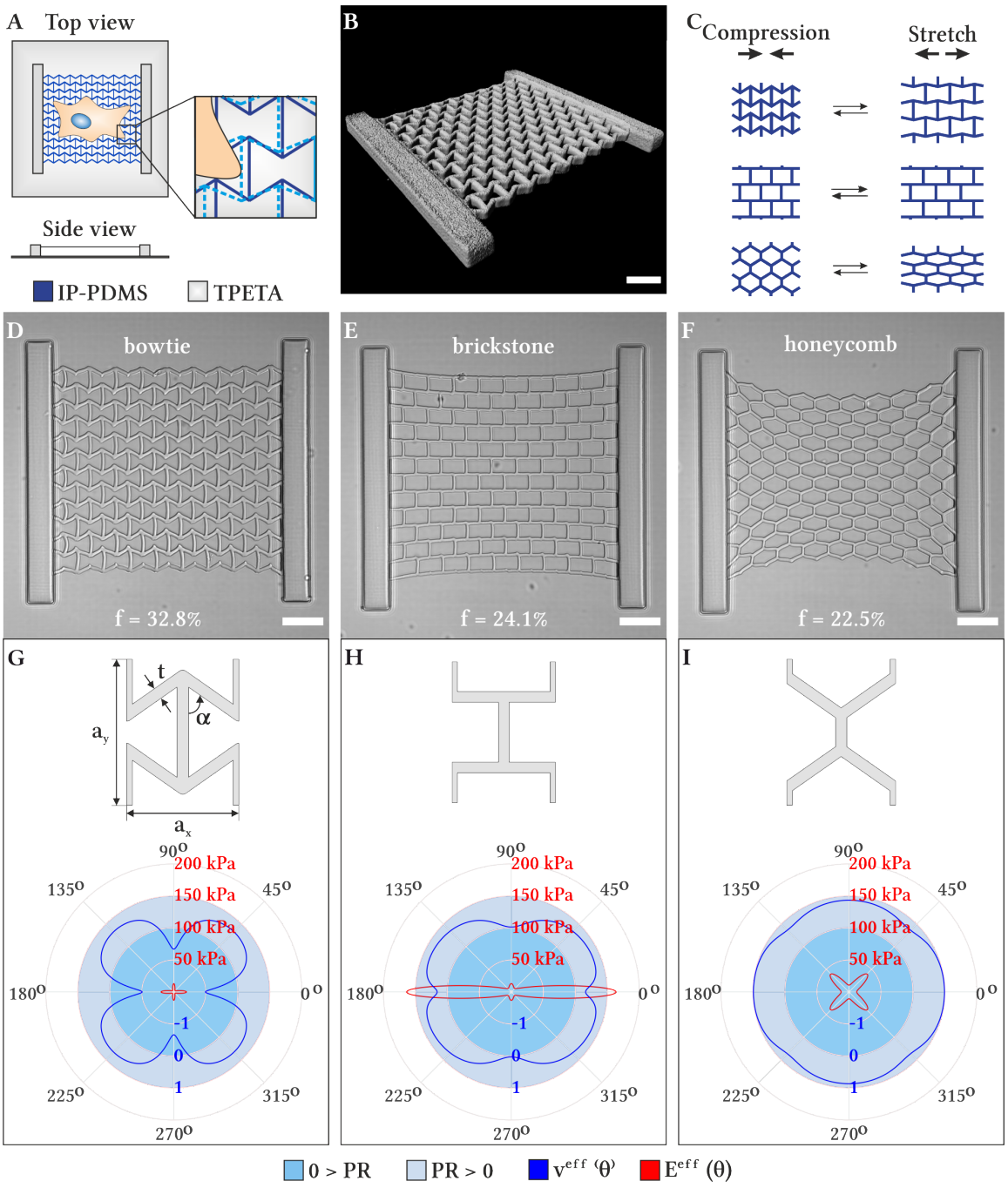

Figure 4.1: Design and physical characterisation of 3D scaffolds with metamaterial properties. (adapted from Munding et al., 2023)
A Schematical depiction of the scaffold design. Structures comprise two stiff supporting beams and a baseplate, fabricated from the passivating resist TPETA. Free hanging nets with metamaterial geometry are printed between the stiff supports. Unit cell sizes smaller than the biological cell were chosen together with the soft photoresist IP-PDMS, to allow for experiencing of effective metamaterial properties by a biological cell. **B** 3D reconstruction of a metamaterial scaffold based on its autofluorescence. The net is suspended between the supporting beams and free hanging. **C** Schematical depiction of the behaviour of metamaterial geometries under uniaxial stretch or compression along the x-axis. While bowtie geometries expand perpendicular to the axis of stretch, honeycomb geometries contract. Brickstone geometries remain unaffected in the axis perpendicular to the stretch. **D-F** ESID images of three different metamaterial scaffolds. Filling fractions of the three designs are *Continues on next page.*

Figure 4.1: *Continued from previous page.* roughly the same to minimise the effect of available cell adhesion area. **G-I** Calculated Young's moduli (red) and Poisson's ratios (blue) in dependency of the angle in which the force is applied. All geometries exhibit an anisotropic distribution of the two parameters. Merely honeycomb geometries show a nearly isotropic distribution of the Poisson's ratio. Poisson-negative and -positive regions are coloured in light blue and medium blue, respectively. Scale bars: 20 µm.

4.1.2 Workflow for Force Field Analysis

Starting from the scaffold design and 3D laser microprinting process developed by Dr. Marc Hippler, a workflow for cell experiments was established with the aim of analysing the cellular forces exerted on the metamaterial net. Cells seeded on the scaffolds adhered to the metamaterial nets as visible in the 3D reconstruction in Figure 4.2A. In order to experience the mechanical properties of the metamaterials, the cells do not merely need to adhere to the metamaterial nets, but they need to be able to deform them as well. As depicted in the enlarged time series images in Figure 4.2B^{I}-B^{III}, a rat embryonic fibroblast (REF) cell was able to deform the underlying metamaterial net over time. With this basic requirement fulfilled, an experimental and computational workflow was developed, schematically depicted in Figure 4.2C, which will be described in detail in the following.

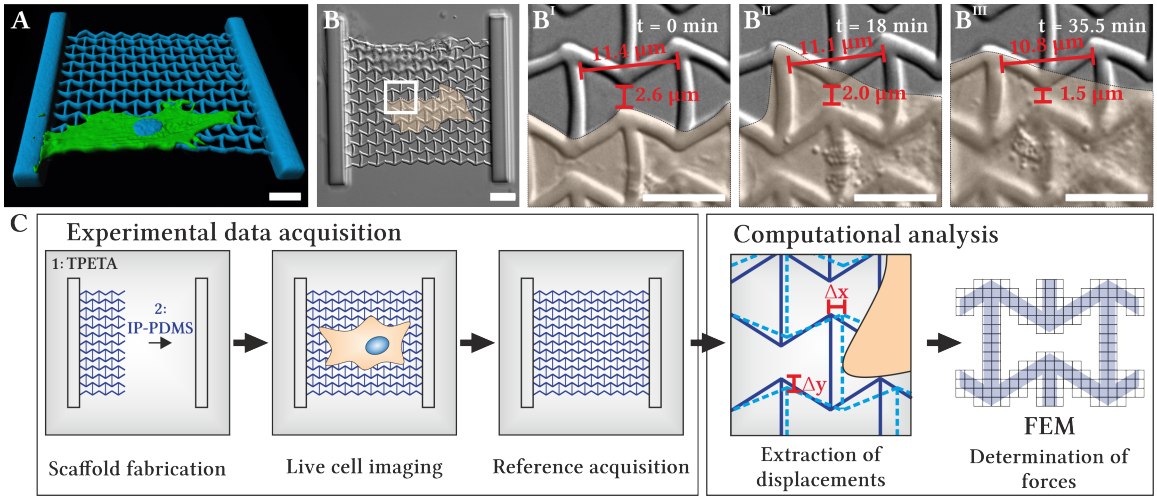

Figure 4.2: Workflow for analysis of forces on metamaterial scaffolds.
A 3D reconstruction of a REF cell on a metamaterial scaffold. Cell body (green) and nucleus (blue) were reconstructed from actin and DAPI stainings, respectively. The scaffold (blue) was reconstructed from its autofluorescence. **B** DIC image of a REF cell on a metamaterial net acquired during live cell imaging (LCI). The outline of the cell was traced manually and the cell area pseudocoloured for better visibility. **B^{I}-B^{III}** Magnifications of the area marked in B at different time points during live cell imaging (LCI). Over time, the cell deforms the underlying metamaterial net. Scale bars: 10 µm. **C** Schematic depiction of the experimental and computational workflow for the determination of exerted cellular forces (adapted from Munding et al., 2023). After scaffold fabrication, cells are seeded onto the metamaterial nets and their interaction with the metamaterial observed during LCI. After imaging, the cell is removed by trypsination to obtain a reference image of the non-deformed metamaterial. Displacement vectors are extracted from the timeseries images *via* digital image cross-correlation. The extracted vectors are used to determine the forces necessary for deformation *via* finite element method (FEM) with respect to the reference image. **A-B** Scale bars: 20 µm.

4.1.2.1 Experimental Data Acquisition

Scaffolds with metamaterial properties were fabricated by 3D laser microprinting in two sequential writing steps as described in Section 3.2.1.2. Cells were seeded on the metamaterial scaffolds and the cell-induced deformations imaged using DIC microscopy. This method proved superior to the commonly used phase contrast microscopy, as it eliminated halos appearing around the metamaterial net. This proved crucial for later analysis steps, as it allows clear visualisation of the metamaterial net at any given timepoint. Following LCI, cells were detached from the scaffolds by trypsination to obtain a reference image of the non-deformed nets. Acquiring the reference image after LCI greatly reduces the need for manual image alignments for later analysis compared to acquiring the reference image before seeding of cells. However, both methods proved feasible.

4.1.2.2 Computational Analysis

Following the experimental data acquisition, forces were calculated from observed deformations. For this, the resulting displacement vectors were extracted and subjected to finite element method (FEM) to determine the exerted force field.

Extraction of Displacement Vectors

The displacement vectors were extracted from the timeseries images using digital image cross-correlation as schematically depicted in Figure 4.3A. Timeseries images were corrected for drifts using the Fiji plugin "Linear stack alignment with SIFT" (Lowe, 2004) prior to further analysis. In collaboration with Dr. Tobias Frenzel (formerly Wegener group, Institute of Applied Physics, KIT, Karlsruhe), a previously published Matlab-script for image cross-correlation was refined to match the metamaterial setting (Frenzel et al., 2021). In the first frame of the timeseries, prominent regions were selected for tracking. For the metamaterial geometries, crossing points of the individual bars forming the net were chosen preferrably (see Figure 4.3C). These markers were tracked throughout the timeseries images and individual coordinates of each marker at each timepoint collected. From these coordinates, the displacement vectors for each timepoint were calculated with respect to the first frame. The obtained vector fields for one timeseries is depicted for different timepoints in Figure 4.3B. It is apparent that some regions experienced less deformation than others, corresponding to the localisation of the cell in the bottom left quarter (not indicated). Figure 4.3D shows the individual displacements in x- and y-direction for each timepoint. The lack of abrupt changes in displacement or flat lines, indicating false correlation or lost positions, indicate a correct tracking of the markers throughout all frames.

Determination of Force Fields *via* Finite Element Method

From the obtained displacements, force fields were extracted using FEM. The procedure was developed using the the commercial finite element software COMSOL Multiphysics in collaboration with Dr. Yi Chen (Wegener group, Institute of Applied Science, KIT, Karlsruhe). Essentially, it is based on mapping the individual displacements onto the autofluorescence-based non-deformed

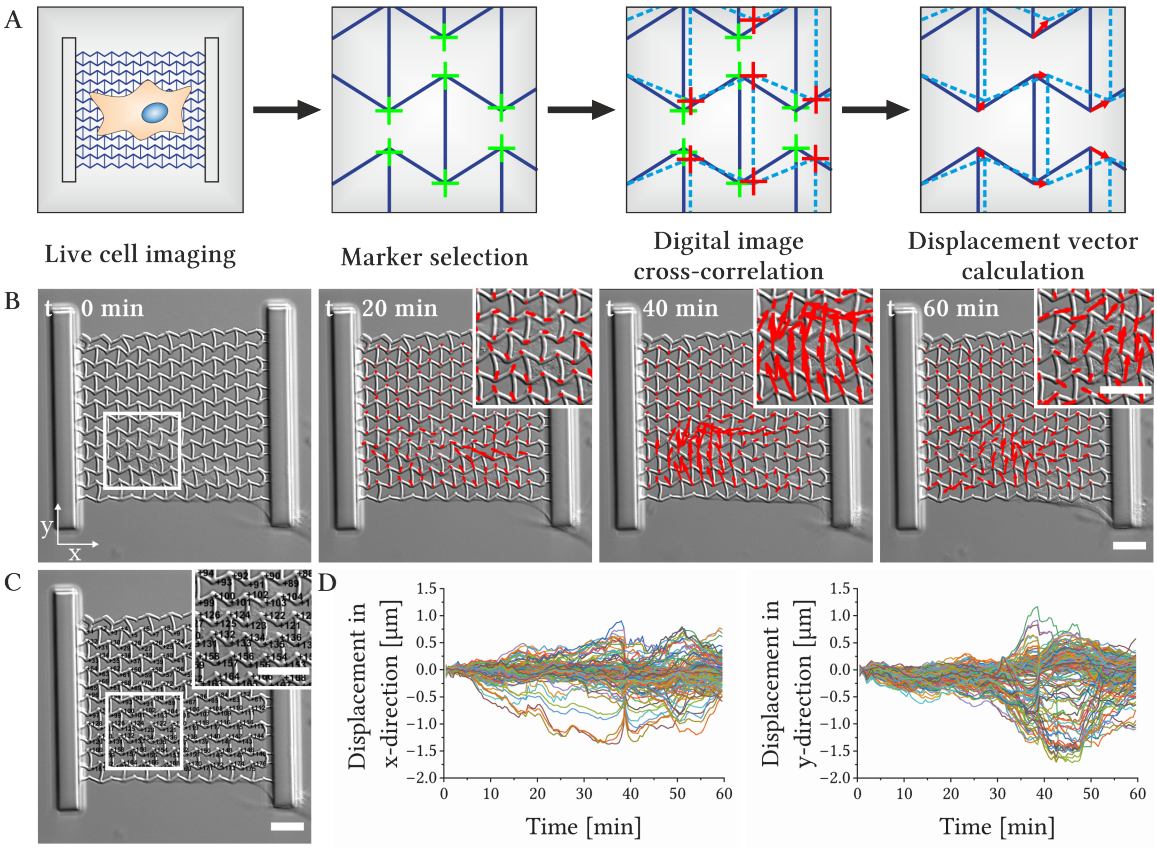

Figure 4.3: Extraction of displacements from LCI images.
A Schematic depiction of displacement vector extraction. Starting with the first frame of the LCI, markers are manually selected on prominent regions of the metamaterial net. These regions are tracked throughout the timeseries by digital image cross-correlation and the coordinates for each marker at each timepoint are collected. From these coordinates, the displacement vectors for each timepoint are calculated with respect to the first frame. **B** Timeseries images with the corresponding displacement vectors (red). As the obtained displacements are quite small, the vectors were scaled by a factor of 10 for better visibility. Top right images are magnifications of the region indicated at t=0 min. **C** Annotated markers used for displacement vector extraction. A total of 176 markers was selected to track the deformation of the whole metamaterial net. The image on the top right shows a magnification of the indicated region. **D** Extracted displacements in x- and y-direction over time with respect to the initial marker position. As visible in B, some markers show stronger displacement than others. **B-C** Scale bars: 20 µm.

reference image from which the necessary forces for this deformation are calculated. For the analysis, a binarised reference image was used, which was reduced in pixel size by a factor of two to reduce computational cost. To ensure correct mapping of the displacements, the reference image was corrected for rotation by determining the rotation angle *via* fitting a line to the stiff support beam of the scaffold. The boundaries of the metamaterial net were determined from the now accordingly rotated image. These boundaries were assumed to be fixed in the numerical simulations. After the boundaries were set, three markers were placed on the first image of the timeseries as well as the reference image. The positions of the markers were adjusted to match the position on the timeseries and the reference image. By comparison of the obtained coordinates, differences in scaling as well as rotation were determined and corrected. The individual steps of image preparation are schematically depicted in Figure 4.4A.

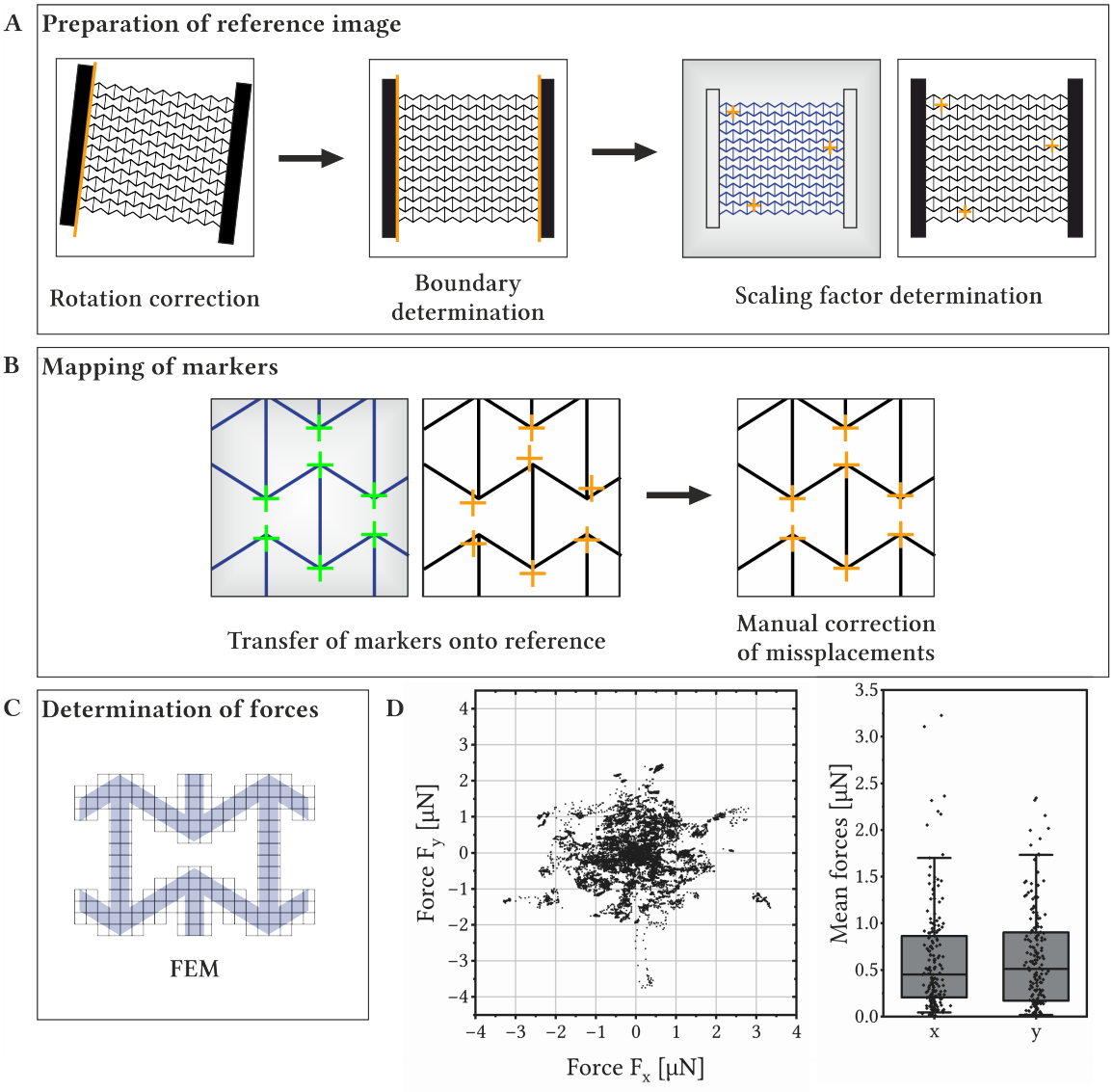

Figure 4.4: Determination of forces from displacement vectors.
A Prior to analysis of forces, the reference image needs to be adjusted to match the timeseries image. For this, rotations are corrected and the boundaries of the metamaterial net determined. Additionally, a potential difference in scaling is removed, in case reference images are acquired before LCI using a different imaging set up. **B** Once the images are prepared for analysis, the markers used for displacement tracking are transferred onto the reference image. As the first image of the timeseries already includes deformations, the markers are manually moved to the corresponding area on the non-deformed reference image. **C** The exerted cellular forces are derived from the displacement vectors by FEM. **D** Obtained forces in x- and y-direction for a REF cell cultured on a metamaterial net with bowtie geometry. The scatter plot shows forces exerted by the cell for every marker and each timepoint during imaging. Mean forces for each marker are depicted in the box plot, revealing no significant difference in x- and y-direction.

In the next step, the initial markers were mapped on the hence prepared reference image as schematically depicted in Figure 4.4B. As the first frame of the timeseries is acquired after the cells were allowed to fully spread on the metamaterial net, it already contains displacements in comparison to the reference. To account for this initial missplacement of the markers, they were manually moved onto the corresponding region of the reference image, thus providing an artifi-

cial t=0 image to which the subsequent displacement vectors were compared. For the numerical model, each pixel was considered as a square mesh with four finite element nodes resulting in roughly 10^5 square meshes for capturing the induced deformations. The Equation 4.1 for static linear elasticity was solved by using the plain strain Solid Mechanics module in Comsol Multiphysics.

$$\frac{E_{bulk}}{2(1+\nu_{bulk})(1-2\nu_{bulk}}\nabla(\nabla * u(r)) + \frac{E_{bulk}}{2(1+\nu_{bulk})}\nabla^2 u(r) = 0 \tag{4.1}$$

with E_{bulk} = bulk Young's modulus , ν_{bulk} = bulk Poisson's ratio and $u(r)$ = displacement vector

The E_{bulk} was assumed to be 700 kPa, derived from preliminary measurements, and the ν_{bulk} was set to 0.49. Each marker corresponded to a pixel in the numerical model. The displacement vectors obtained from the digital image cross-correlation for each maker were then applied to the four nodes of the corresponding pixel by using displacement boundary conditions. The force required at each marker (or pixel) was deduced as the sum of the forces at the corresponding four nodes. Obtained forces were scaled according to the thickness of the metamaterial nets which was determined from representative image stacks.

4.1.3 Force Field Analysis of Living Cells

REF cells were used for LCI, as they were able to deflect the metamaterial nets by roughly $1\,\mu m$ in x- and y-direction. Albeit the displacements being rather small, force fields were determined. During the analysis, no difference of mean forces could be observed for individual cells and forces appeared to be rather evenly distributed as visualised for one cell on bowtie geometry in Figure 4.4D. To determine whether this was due to the specific cell type or indicated a general issue of the metamaterial scaffolds, human mesenchymal stem cells (hMSCs) were subjected to the different metamaterial scaffolds in collaboration with Natalie Munding (Tanaka group, Institute of Physical Chemistry, Heidelberg University, Heidelberg). The results of her experiments, published in 2023 (Munding et al., 2023), are visualised in Figure 4.5. For these cells, differences in mean force distribution were found for all three geometries with forces in x-direction being significantly higher than those in y-direction and overall higher forces on bowtie geometries. To determine whether this increase in forces was due to the stiffening of the net by suspension between the supporting beams or the anisotropic nature of the metamaterial properties, nets were rotated by 90°. For bowtie and brickstone, which are highly anisotropic in x- and y-direction, this should result in an inversed force distribution. For honeycomb geometries, the rotation should result in no effect, as the anisotropic axis corresponds to the diagonals of the net. Following the force field analysis of hMSCs cultured on the rotated geometries, these effects could indeed be observed. Thus, the difference in force distribution can be attributed to the metamaterial properties of the nets, confirming the suitability of metamaterials for mechano-regulation of the cellular response.

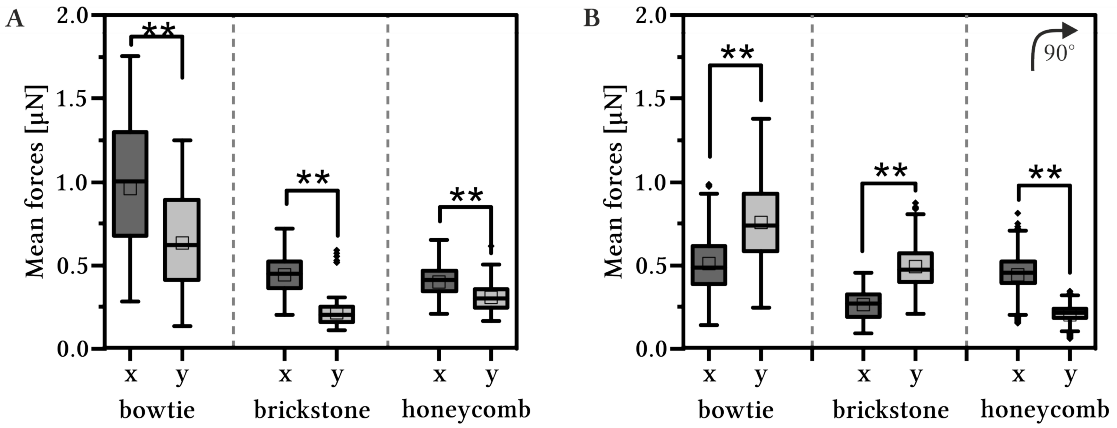

Figure 4.5: Force field calculations for hMSCs cultured on metamaterial nets. (adapted from Munding et al., 2023)
A Mean forces of hMSCs cultured on metamaterial nets with different geometries. Forces in x-direction are significantly higher than in y-direction, with overall highest forces on bowtie geometries. **B** Mean forces of hMSCs on 90° rotated metamaterial geometries. Force distributions changed in agreement with main axis of anisotropy for each geometry, leading to an inversion for bowtie and brickstone geometries while honeycomb geometries remained unaffected.

4.1.4 Analysis of Biological Response

In addition to the computational force analysis, the effect on biological mechanosensors was analysed. In order for cells to exert forces, they need to adapt their actin cytoskeleton. On the cell level, this often is reflected in a change of cell shape. Thus, spreading areas and aspect ratios were determined. On the subcellular level, the localisation of the YAP/TAZ complex was analysed. Depending on the degree of tension established by the focal adhesions, nuclear pores are opened allowing translocalisation of cytoplasmic YAP into the nucleus, where it acts as a transcriptional co-activator. Due to this tension-dependent localisation, the ratio of nuclear to cytoplasmic YAP can serve as an indicator of the degree of mechanical activation.
Simultaneously to shaping metamaterial properties, the microstructuring of the net introduces a different shape of adhesive areas. As cells are generally know to adapt to microstructured surfaces without metamaterial properties (Jeon et al., 2010; Linke et al., 2019), a non-deformable scaffold in the same geometry than the soft metamaterials was fabricated as a control. These stiff nets provide the same adhesion geometry, yet they prohibit experiencing of mechanical metamaterial properties by the cell as it can not deform the net. Thus, by the comparison of the soft to the stiff condition, the effect of the metamaterial properties can be separated from the adhesion geometry-derived ones.

4.1.4.1 Cellular Adaptation to Soft, Deformable Metamaterials

First, soft and deformable metamaterials were fabricated from IP-PDMS. In addition to the bowtie, brickstone and honeycomb geometries, blocks with the same size of the nets and a height of 12.5 µm were used as a control for a soft, homogenous substrates. The immunocytochemical stainings of REF cells cultured on these substrates are shown in Figure 4.6A.

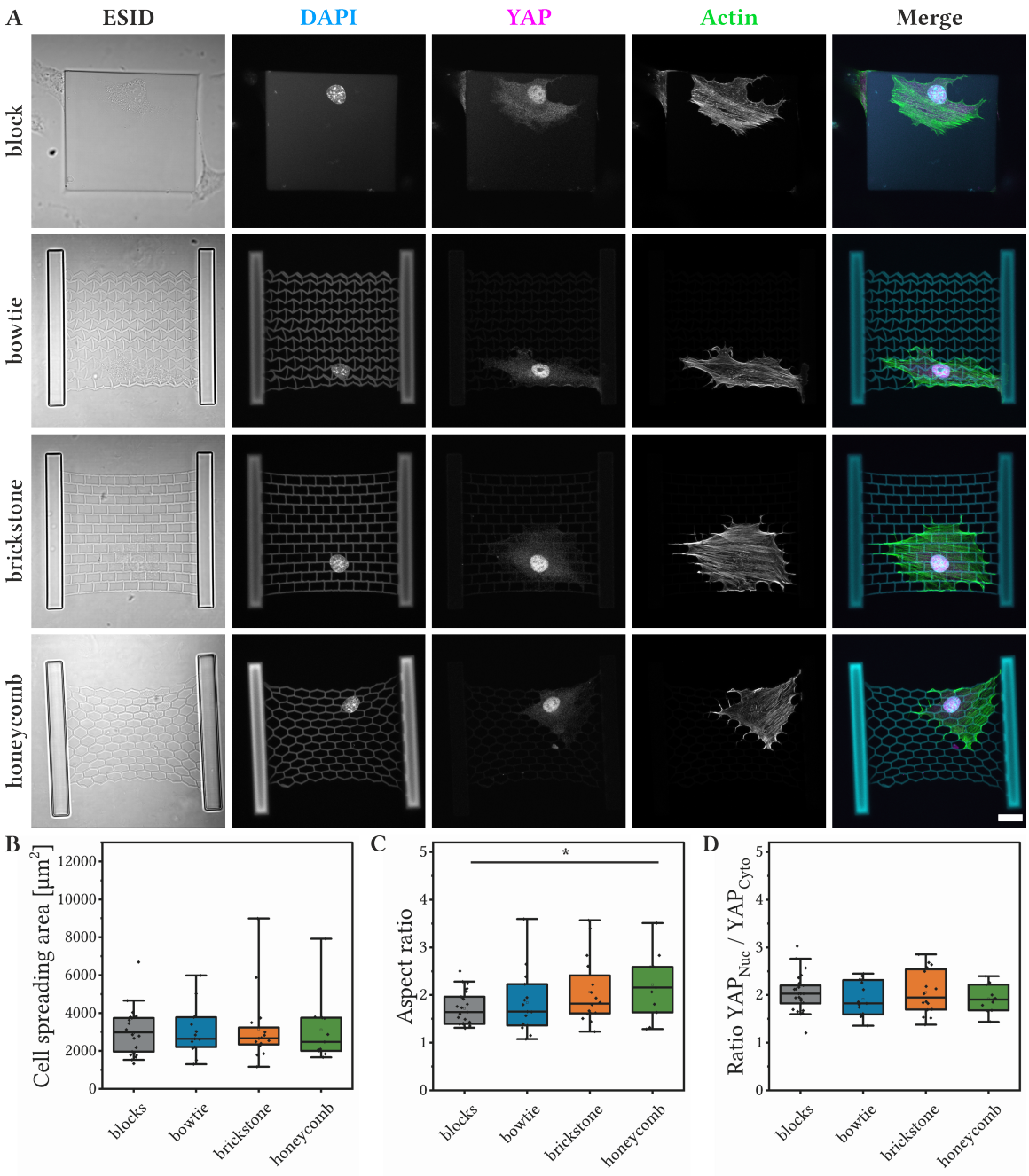

Figure 4.6: REF cells cultured on soft, deformable metamaterials.
A Immunocytochemical staining of REF cells cultivated on blocks and metamaterials fabricated from IP-PDMS. All cells mainly adhered to the printed IP-PDMS structures and formed stress fibres. Neither cell size or shape seem to be significantly different between the different conditions. Scale bar: 20 µm. **B** Mean cell spreading areas for REF cells on metamaterials and IP-PDMS blocks. As visible in the immunostaining, spreading areas are roughly constant for all conditions. **C** Mean aspect ratios for REF cells located on metamaterial geometries and blocks. As for the spreading area, aspect ratios are nearly the same for all conditions. Merely cells on honeycomb geometries appear significantly more elongated than on blocks. **D** Nuclear to cytoplasmic ratios of YAP. REF cells appear to experience the same degree of mechanical activation independent of the substrate. **B-D** $N \geq 3$, $n \geq 11$.

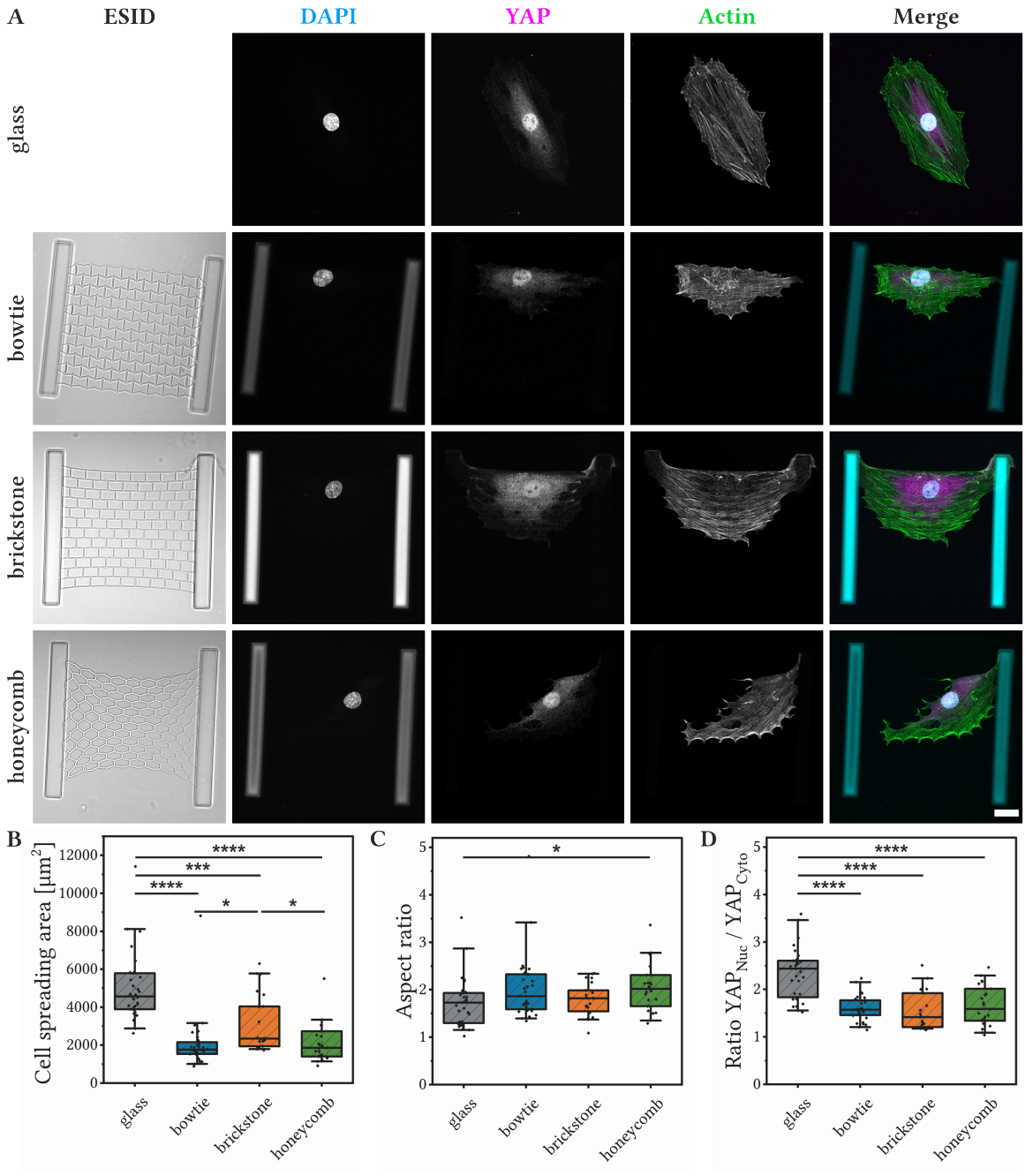

Figure 4.7: REF cells cultured on stiff metamaterial geometries.
A Immunocytochemical stainings of REF cells cultured on glass or stiff metamaterial geometries. As for IP-PDMS, cells adhered to the geometries and formed stress fibres. Scale bar: 20 µm. **B** Cell spreading areas of REF cells cultivated on stiff substrates. Cells cultured on homogenous stiff substrates showed significantly larger spreading areas than those on metamaterial geometries. When comparing the different geometries, cells on honeycomb nets were significantly larger than those on bowtie or brickstone. However, this difference in spreading did not lead to a difference in elongation, as visualised by the mainly equal aspect ratios in **C**. Again, only cells on honeycomb geometry appeared significantly more elongated than those on glass. **D** Mechanical activation of REF cells as determined by the ratio of nuclear to cytoplasmatic YAP. Cells cultured on glass experienced a significantly higher mechanical activation than those on metamaterial geometries, which again show equal levels of activation. **B-D** $N \geq 3$, $n \geq 21$.

The cells adhered to all three substrates and formed stress fibres as visible in the actin staining. From the actin staining, no striking difference in cell morphology can be observed, which is reflected in the nearly constant spreading area and aspect ratios in Figure 4.6B and C. Merely on honeycomb geometry, REF cells appear to be more elongated than on the control blocks with a weakly significant increase in aspect ratio of 0.6. From the YAP staining, the ratio of nuclear to cytoplasmic YAP was determined following the method described by Kuroda and colleagues (Kuroda et al., 2017). As visible in Figure 4.6D, the ratio is nearly the same for all conditions, indicating no additional mechanical activation of REF cells by the metamaterials.

4.1.4.2 Cellular Adaptation to Stiff Metamaterial Geometries

To disentangle the effect of altered adhesion geometry by the microstructuring from the experienced effective metamaterial properties of the deformable nets, stiff nets with the same geometry were fabricated from PETA, which possesses a Young's modulus of 3×10^6 kPa (Hippler et al., 2020). The respective Young's moduli and Poisson's ratios in dependy of the applied angle of force are given in supplemental Figure S1. Figure 4.7A shows representative immunocytochemical stainings of REF cells cultured on a homogenous stiff surface, in this case glass, and stiff metamaterial geometries. As for the soft metamaterials, REF cells adhered to the net and formed stress fibres. When analysing the cell spreading area, cells on glass were significantly more spread than those on the metamaterial geometries as visible in Figure 4.7B. Cells on brickstone geometries appeared to spread more than those on bowtie or honeycomb geometry. Despite these differences in spreading area, aspect ratios again showed no difference in elongation, except for cells on glass compared to those on honeycomb geometries. When determining the degree of mechanical activation based on YAP localisation, no difference between the individual geometries could be found but a strong increase of activation when cells were cultured on glass, depicted in Figure 4.7D. Interestingly, the ratio of nuclear to cytoplasmic YAP is around 1.5 for all metamaterial geometries and thus lower than the obtained value of roughly 1.9 for all conditions on soft materials. As cells were not able to deform PETA nets (see supplemental Figure S2), this reduced activation can not be traced back to mechanical metamaterial properties but rather is influenced by other means.

4.1.4.3 hMSCs and Metamaterials

As hMSC exhibited differences in force distribution, they were also analysed for morphological changes and activation in collaboration with Natalie Munding (Tanaka group, Institute of Physical Chemistry, Heidelberg University, Heidelberg). The results of the experiments are described in detail in Munding et al., 2023 and only summarised briefly here. For these cells, significant differences in spreading area, aspect ratio, as well as YAP distribution were found when cultured on soft metamaterials. As for the force field analysis, hMSC cultured on bowtie geometries exhibited the highest mechanical activation, reflected in the highest ratio of nuclear to cytoplasmic YAP which was in the same region as for culture on glass. When stiff geometries were used, these differences in activation were abolished and all conditions showed the same mechanical activation as for glass.

Taken together, the analysis of the biological response of REF cells and hMSC revealed a cell type-dependent reaction to the metamaterial scaffolds. Whereas REF cells seem to be largely unaffected by the effective metamaterial properties, hMSCs appear to react differently to the individual effective properties. When metamaterials geometries are fabricated from stiff PETA, these effects disappear in the case of hMSCs. On such scaffolds, however, REF cells exhibit reduced activation levels, indicating an effect of available adhesive area or its organisation. As the observed degree of activation resided even below those achieved on IP-PDMS scaffolds, an overall stimulating effect of metamaterials can not be excluded.

4.2 Influence of Structured Substrates on Cell Shape and Polarisation

As described above, the microstructuring necessary to generate metamaterials is accompanied with an alteration of the available adhesive area. While the effect of metamaterial properties on the cellular mechanoresponse is a relatively new field of study, it is well known that cells adapt to structured substrates (Coyle et al., 2022; Curtis & Wilkinson, 1997; Flemming et al., 1999; Jeon et al., 2010; Linke et al., 2019). In 2016, Fee and colleagues demonstrated an influence of aligned and randomly oriented nanofibres on cell orientation and expression of genes related to focal adhesion formation and actin polymerisation (Fee et al., 2016). Two of the drivers of the cytoskeletal reorganisation, necessary for orientation along such aligned substrates, are the isoforms NM IIA and NM IIB, which have been shown to polarise the cytoskeleton in response to substrate stiffness (Shutova et al., 2017). However, whether these isoforms are also involved in sensing the cellular microenvironment remains unclear.
To address this topic, U2OS cell lines lacking either NM IIA or NM IIB were cultivated on structured 2D and 3D substrates. The role of the two isoforms in adaptating to these environments was analysed *via* the ordering of the actin cytoskeleton, cell shape and polarisation. Cell seeding experiments and immunocytochemical stainings in the following sections were performed by supervised students as part of their bachelor or master theses. Where necessary, the acquired data was complemented with additional experiments.

4.2.1 Aligned and Random Gelatine Nanofibres as Structured 2D Substrates

For the 2D case, aligned and random gelatine nanofibres were chosen. The substrates were fabricated during a research stay at the group of Prof. Dr. Motomu Tanaka (Center for Integrative Medicine and Physics, Institute for Advanced Study, Kyoto University, Kyoto). Representative images of aGNF and rGNF together with the obtained surface coverage are given in Figure 4.8A and Figure 4.8B, respectively. Due to the fabrication process, aligned fibres cover significantly less surface than random ones.

U2OS wt, NM IIA KO and NM IIB KO cells were cultured on these substrates and stained for the actin cytoskeleton and the Golgi apparatus. The Golgi apparatus was chosen as a target, as it is located in front of the nucleus and in line with the leading edge in mesenchymally migrating cells, thus serving as an indicator of polarisation (Ridley et al., 2003). Figure 4.9 and Figure 4.10 show immunocytochemical stainings of cells cultured on aGNF and rGNF, respectively. As visible in Figure 4.9, cells seeded on aGNF exhibit an elongated morphology along the main fibre direction. The fibre direction is visualised in the binary images next to the immunocytochemical stainings. U2OS cells cultured on rGNF exhibit no clear orientation or shape of the cells. For both substrates, U2OS NM IIA KO cells, in contrast to wt and NM IIB KO cells, form only few pronounced stress fibres as typical for this cell line.

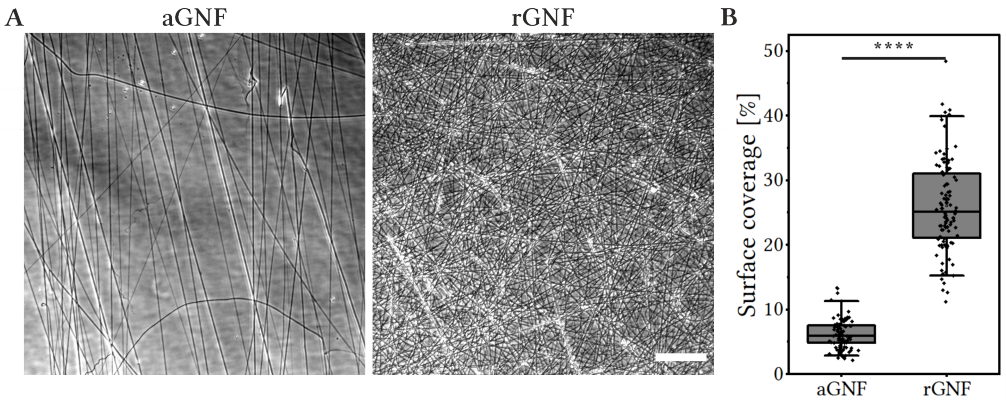

Figure 4.8: Mean surface coverage of aGNF and rGNF.
A Phase contrast images of aGNF and rGNF. Aligned fibres appear to follow one main direction with only few fibres facing other directions. Random fibres are oriented in all spatial directions and appear denser than aligned ones. Scale bar: 100 µm. **B** Mean surface coverage of aligned and random gelatine nanofibres. Random fibres cover three times more of the substrate area than aligned fibres. n≥68.

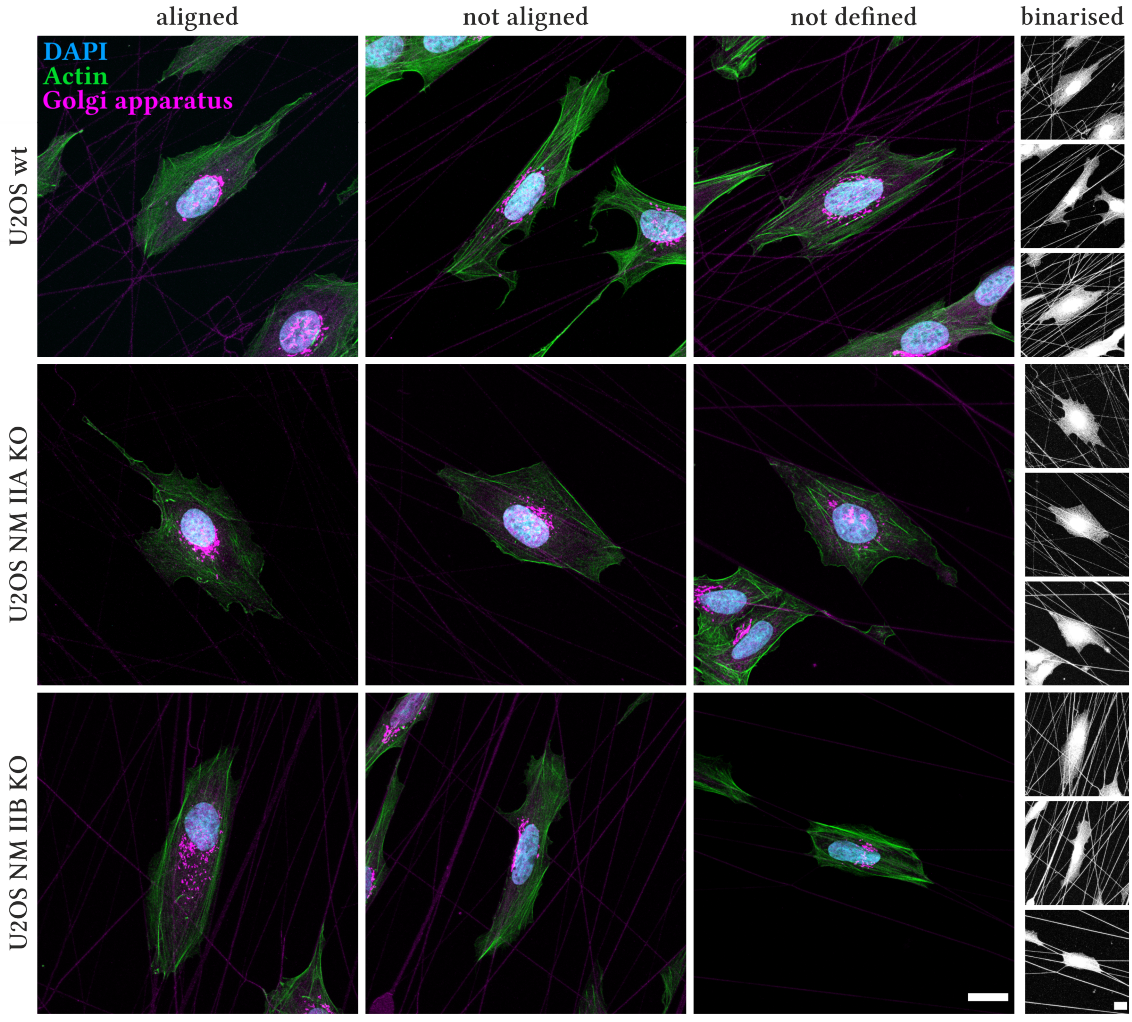

Figure 4.9: Immunocytochemical stainings of U2OS cells cultured on aGNFs.
All cell types exhibit an elongated cell shape, which corresponds to the main fibre direction. The main fibre direction is visible in the binarised images, which from top to bottom correspond to the stainings from left to right. Other than wt and NM IIB KO cells, NM IIA KO cells posses only few pronounced stress fibres. From the Golgi apparatus staining, three different localisations with respect to the nucleus and main cell body axis can be distinguished: aligned, not aligned and not defined. Scale bars: 20 µm.

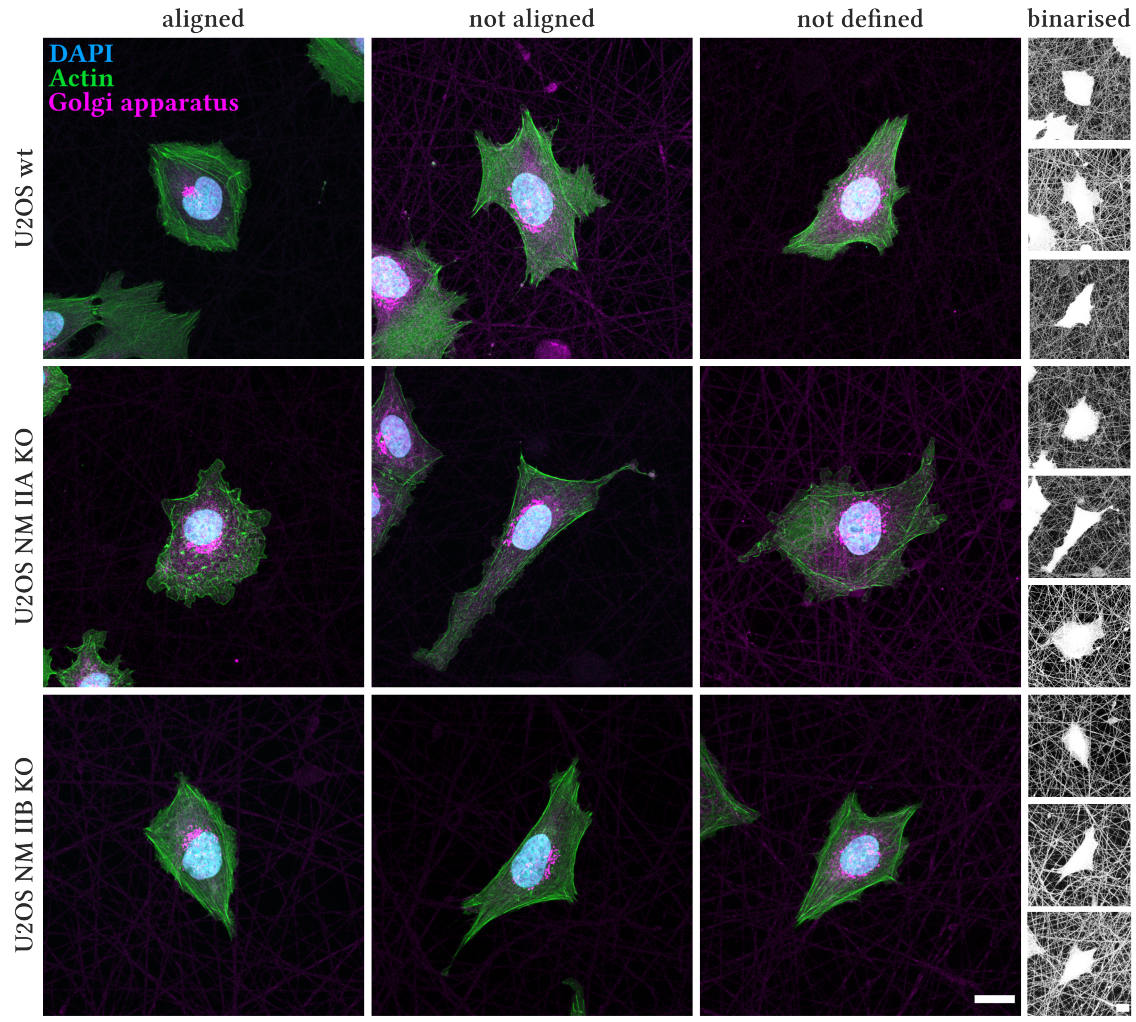

Figure 4.10: Immunocytochemical stainings of U2OS cells cultured on rGNFs.
Cells cultured on rGNF do not show a homogenous cell shape or preferred orientation. The fibre orientation is visible in the binarised images, corresponding from top to bottom to the stainings from left to right, respectively. Compared to wt and NM IIB KO, NM IIA KO cells exhibit only few stress fibres. Localisation of the Golgi apparatus with respect to the main cell axis und nucleus can be separated into three categories: aligned, not aligned and not defined. Scale bars: 20 µm.

When analysing the localisation of the Golgi apparatus with respect to the main cell body axis, being in line with the main fibre direction on aGNF, and the nucleus, three different categories can be determined:

(I) outside the nucleus and in line with the main cell body/fibre axis (aligned),
(II) outside the nucleus and not aligned with cell body/fibre axis (not aligned), and
(III) above the nucleus (not defined).

In the following, statistical evaluations of the cell shape, as given by spreading area and aspect ratio, the ordering of the actin cytoskeleton as well as the Golgi apparatus localisation are presented.

4.2.1.1 Cell Spreading Area and Elongation on Gelatine Nanofibres

The differences in cell shape were quantified on the basis of cell spreading area and aspect ratio, as depicted in Figure 4.11A and B, respectively.

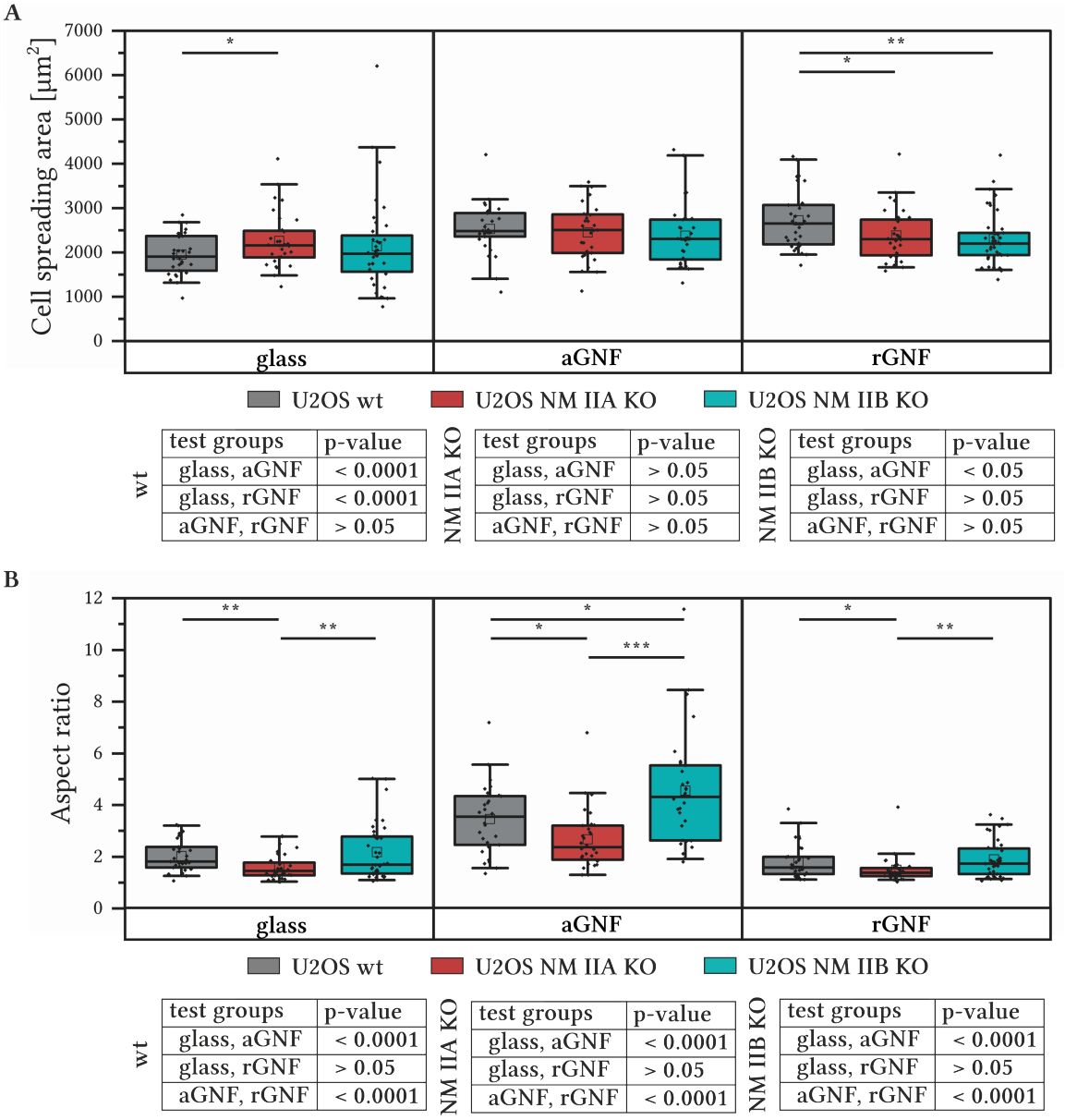

Figure 4.11: Mean cell spreading areas and aspect ratios for U2OS cell cultured on microstructured 2D substrates.
A Mean cell spreading areas and statistical analysis. On glass and aGNF, cell lines exhibit roughly the same cell spreading area. On rGNF, wt cells appear significantly more spread than KO cell lines. Regarding the impact of the substrates on the individual cell lines, wt cells appear significantly larger on gelatine nanofibres than on glass, whereas NM IIA KO and NM IIB KO cells exhibit no difference between the substrates. **B** Mean aspect ratios and statistical analysis. NM IIA KO cells appear less elongated compared to wt and NM IIB KO, independent of the substrate. Overall, all cells are significantly more elongated on aGNF, as indicated by the significant increase in aspect ratio. **A-B** N≥3, n≥27.

To allow comparison to standard culture conditions, cells were also seeded on glass surfaces. When comparing the different cell spreading areas between each cell line per substrate, cells cultured on

glass do not exhibit large differences in size between the different cell types. However, the difference appears to be weakly significant for wt and NM IIA KO cells on glass. For the case of rGNF, wt cells appear significantly more spread than both knock-out cell lines. On aGNF, no differences between the cell lines are visible.
Below the plot, the results of the statistical comparison of the three substrates for each cell line are given. For wt cells, the spreading area increases significantly for culture on either aGNF or rGNF. For both knock-out cell lines, the mean spreading area is roughly the same on all substrates.
When analysing the elongation of the cells by their aspect ratio, a few more differences become apparent. While wt and NM IIB KO cells exhibit equal aspect ratios on glass and rGNF, both are significantly more elongated than NM IIA KO cells on all substrates. For culture on aGNF, NM IIB KO cells appear significanytly larger than wt cells. In general, all cells cultured on aGNF appear to be more elongated, reflected in the overall significantly higher aspect ratio compared to glass and rGNF. The aspect ratio increased by a factor of 1.7-1.9 for wt and NM IIA KO cells and slightly more for NM IIB KO cells with a factor of 2.1-2.4. The comparison of the culture on glass and rGNF on the other hand revealed no significant difference.

4.2.1.2 Ordering of the Actin Cytoskeleton on Gelatine Nanofibres

Following the analysis of the cell shape, the intracellular organisation was of interest. For this, the orientation of actin fibres was analysed in collaboration with Danny Egic (Tanaka group, Institute of Physical Chemistry, Heidelberg University, Heidelberg), following a previously published procedure (Inoue et al., 2015; Yoshikawa et al., 2013). Essentially, actin fibres are identified and their angle determined with respect to the vertical image axis. In case of aGNF, the images were rotated such that the main fibre direction corresponds to the vertical axis. Figure 4.12A shows exemplary images with identified actin fibres, colour-coded by the respective angle. Gelatine nanofibre oritentation is schematically depicted in the upper left corner of each panel.
The statistical evaluation of actin fibre orientation is given in Figure 4.12B. On rGNF, actin fibres take a random orientation independent of the cell line. In contrast to this, an increased alignment of actin fibres with the main fibre direction is found on aGNF for all cell lines. This also holds true for NM IIA KO cells, which show a less pronounced alignment of fibres than wt and NM IIB KO cells. For the latter, the strongest alignment of actin fibres with the main fibre direction is found.

4.2.1.3 Polarisation Along aGNF and rGNF

Next, the polarisation of the cells was analysed based on the localisation of the Golgi apparatus relative to nucleus and the main cell axis. For aGNF, the latter corresponded with the main fibre direction, thus indicating the alignment along the fibres. The calculated percentages of each category are visualised in Figure 4.13A.
On aGNF, nearly the same amount of wt and NM IIA KO cells were aligned, whereas 10% more cells were aligned for NM IIB KO. In the case of rGNF, the fractions of polarised wt and NM IIB KO cells were reduced. Interestingly, NM IIA KO cells exhibited an increase of 4% in alignment. The fraction of not defined cells remained nearly the same for wt cells while being reduced for NM IIB KO

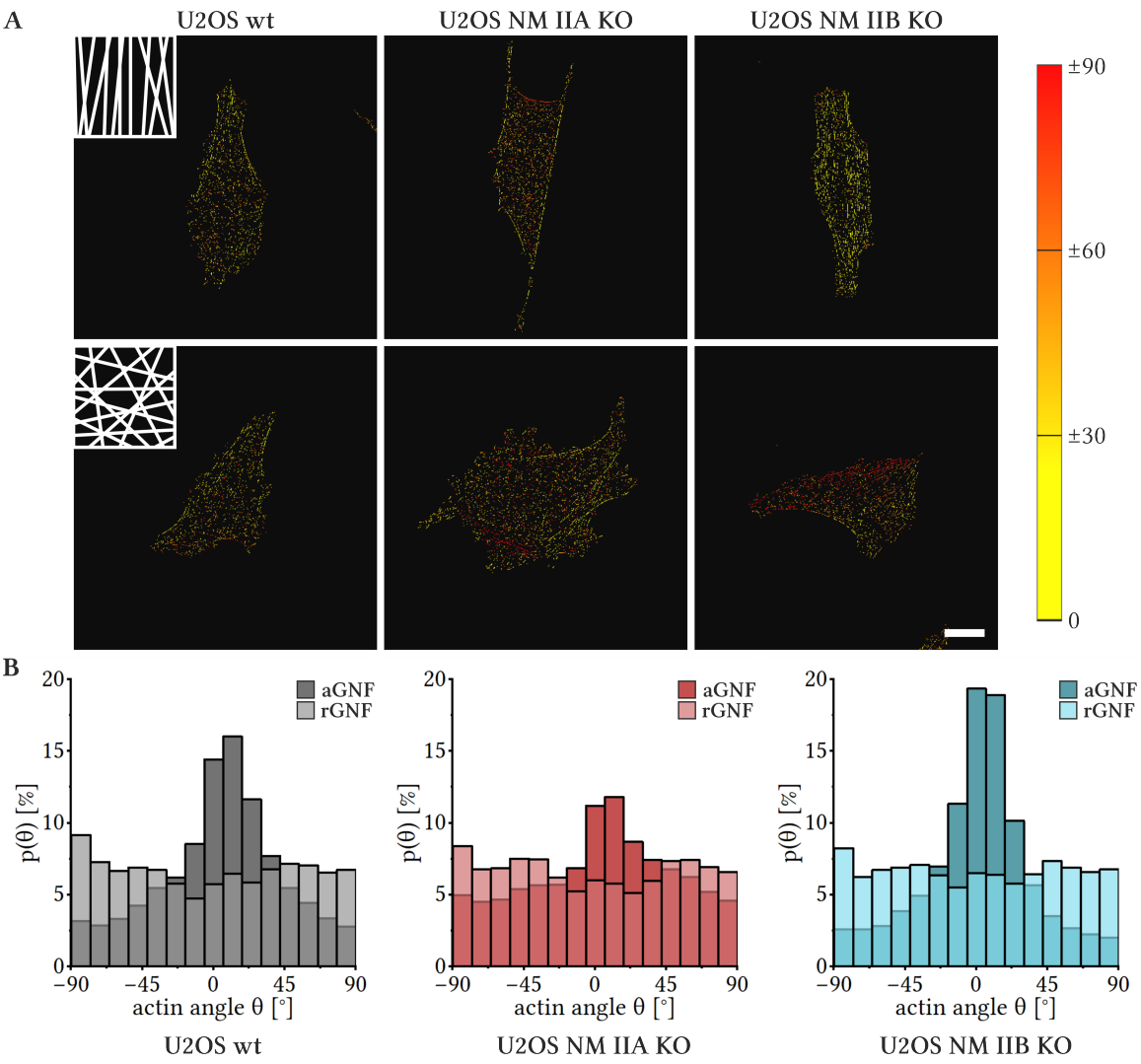

Figure 4.12: Actin fibre orientation with respect to substrate geometry.
A Exemplary images of analysis of actin fibre alignment with substrate geometry. The identified actin fibres are colour-coded according to the detected angle. The orientation of the fibres is given in the upper left corner of each panel, with aGNF corresponding to the vertical image axis. Scale bar: 20 µm. **B** Statistical distribution of the measured actin fibre angles. While all cell lines show an equal distribution of all angles on rGNF, actin fibres align with aGNF. The alignment is strongest for NM IIB KO cells and weakest for NM IIA KO cells. N≥3, n≥27.

and more than doubled for NM IIA KO. The statistical significance of the distribution was analysed by a χ^2-test, revealing a significantly different overall distribution on aGNF different than expected with a p-value ≤ 0.01.

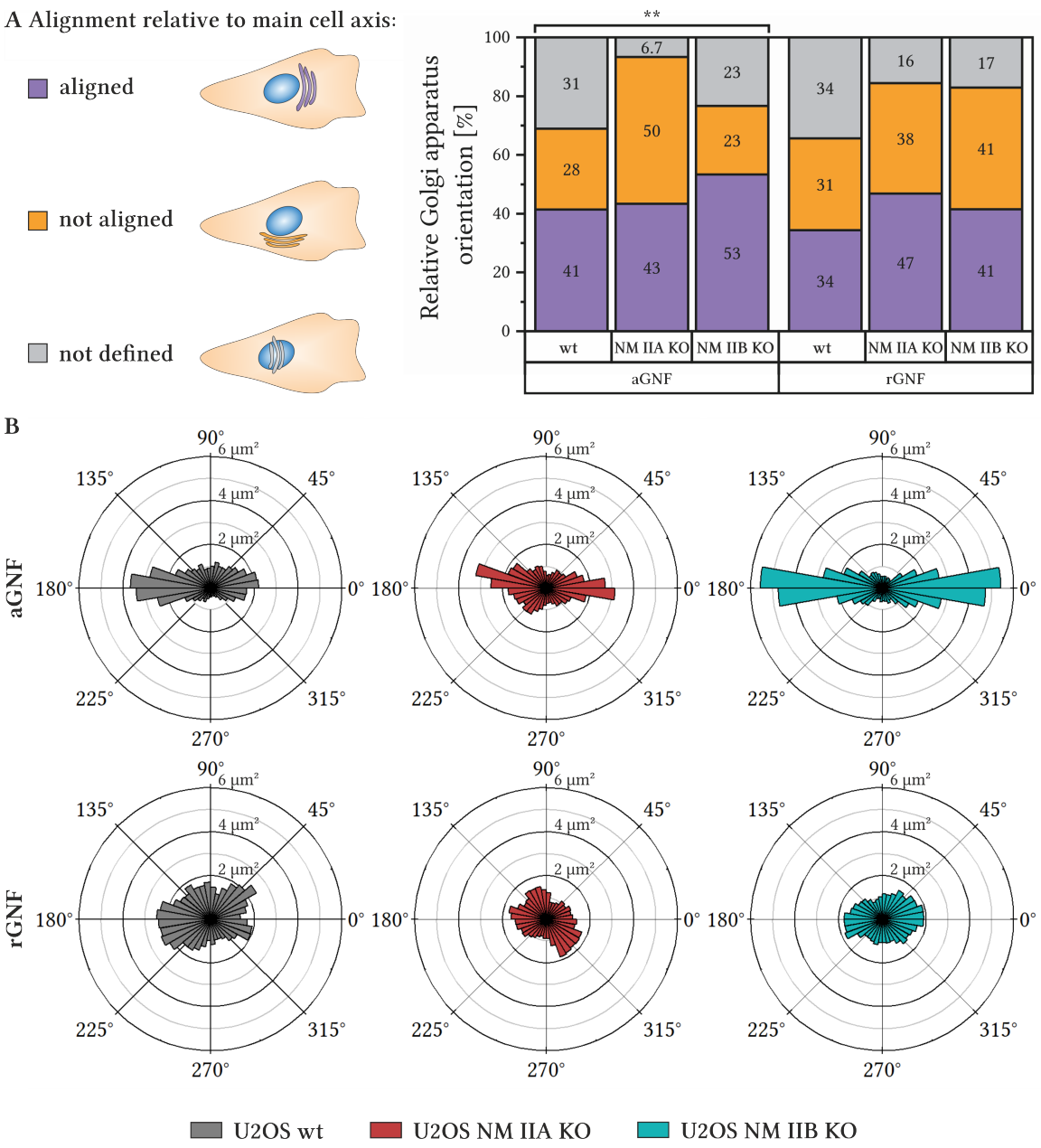

Figure 4.13: Golgi apparatus localisation of U2OS cells cultured on aGNF and rGNF.
A Percentages of cells with aligned, not aligned and not defined Golgi apparatus localisation. On aGNF, wt and NM IIA KO cells show the same fraction of aligned cells. For NM IIB KO cells, a 10% higher fraction of aligned cells was found. While no change in alignment was found for NM IIA KO cells cultured on rGNF, both wt and NM IIB KO cells exhibited a reduced fraction of aligned cells. The distribution on aGNF appears significantly different than expected with a p-value ≤ 0.01, as determined by a χ^2-test. **B** Area of Golgi apparatus per 10° radial segment. For aGNF, the main fibre direction was set to 0°. The Golgi apparatus is preferentially located along the fibre direction on aGNF, as visible by the increase in area around 0° and 180°. While this distribution is the clearest for NM IIB KO cells, they also show the least compact Golgi apparatus. For rGNF, also the Golgi apparatus is randomly oriented. The occupied area appears slightly larger in wt cells than for both knock-out cell lines. **A-B** N≥3, n≥27.

For a more detailed analysis of the Golgi apparatus distribution with respect to the main fibre direction, corresponding to the main cell axis on aGNF, its occupied area per 10° radial segment was analysed in collaboration with Danny Egic (Tanaka group, Institute of Physical Chemistry,

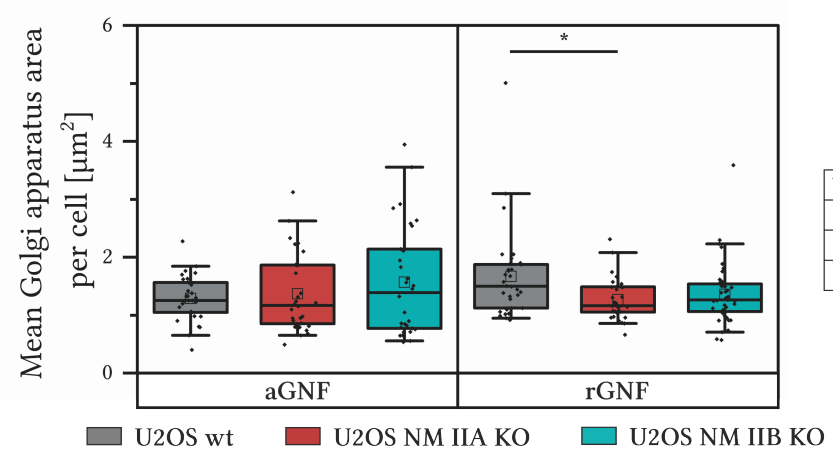

Two sample t-test aGNF vs. rGNF

test groups	p-value
wt	< 0.05
NM IIA KO	> 0.05
NM IIB KO	> 0.05

Figure 4.14: Mean Golgi apparatus area per cell
Cells cultured on aGNF exhibit no significant difference in mean Golgi apparatus area, although NM IIA KO and NM IIB KO cells show a broader dsitribution. For rGNF, the Golgi apparatus is significantly more compact within NM IIA KO than wt cells. While the mean Golgi apparatus area is not affected by the choice of substrate for both knockouts, it appears signidicantly more compact within wt cells cultured on aGNF. N≥3, n≥27.

Heidelberg University, Heidelberg). In case of aGNF substrates, the 0°/180° axis was aligned to the main fibre direction, whereas for rGNF it was fit to the vertical axis of the image. Originating from the centre of mass of the nucleus, the occupied area of the Golgi apparatus was measured per radial segment, depicted in Figure 4.13B. While the Golgi apparatus is preferentially located along the fibre direction on aGNF, it shows a random distribution on rGNF. For clearer visualisation, the percentile fractions of the area in line with the fibre directions are given in supplemental Figure S3. NM IIA KO cells resemble wt cells on aGNF, whereas NM IIB KO cells show a slightly stronger alignment with the main fibre axis and larger Golgi apparatus areas. On rGNF, no striking differences in Golgi apparatus distribution is visible. On closer inspection, the Golgi apparutus of wt cells appears to occupy slightly more area than for both knock-out cell lines, depicted in Figure 4.14. However, this difference is only significant for NM IIA KO cells. This indicates that overall NM IIB KO cells are able to compact their Golgi apparatus, but fail to do so on aGNF. Additionally, wt cells but neither knock-out cell line show a significantly more compacted Golgi apparatus on aGNF compared to rGNF, emphasising the necessity of both isoforms to maintain Golgi apparatus morphology.

In conclusion, all cell lines adapt to the nanofibre organisation, as demonstrated by the alignment of actin fibres with aGNF and their random distribution on rGNF. The choice of substrate seems to affect the spreading area of wt cells, whereas NM IIA KO and NM IIB KO cells remain largely unaffected. When comparing the individual cell lines to each other on the different substrates, weak significant differences can be found for NM IIA KO cells and wt cells on glass, as well as for wt and both knock-out cell lines on rGNF. However, the choice of substrate seems to affect the shape of all cell lines in the same way, independent of the NM II KO. All cells appear to be more elongated on aGNF than the other substrates, with NM IIA KO cells being less elongated

than wt and NM IIB KO cells. Regarding polarisation, NM IIB KO cells show increased alignment with aGNF but lower compaction of the Golgi apparatus compared to wt and NM IIA KO cells. Interestingly, depite an overall random distribution of the Golgi apparatus on rGNF, NM IIA KO cells exhibited an unimpeded alignment of it with the cell body while both NM IIB KO and wt cells were negatively affected.
Together these results imply that NM IIA and NM IIB both act as potential regulators of different aspects of cellular adaptation to substrate organisation. As the knock-out of neither NM II isoform completely abrogated the cellular adaptation, they likely act in concert in establishing the response to structured invironments.

4.2.2 3D Orthogonal and Parallel Collagen Fibre Networks

Following the experiments in 2D, the analysis was extended to the 3D case. For this, aligned and orthogonal collagen networks were purchased from 3DBioFibR. U2OS cells were cultured in these networks and analysed as for the 2D case. Figure 4.15 and Figure 4.16 show immunocytochemical stainings of U2OS cells cultured in parallel and orthogonal collagen fibre networks, respectively. As for aGNF, the cells showed an elongated morphology along the main fibre direction of parallel fibres. Fibre directions are visible in the grey scale images on the right hand side. In case of orthogonal fibres, cells mostly aligned with one of the two fibre directions. All cells formed stress fibres, with NM IIA KO exhibiting the least amount of fibres. Again, the Golgi apparatus localisation was categorised as aligned, not aligned or not defined, with one example each given for both fibre networks.

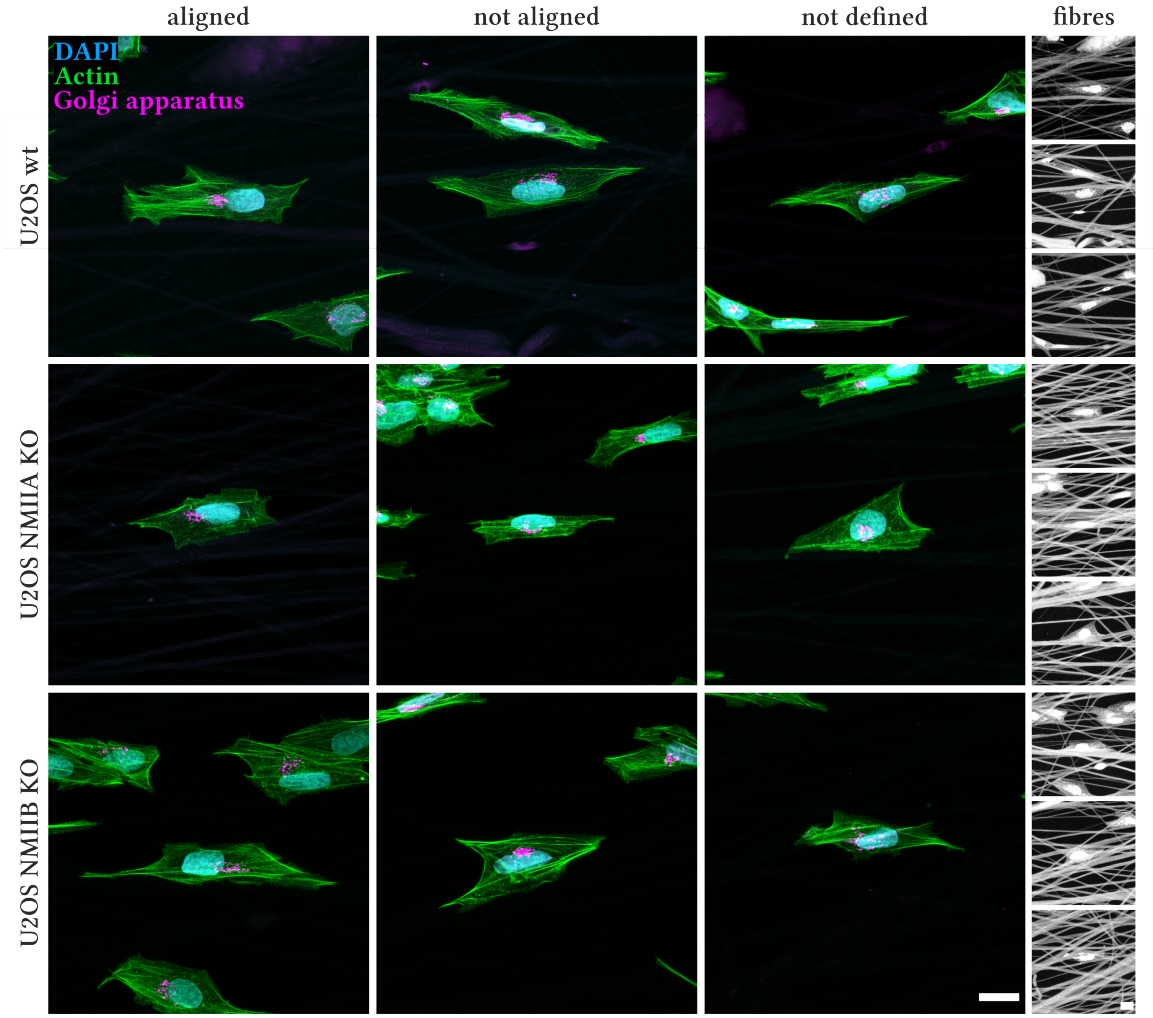

Figure 4.15: Immunocytochemical stainings of U2OS cells cultured within 3D parallel collagen fibres.
An elongated morphology along the main fibre axis is visible for all cell lines. The corresponding fibre directions are visible in the grey scale images corresponding from top to bottom with the stainings from left to right. All cells show a pronounced actin cytoskeleton, with NM IIA KO cells exhibiting the least amount of stress fibres. As for 2D substrates, three different categories of Golgi apparatus localisation were found: aligned, not aligned and not defined. Representative images for each cell line are given for each category. Scale bars: 20 µm.

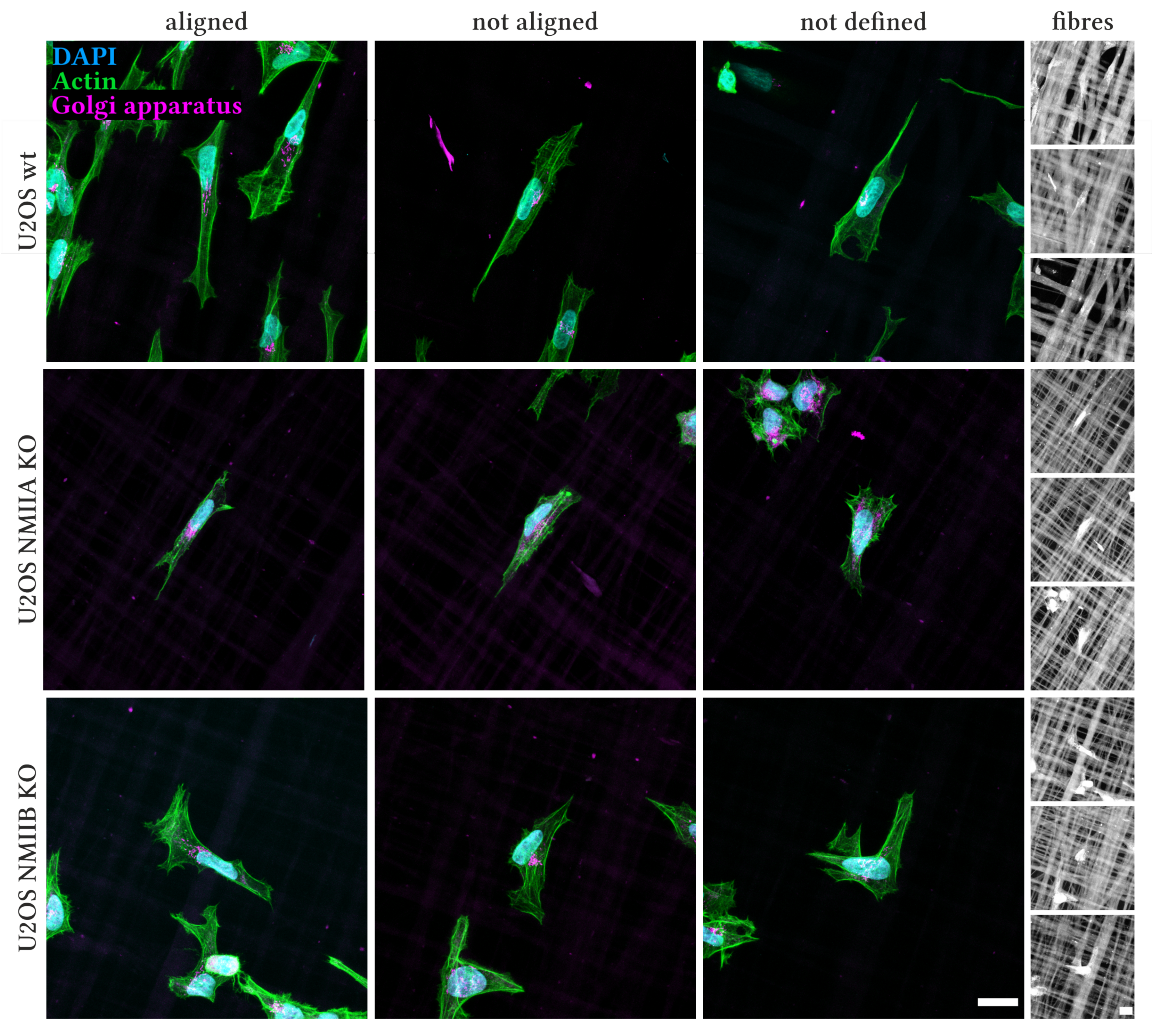

Figure 4.16: Immunocytochemical stainings of U2OS cells cultured on 3D orthogonal fibres. Cells mostly exhibit an elongated morphology along one of the two main fibre directions. In some cases, as visible for not defined NM IIB KO cells, cells elongated along both axis. All cells formed stress fibres, with NM IIA KO cells forming the least amount. The golgi localisation was categorised in aligned, not aligned and not defined as described before. Representative images for each category are given for each cell line. Scale bars: 20 µm.

4.2.2.1 Cell Spreading Area and Elongation in Structured 3D Fibre Networks

As for the 2D case, cell spreading areas and aspect ratios were analysed in the x-y-plane. The results are visualised in Figure 4.17A and B, respectively. Within parallel collagen fibres, all three cell lines spread equally with a slightly larger distribution of spreading areas for wt cells. Within orthogonal collagen fibres, the mean spreading area was significantly reduced for all cell lines and the measured areas show a smaller distribution. Additionally, NM IIA KO cells were significantly smaller than wt or NM IIB KO cells.

Regarding the aspect ratio within parallel fibre networks, NM IIA KO cells appear significantly less elongated than wt and NM IIB KO cells, as it was the case for the 2D substrates. For the orthogonal fibres, this relation changes: while wt and NM IIA KO cells remain largely unaffected, NM IIB KO cells exhibit a broader distribution and a reduced mean aspect ratio similiar to NM IIA KO cells.

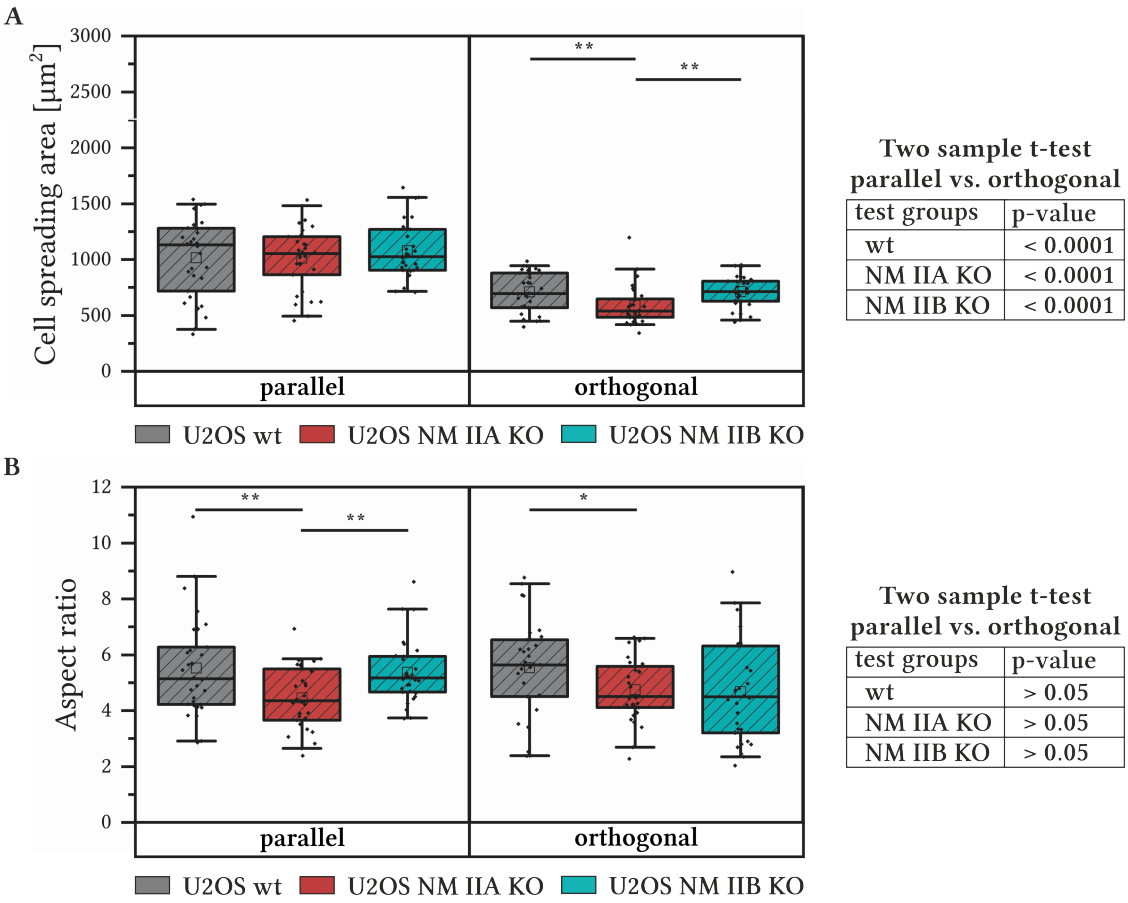

Figure 4.17: Mean cell spreading areas and aspect ratios for U2OS cells cultured within 3D collagen fibre networks
A Mean cell spreading areas within parallel and orthogonal fibre networks. Within parallel fibres, all cell lines exhibit the same spreading area. This area is significantly reduced within orthogonal fibres, with the highest decrease observed for NM IIA KO cells. Within these networks, the latter are significantly less spread than wt and NM IIB KO cells. **B** Mean aspect ratios for cells cultured within 3D fibre networks. NM IIA KO cells appear significantly less elongated than wt and NM IIB KO cells when cultured in parallel fibres. For wt and NM IIA KO cells, culture in orthogonal fibres appears to have no effect. On the other hand, NM IIB KO cells exhibit a reduced elongation similiar to NM IIA KO cells with a broader distribution. However, this effect appears to not be significant. **A-B** N=3, n=30.

However, this reduced elongation is not statistically significant as determined by a two-sided t-test.

4.2.2.2 Polarisation Within Defined 3D Fibre Networks

Following the analysis of the cell shape, the Golgi apparatus localisation with respect to the main cell body axis and the nucleus was quantified. The obtained percentages for each category are visualised in Figure 4.18A. While wt cells exhibit the same fraction of aligned cells on parallel and orthogonal fibres, the fraction of not defined Golgi apparatus positioning increased by 7%. Within parallel fibres, both NM IIA KO and NM IIB KO cells show a roughly 10% higher fraction of aligned cells than the wt. However, within orthogonal fibre networks both of these cell lines show a reduction of aligned cells by roughly 20% accompanied by an increase in not aligned and not defined Golgi apparatus positioning. Within these networks, both knock-out lines appear

less polarised than wt cells, with a roughly 10% lower fraction of aligned cells. The statistical significance of the distribution was analysed by a χ^2-test, revealing a significantly different overall distribution than expected within parallel fibres.

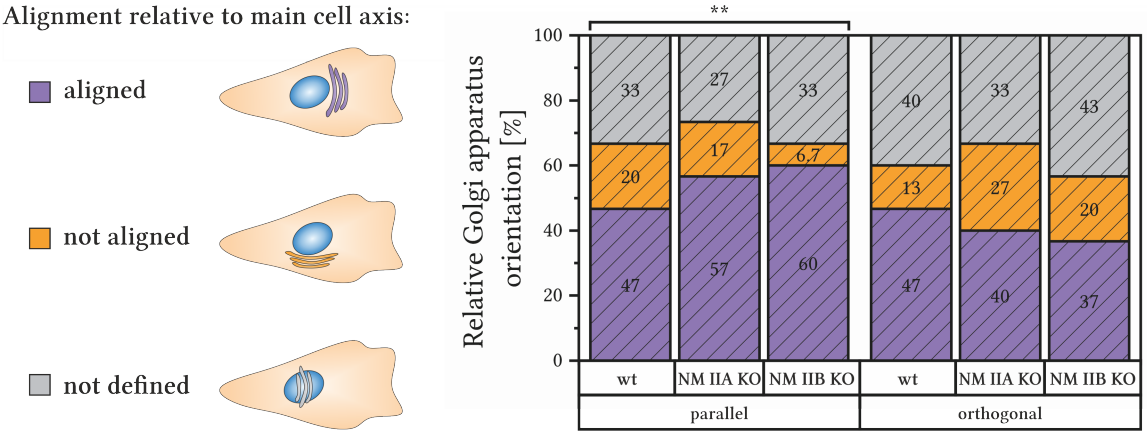

Figure 4.18: Golgi apparatus localisation of U2OS cells cultured within 3D collagen fibre networks.
Percentages of cells with aligned, not aligned and not defined golgi apparatus localisation. Within parallel fibre networks, wt cells appear less aligned than NM IIA KO and NM IIB KO cells. While both of the knock-out cell lines appear less aligned within orthogonal fibre networks, the wt cells remains unaffected. N=3, n=30. The distribution within parallel fibres appears significantly different than expected as determined by a χ^2-test.

To summarise, wt cells appear unaffected in alignment and elongation by both fibre networks. Merely the spreading area decreased within orthogonal fibres, as was the case for both knock-out cell lines. Both knock-out cell lines aligned more with parallel fibre networks than wt cells and were negatively affected by orthogonal ones. As for the 2D case, this implies that both isoforms act in concert in wt cells to achieve adaptation to their microenvironment.

4.3 Confinement in 3D Environments

In contrast to plain 2D surfaces, cells entering fibrous 3D networks, such as the parallel and orthogonal fibre arrangements used here, do not only experience the ordering of the fibres but are also affected by the limited space between the individual fibre layers. This additional constraint of 3D environments is referred to as confinement and has previously been shown to affect cell migration (Y. J. Liu et al., 2015). Depending on the degree of confinement, cells can adapt their migration from a mesenchymal mode to an adhesion-independent amoeboid type, a process deemed MAT. NM II and actin have been shown to play a central role in this process; however, the role of the individual NM II isoforms is not yet clear.

While MAT *in vivo* might occur as a gradual process rather than a switch, most experimental approaches apply confinement rather apruptly or can not monitor migration at the same time. Inspired by the work of Holle and colleagues (Holle et al., 2019), who found a self-directed MAT of cancer cells entering microchannels, an experimental set-up was designed to monitor migration under gradually increasing confinement. The general concept is depicted in Figure 4.19A.

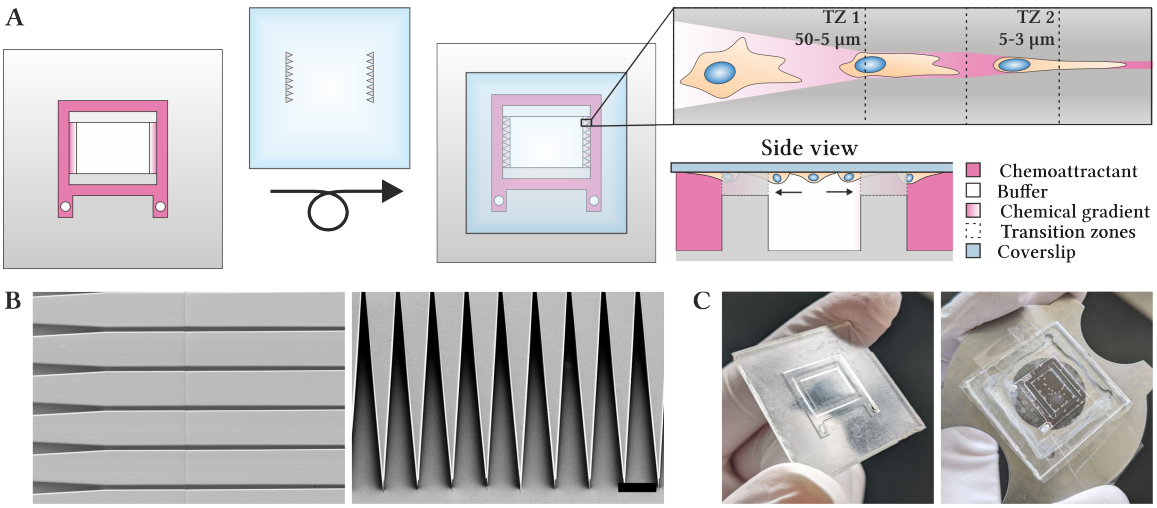

Figure 4.19: Chemotaxis chamber with confining microchannels.
A Schematic depiction of a chemotaxis chamber design with microchannels for analysis of migration under increasing confinement. The chemotaxis chamber comprises two reservoirs which are connected by a bridging area. Across this bridge, exchange between the two reservoirs is possible and hence allows formation of a stable gradient. The chamber is sealed with a cover slip, onto which migration channels are printed by 3D laser microprinting. In the assembled chamber, these channels are positioned within the bridge area to facilitate directional migration along a chemotactic gradient into the gradually confining channels. The confinement increases within two transition zones (TZ), beginning with a transition from 50 µm to 5 µm in TZ1, followed by 5 µm to 3 µm in TZ2. **B** Scanning electron microscopy images of microchannels. The channels are free of debris. Scale bar: 50 µm. **C** Photos of an unsealed chemotaxis chamber (left) and a fully assembled one after imaging for 30 h (right). Although some of the medium evaporated during imaging, indicated by the formation of air bubbles, the two reservoirs are still sufficiently filled.

It comprises microchannels with transition zones and a chemotaxis chamber for application of chemotactic gradients where necessary. The chemotaxis chamber, based on the Insall-chamber published by the group of Robert Insall in 2010 (Muinonen-Martin et al., 2010), is formed by two separated reservoirs, which are connected by two bridge areas with defined height. In a sealed

chamber, these areas allow for the formation of a stable chemotactic gradient, until an equilibrium between the two reservoirs is reached. The chemotaxis chamber is sealed with a glass coverslip, onto which microchannels are printed that are placed directly within the bridge areas. The microchannels themselves possess two transition zones, which introduce increasing confinement the further a cell enters the microchannel. The first transition zone starts with a width of 50 µm (and thus no confinement) and over a distance of 400 µm decreases to a width of 5 µm. The second transition zone narrows down from 5 µm to 3 µm over a distance of 200 µm. Both transition zones are followed by 200 µm of straight microchannels.
Migration channels fabricated by 3D laser microprinting were free of debris as visualised in Figure 4.19B. The scanning electron microscopy images were kindly provided by Jannis Weinacker (Wegener group, Institute of Applied Physics, KIT, Karlsruhe). Figure 4.19C shows a chemotaxis chamber before assembly and a fully assembled chamber without migration channels after over 30 h of imaging. As evident by the formation of air bubbles, some of the imaging medium evaporated, yet the chamber is still sufficiently filled. Thus, the chamber is suitable for long-term imaging.
Next, cells were seeded on cover slips with migration channels. The chamber was assembled without introducing a chemotactic gradient to test whether cells would enter the channels on their own. Figure 4.20A shows the migration of a cell located away from the channels for comparison. Unfortunately, cells within the migration channels did not enter past the first transition zone, sometimes even turning around as visible in Figure 4.20B. The mean velocity as well as migration trajectories of cells outside of and within migration channels are given in Figure 4.20C and D, respectively. As clear from the trajectories, cells within channels were restrained to the channel dimensions but did not migrate past the end of the first transition zone, with no linear migration distance being longer than 400 µm. With the velocity being not significantly different, it appears migration was not affected so far.

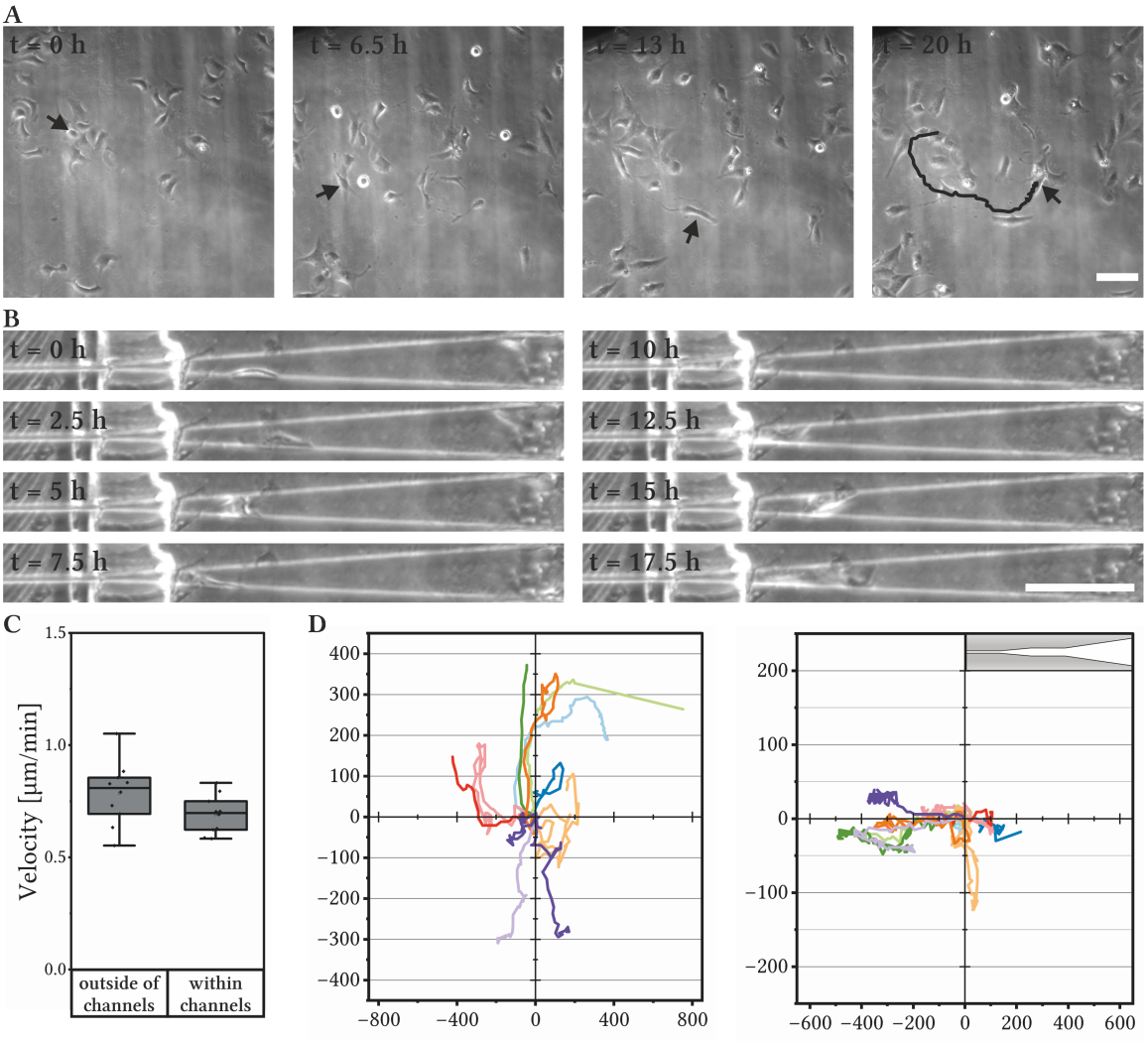

Figure 4.20: Timelapse images of U2OS cells in a chemotaxis chamber without chemoattractant.

A Migration of a U2OS cell outside of the microchannels. The tracked cell is marked by an arrow in the individual frames. The last frame depicts the whole migrated path. Scale bar: 100 µm. **B** Migration of a U2OS cell within a microchannel. Despite the cell entering the 5 µm wide zone after 10 h, it turned back and migrated away from the confined region after 12.5 h. Scale bar: 100 µm. **C** Mean velocity of cells migrating outside and within microchannels. No significant difference in mean velocities were found. **D** Trajectories of tracked cells migration outside (left) and within migration channels (right). While cells migrating within microchannels are restricted to the channel's area, no cell migrated past the initial 5 µm confinement, sometimes even turning back within the channel. **C-D** N=1, n=10.

To facilitate entering of the cells into the confined regions, a chemotactic gradient can be applied. In order to quantify the slope of such a gradient, the outer reservoir was filled with 10 µM Fluorescein-5(6)-isothiocyanat in 100 mM Tris-HCl. The bridge area was imaged for 22 h to monitor the formation of the gradient. As visible in Figure 4.21A, over time the intensity of flourescein in the inner reservoir increased. The measured intensities across the reservoirs and the bridge area are given in Figure 4.21B for several time points. After an increase in slope after 6 h, the gradient slowly returned to its orginal slope around 18 h from which on it remained constant. The intensity at the beginning of the gradient is roughly two times greater than at the end of the gradient. A linear fit for values along the bridge area revealed a slope of -0.129 AU/µm.

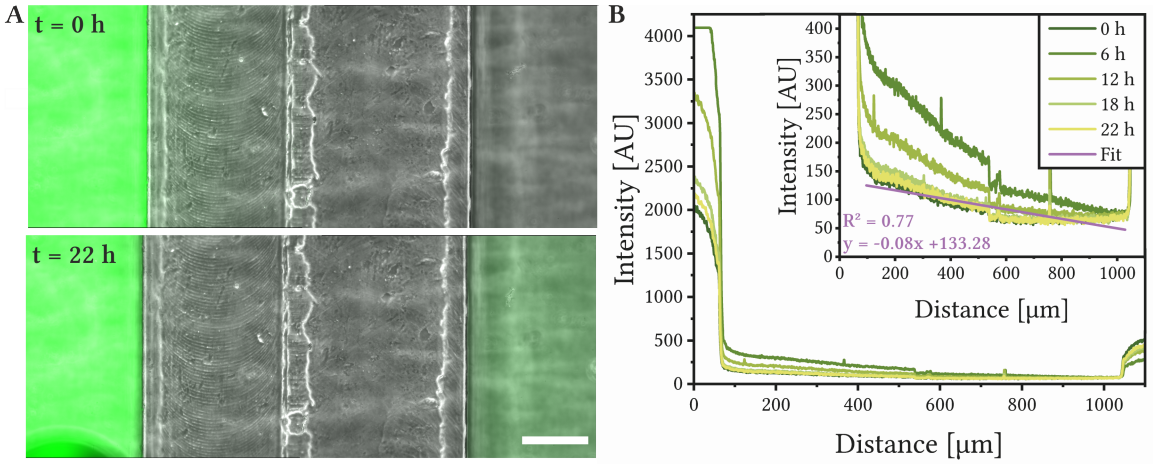

Figure 4.21: Characterisation of gradient in chemotaxis chamber.
A Visualisation of gradient formation along bridge area using fluorescein at the beginning of imaging and after 22 h. As visible by the increased fluorescence in the right reservoir after 22 h, the fluorescein was able to diffuse to the previously not-fluorescent reservoir. Scale bar: 200 µm. **B** Fluorescein intensities across the bridge area over time. After an increase in slope after 6 h, the gradient slowly returned to the inital distribution after 18 h and stayed constant after that. The measured intensity at the end of the bridge was roughly half of the initial intensity.

Upon characterisation of the gradient, different chemoattractants were tested (data not shown). To this end, no suitable concentrations for the tested chemoattractants were found due to time restrictions, but is part of ongoing work.

Chapter 5

Discussion

Within this thesis, different aspects of the cellular microenvironment and how they affect the cellular mechanoresponse were analysed by three different approaches. First a metamaterial-based system was developed to analyse the cellular mechanoresponse in the context of rare material properties such as a negative Poisson's ratio. In the second part, the influence of substrate geometry on cellular morphology and polarisation was determined based on 2D and 3D fibre networks. As NM II-mediated contractility is associated with both processes, the analysis was centred around NM IIA KO and NM IIB KO cells. The last part focussed on creating an experimental setup to allow for LCI of cells during the transition from mesenchymal to amoeboid migration within gradually confining microchannels. In the following, the individual findings of each approach are discussed.

5.1 Metamaterials Provide a Platform for Mechanostimulation of Cells

With the ongoing work in the field of mechanobiology, today it is clear that the cellular microenvironment influences cells by more than just stiffness. Following this insight, researchers identified other material properties such as the Poisson's ratio as potential influencing factors of the cellular mechanoresponse. In contrast to modulating stiffness, e.g. by altering crosslinking of hydrogels, this material parameter is not so easily accessible and adjustable. The vast majority of natural materials exhibit positive Poisson's ratios, whereas negative (or auxetic) Poisson's ratio materials are rare and thus a limiting resource. Although a rare material property, different biological tissues such as skin, tendons or cancellous bone were characterised as auxetic (Gatt et al., 2015; Lees et al., 1991; Williams & Lewis, 1982). Despite its occurence *in vivo*, the lack of applicable materials or experimental approaches to recreate auxetic behaviour *in vitro* thus far restricted research of the Poisson's ratio's effect on cells.

In the past decade, a few attempts have been made to fabricate auxetic materials for cell studies, taking advantage of so-called metamaterial properties (Flamourakis et al., 2020; C. Wang et al., 2022; W. Zhang et al., 2013), which can be introduced to a bulk material by appropriate microstructuring *via* two-photon polymerisation. Building on this concept, a workflow for detailed analysis of the cellular mechanoresponse was developed in this work, including fabrication of metamaterial scaffolds, the extraction of forces from timelapse images and the analysis of biological markers of mechanoactivation.

5.1.1 Metamaterials Can Induce a Mechanoresponse in Human Mesenchymal Stem Cells

In Section 4.1, the development and detailed procedure of the aforementioned workflow is described. In brief, free-hanging metamaterial nets are fabricated from a highly elastic photoresist called IP-PDMS by 3D laser microprinting. Cells cultured on these scaffolds interact with the metamaterial and the resulting dynamic deformations of the metamaterial net by individual cells are monitored during LCI. From these timelapse images, displacement vectors of distinct features of the net can be extracted, which serve as the basis for force field extraction by FEM under consideration of the bulk materials properties. The obtained force field vectors provide the exerted force components in x- and y-direction for each timepoint and selected feature of the analysed timelapse series.
One drawback of the used scaffold design is the necessity for supporting beam structures to create free-hanging metamaterial nets. When hMSCs were seeded on the scaffolds, they exhibited significantly increased forces along the x-axis for all tested geometries (Munding et al., 2023). Due to the suspension of the metamaterial nets between the non-deformable beams, a stiffening is introduced in the x-axis which limits the deformability of the metamaterial. Further, the tested geometries exhibit anisotropic distributions of the metamaterial properties. To verify that the difference in force distribution originates from the effective material properties rather than the support structure, nets with 90° rotated geometry were fabricated, resulting in a change of orientation of metamaterial properties in case of bowtie and brickstone geometries. As hMSCs cultured on the latter two exhibited inverted force distributions, the supporting beams appear to present only a minor influence on the cellular mechanoresponse. Thus, the fabricated metamaterials were able to introduce different responses in hMSCs as demonstrated by the overall increased forces on bowtie geometries and the impact on other components of the mechanosensory machinery like actin fibres, focal adhesions and cytoplasmic YAP. This was further confirmed by an equal YAP distribution across all conditions when seeding cells on stiff metamaterial geometries (Munding et al., 2023). Similar to the results on free-hanging nets, Wang and colleagues observed an effect of bowtie metamaterials on cells in form of large deformations of their 3D bowtie scaffolds and more compact colonies of hMSCs derived from human induced pluripotent stem cells (C. Wang et al., 2022). Although this confirms the potential of metamaterials to influence cell behaviour, whether the cells react to the different effective properties or sensed the anisotropic distribution of those remains a subject to further research.

To conclude, while previously reported results on the effect of auxetic metamaterials on different cell lines focussed on visual inspection of cell morphology, the workflow presented here allows for spatial and temporal analysis of cellular forces. The fabricated soft metamaterials were able to induce a mechanoresponse in hMSCs, which could be demonstrated both by (physical) force field analysis and biological indicators. Thus, the presented workflow paves the way for comprehensive studies, considering both physical and biological perspectives. The hence obtainable insights into cellular contractility add a new dimension to the biological observations made so far and thus may contribute to disentangling effective material properties and cellular mechanoresponse.

5.1.2 Rat Embryonic Fibroblast Cells Do Not Differentiate Between Soft Metamaterial Geometries

In addition to the results on hMSC published in Munding et al., 2023, the mechanoresponse of REF cells was analysed in the course of this work. In contrast to hMSCs, these cells were able to achieve only minor deformations of the metamaterial nets and an initial force field analysis yielded no difference in force distribution. To nonetheless verify that metamaterial substrates do not influence the cells' mechanoresponse, morphological descriptors such as cell shape and aspect ratio were quantified together with the ratio of cytoplasmic YAP, which is a well established indicator of mechanoactivation. REF cells seeded on blocks and metamaterials made from IP-PDMS exhibited no difference in spreading area and YAP distribution. Merely cells on honeycomb metamaterials appeared significantly more elongated than those on the control blocks.
Overall, the equal levels of YAP activation on all soft conditions reveal no effect of effective metamaterial properties on the mechanoactivation of REF cells, as implied by the initial force field analysis. In contrast to hMSCs, the cues from the metamaterials seem to be overwritten by the softness of the substrate. This indicates a different sensitivity for material properties, depending on the cell type. Before further discussion of this effect, a few descriptors of material properties need to be defined. In biology, materials are often characterised by their elasticity or stiffness, which are at times used interchangeably. In general, stiffness refers to the materials resistance to deformation and thus is not as clearly defined, while elasticity equals the Young's modulus which is related to but not identical to stiffness. Both phrases are used according to this definition in the following.
Turning back to cell type specific responses to the mechanical microenvironment, in case of hMSCs an impact of matrix elasticity ranging from 0.1-40 kPa on differentiation was found (Engler et al., 2006). This elasticity-dependent differentiation is precedented by durotactic migration towards stiffer regions, indicating a regulatory influence of substrate stiffness on MSC behaviour and fate (Tse & Engler, 2011). This durotaxis was shown to depend on the strength of the stiffness gradient, with gradients as shallow as 1 Pa/µm up to steep increases of 100 Pa/µm affecting MSCs differently (Vincent et al., 2013). Fibroblasts on the other hand were shown to be affected by stiffness but not elasticity of the substrate (Tong et al., 2017). They exhibit increasing actin crosslinking and cellular stiffness for substrates with a shear modulus range of 0.5-20 kPa (Solon et al., 2007). When cultured in 3D hydrogels with stiffness gradients, fibroblasts align differently depending on the substrate stiffness and remodel the surrounding matrix to achieve stiffnesses of 3-27 kPa (F. Zhao et al., 2024). These characterisations imply a relatively high sensitivity of MSCs to their mechanical microenvironment, whereas REF cells appear to react more to the general deformability of the substrate. During durotaxis, cells sense the mechanical properties of their microenvironment with the help of focal adhesions and actomyosin contactility, as demonstrated for sensing of different stiffnesses. More precisely, focal adhesion distribution and strength together with NM II activity mediate spatiotemporal actin organisation, which in turn affects focal adhesion patterning *via* NM II-mediated contractility directed along these actin fibres (Gupton & Waterman-Storer, 2006). This interplay of focal adhesions and the actomyosin network enables sensing of stiffness differ-

ences within the ECM, thus facilitating durotaxis (Plotnikov et al., 2012; Yeoman et al., 2021). On the other hand, the sensed stiffness affects the adhesive and contractile machinery of cells. While some cell types spread or migrate more on stiffer substrates, others do so on softer ones (Huang et al., 2022; Isomursu et al., 2022; Sunyer & Trepat, 2020). One framework aiming at describing this interdepence of cellular contactility and ECM properties is the so-called molecular clutch model, reviewed in detail by several articles and summarised in the following (Elosegui-Artola et al., 2018; Fortunato & Sunyer, 2022). Here, focal adhesions are represented by clutches which are connected to the retrograde actin flow. On soft substrates, these clutches are only weakly engaged, resulting in low contractile forces. Opposed to this, clutches are highly engaged on stiff subtrates as the retrograde actin flow is counteracted by the high resistance of the substrate, resulting in increased tension and ultimately release of the clutch which can only support a certain degree of force. Following this reasoning, forces increase with substrate stiffness until maximised for an optimal substrate stiffness. Further increase in substrate stiffness beyond this point results in reduced forces as clutches become destabilised. Although this behaviour was observed for some cell types, others exhibit a continuously positive correlation of cellular forces and substrate rigidity (Bangasser et al., 2017; Califano & Reinhart-King, 2010; Chan & Odde, 2008; Ghibaudo et al., 2008). The latter can be explained by additional stabilisation of focal adhesions under tension as described in Section 1.2.1, thus obscuring the effect predicted by the molecular clutch model (Elosegui-Artola et al., 2016). In addition to substrate stiffness, other factors such as density of binding sites and NM II-mediated contractility, regulating the actin retrograde flow, influence the mechanosensitivity of the clutch. As presented in this work, hMSCs but not REF cells cultured on soft metamaterials were able to deform them, indicating a lower contractility of REF cells. Thus, they experience more resistance of comparably soft IP-PDMS metamaterials than hMSCs. This results in a shift of the optimal stiffness towards softer materials compared to hMSCs and renders them insensitive to the effective material properties. On the other hand, hMSCs can withstand higher substrate stiffnesses due to their increased contractility, leading to a shift of their stiffness optimum towards higher stiffnesses. Consequently, the range of stiffnesses they can differentiate is broader than those of REF cells, allowing hMSCs to differentiate between the different metamaterials upon their deformation. Due to this increased sensitivity for stiffness, they might also be more sensitive for different Poisson's ratio materials. Most natural materials exhibit a positive Poisson's ratio and thus expand perpendicular to the axis of compression. Assuming the cell only contracts along one axis, the expansion of the material in the perpendicular axis counteracts the inward-facing actin retrograde flow resulting in a local 'stiffening' and thus a potentially higher engagement of the clutches, schematically depicted in Figure 5.1. For lower or negative Poisson's ratios this effect is supposedly reduced or even inverted. Due to their high sensitivity, hMSCs may be able to sense this local difference in material resistance and adapt accordingly.

Taken together, the observations of REF cells and hMSCs on metamaterial geometries point towards a different sensitivity of cell types towards their microenvironment. According to the molecular clutch model, these differences in adaptation to the mechanical microenvironment can be attributed to differences in contractility and thus different optima for stiffness. This emphasizes the critical role of cellular contractility in sensing aspects of the mechanical microenvironment.

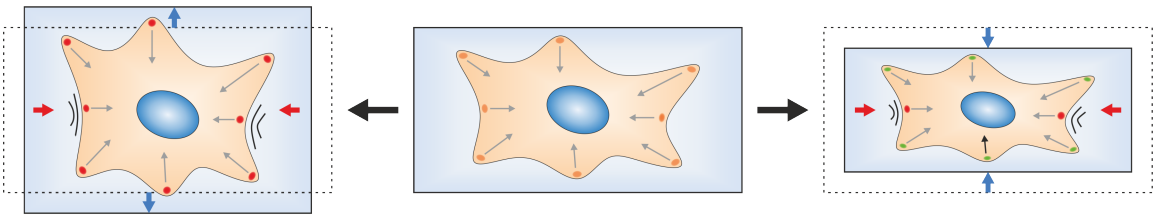

Figure 5.1: Clutch engagement in reponse to material deformation.
Upon cellular contraction along the horizontal axis, clutches in this direction become more engaged (red) due to the resistance they experience by the substrate. The direction of cellular contraction and thus compression of the material is indicated by red arrows. For positive Poisson's ratio materials (left), compression of the material results in simultaneous expansion in the perpendicular direction (blue arrows). This leads to a local increase in clutch engagement, as the expansion acts in the opposite direction to the retrograde actin flow (grey arrows). In contrast to this, compression of negative Poisson's ratio materials (right) along the horizontal axis results in compression in the perpendicular axis (blue arrows). Thus, clutches become less engaged (green) as the material moves in the same direction as the retrograde actin flow, resulting in a lowered material resistance.

5.1.3 Microstructuring Overrides Other Mechanostimulation of Rat Embryonic Fibroblast Cells

In addition to the soft metamaterials, cells were seeded on stiff metamaterial geometries to determine the effect of microstructuring and allow its decoupling of effective metamaterial properties. Interestingly, while hMSCs are equally mechanically activated on glass and stiff metamaterial geometries, REF cells exhibit reduced nuclear YAP localisation and cell spreading areas on the metamaterial geometries. Even more so, the activation appears to be lower than on the soft metamaterial conditions, indicating an enhanced effect of substrate patterning over general stiffness. For better visualisation, the relative change on soft and stiff conditions is given in Figure 5.2. While the control cells show a higher spreading and nuclear YAP localisation on the stiff condition, cells on metamaterial geometries overall appear more spread and mechanically activated on the soft conditions. Merely cells on brickstone geometry show no difference in spreading area.
In general, REF cells react to the different material stiffnesses of IP-PDMS and glass as visible in the control condition, where REF cells spread more on stiff than on soft materials. Consequently, cells cultured on metamaterial geometries made from PETA, which with a Young's modulus of 3 GPa is four orders of magnitude stiffer than IP-PDMS (Hippler et al., 2020), should spread more than on IP-PDMS. Yet, cells on stiff brickstone geometries exhibit the same spreading areas. Moreover, cells cultured on bowtie and honeycomb geometries show a reduction in spreading area compared to soft metamaterials. Thus, another parameter seems to influence cell spreading in addition to stiffness. Although the spreading area was not comparatively analysed in detail in previous works, an impact of stiff metamaterials on cell spreading was reported (W. Zhang et al., 2013). One factor introduced with the microstructuring to achieve metamaterial properties is the patterning of the substrate. As cells on IP-PDMS blocks and metamaterials exhibit the same behaviour, it appears like REF cells on one hand react the same to all soft substrates and on the other are affected by the patterning in case of the stiff substrates. This implies a stiffness-dependent sensing of substrate patterning, which is enhanced for stiffer substrates and absent on softer ones.

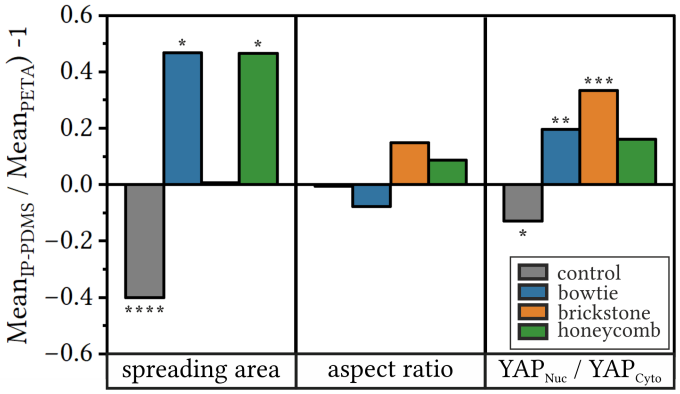

Figure 5.2: Relative change in spreading area, aspect ratio and YAP localisation on soft and stiff metamaterial geometries.
Control cells cultured on glass or blocks of IP-PDMS exhibit significantly increased spreading and more nuclear YAP for the stiff condition. For all conditions, cells exhibit no significant change in elongation. On metamaterial geometries, cells on brickstone geometry remain unaffected, whereas cells on bowtie and honeycomb geometries appear significantly more spread on the softer condition. Regarding the mechanical activation, cells cultured on stiff bowtie and brickstone geometries exhibit significantly higher fractions of nuclear YAP.

Indeed, cell spreading is controlled by the micropatterning of the substrate, affecting stress fibre localisation in reponse to the initial adhesion site (Kassianidou et al., 2019). On patterns of 1.2 µm squares, cells adapt their shape for spacings of 2-25 µm. Additionally, cell size increases with the surface coverage of adhesive area, with 15% coverage as the lower limit for cell spreading (Lehnert et al., 2004). All these different effectors are also present in the substrates used here: microstructuring is introduced to achieve metamaterial properties, non-adhesive areas in form of gaps lead to spacings of adhesive areas in the range of 5-15 µm and the adhesive area covers 22-33% of the metamaterial nets' areas. While this might serve as an explanation for altered spreading on stiff metamaterial geometries, the question remains why cells on soft materials remain unaffected by the micropatterning. Again for this case, the molecular clutch model provides a good starting point: beyond the optimal stiffness, cellular forces are drastically reduced, which can be obscured by stabilisation of focal adhesions, e.g. by talin unfolding. Consequently, when this stabilisation of focal adhesions is reduced, cellular forces and thus mechanical activation are reduced as well. For better visualisation, the correlation between substrate stiffness and cellular forces according to the molecular clutch model is given in Figure 5.3.

For the metamaterial geometries presented here, such a destabilisation of focal adhesions might be due to altered actin fibre organisation as a result of the micropatterning. As described above, focal adhesion strength and distribution affect actin fibre organisation, which in turn regulates focal adhesion patterning (Gupton & Waterman-Storer, 2006). Thus, the altered focal adhesion geometry and actin stress fibre organisation might lead to a destabilisation of focal contacts compared to continuous substrates. In case of soft metamaterials, the destabilising impact of the substrate patterning might be reduced as their stiffness is close to or within the stiffness optimum. For stiff materials on the other hand, this impact is increased as increased breakage of clutches can not be counteracted, resulting in forces even below those exerted on soft materials. Both cases are exem-

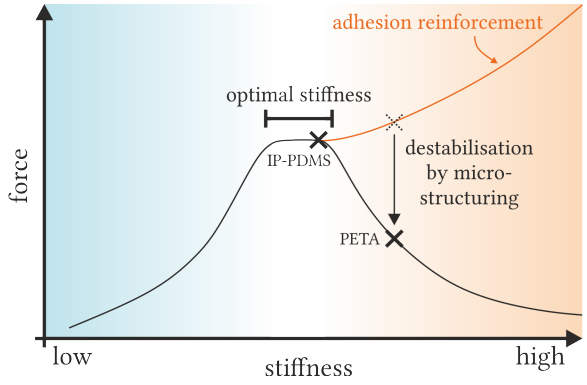

Figure 5.3: Effects of focal adhesion destabilisation based on the molecular clutch model. (adapted from Fortunato and Sunyer, 2022)
According to the molecular clutch model, the destabilisation of clutches beyond the optimal stiffness can be obscured by adhesion reinforcement (orange line). If this reinforcement is impaired due to destabilisation of adhesion complexes by e.g. microstructuring, otherwise stabilised clutches again can not resist increased substrate stiffness. Thus, for stiff metamaterial geometries made from PETA this results in an overall reduction in forces. In case of soft metamaterials made from IP-PDMS, this effect is not present as clutches are less dependent on adhesion reinforcement and thus are unaffected by the micropatterning. Thus, the cells react mainly to the substrate stiffness resulting in equal behaviour on continuous and patterned substrates.

plarily marked in Figure 5.3. This results in a stiffness-dependent sensing of the microstructuring, ultimately leading to both reduced mechanical activation and altered spreading behaviour.
The altered spreading behaviour might also serve as an additional reason for reduced nuclear localisation of YAP on stiff bowtie and brickstone geometries. When cells are restricted to smaller adhesive areas, YAP was found to be cytoplasmic rather than nuclear (Dupont et al., 2011; Nardone et al., 2017; Wada et al., 2011). While YAP localisation is regulated by a variety of different mechanical cues, it is also a target of Hippo signalling which facilitates cytoplasmic retention of YAP upon activation (Dasgupta & McCollum, 2019; Low et al., 2014). Although Hippo signalling is commonly known to regulate contact inhibition in highly confluent cell cultures, it was shown to be activated depending on cell spreading and polarity (Fu et al., 2022; Wada et al., 2011). Despite the expected increase of nuclear YAP on stiff materials, the reduction in spreading area on stiff metamaterial geometries might be sufficient to overcome the stiffness cue. This results in cytoplasmic retention of YAP, which leads to a ratio of nuclear to cytoplasmic YAP even below the levels achieved on soft substrates.

In conclusion, despite REF cells not reacting to the effective material properties of the presented soft metamaterials, they appear strongly affected by the micropatterning of stiff substrates. On these substrates, the cell spreading and nuclear YAP localisation is reduced even beyond the degree observed on soft materials. This stronger mechanoresponse of cells on soft metamaterials is potentially due to a stiffness-dependent sensing of substrate patterning. As soft materials probably do not provide enough mechanical resistance to move past the optimal stiffness range, the effect of micropatterning remains absent with cells solely reacting to substrate stiffness. The stiff micropatterns on the other hand provide such resistance, thus allowing the micropatterning to

induce a cellular response. In case of the metamaterial geometries presented here, a potentially unfavourable adhesion geometry leads to a reduction in cellular forces and cell spreading, which in turn leads to cytoplasmic retention of YAP. Albeit the REF cells do not react to the effective material properties targeted by the experimental approach, they still are affected by micropatterning in an unforeseen stiffness-dependent way. This stresses the multitude of factors which influence the cell's response to its microenvironment, which require careful analysis of the observed effects.

5.2 NM II-Mediated Contractility in Contact Guidance and Polarisation

As demonstrated by the altered behaviour of REF cells in dependency of substrate patterning and stiffness discussed in the previous section, cells can sense and adapt to the organisation of their microenvironment. This influence of substrate geometry or topography on cellular behaviour is referred to as contact guidance. While this phenomenon was already described in the last century, it is still not fully understood today (Curtis & Clark, 1990; Harrison, 1912; Weiss, 1934). A mechanism proposed by Ray and colleagues in 2017 identified the spatial restriction of focal adhesions by the substrate as a key factor in aligning the actin cytoskeleton with the underlying geometry, ultimately resulting in anisotropic cellular contractility and thus guided elongation of the cell (Ray et al., 2017). While focal adhesion orientation and actin fibre alignment are commonly accepted to regulate contact guidance, the role of cellular contractility is discussed ambiguously. To contribute to this discussion, fibrous 2D and 3D networks were employed to determine the roles of NM IIA and NM IIB in contact guidance. The according results described in section Section 4.2, obtained by culturing knock-out cell lines on structured substrates, are discussed in the following.

5.2.1 NM IIA and NM IIB Regulate Different Aspects of Cellular Adaptation to Substrate Geometry Based on Their Dynamic Behaviour

Actin organisation is closely linked to the cell morphology (Pollard & Cooper, 2009). Thus, actomyosin contractility, generating intracellular forces and bundling actin filaments into stress fibres, is a key driver of stabilising cell morphology. Especially knock-out of NM IIA was shown to drastically affect cell shape and actin fibre formation, resulting in irregular morphology with numerous thin protrusions and only few remaining actin stress fibres (Weißenbruch et al., 2021). Despite this strong association with actin, there is no common consensus on whether NM II-mediated contractility plays a role in contact guidance (Kubow et al., 2017; Lee et al., 2016; J. Wang & Schneider, 2017; Zhovmer et al., 2019). To determine the effect of NM IIA and NM IIB on the cellular adaptation to aGNF and rGNF, first the morphology was analysed by means of cell spreading and aspect ratio, and the ordering of the actin fibre network determined.

When analysing the cell spreading area and aspect ratio of cells cultured on aGNF and rGNF, a reduced response was found for NM IIA KO cells. In contrast to wt and NM IIB KO cells, NM IIA KO cells spread the same on either fibre network or glass. Additionally, they appear less elongated than both other cell lines, despite an overall increase of elongation on aGNF. This difference in spreading and elongation is most likely due to the lack of contractility upon knock-out of NM IIA. In wt cells, NM IIA acts as an initiator of minifilament formation, thus contributing to the formation of stress fibres (Weißenbruch et al., 2021). Although NM IIB can form minifilaments in absence of NM IIA, only few pronounced stress fibres are present upon NM IIA KO. Considering the model of contact guidance of Ray and colleagues, cell spreading and elongation along a pattern occurs due to the alignment of stress fibres and resulting anisotropy of cellular tension induced by spatial control of focal adhesions (Ray et al., 2017). In case of NM IIA KO, not only the amount of stress

fibres is reduced but they also appear to be less well aligned with the nanofibre geometry. Without the highly dynamic NM IIA, few stress fibres can be formed to generate the necessary tension and the spatial orientation of focal adhesions can not be translated into stress fibre alignment. This function is even more evident for the case of NM IIB KO: here, actin fibres are even more aligned with the nanofibre direction than for the wt. Furthermore, the cells appear strongly elongated on aGNF, surpassing the increase of elongation observed for wt cells. This overshooting response can be attributed to the loss of NM IIB's regulating influence on NM IIA. While NM IIA initiates minifilament formation, allowing step-wise incorporation of NM IIB, the enrichment in NM IIB in turn hinders further incorporation of NM IIA. This dampens the fast contractility generation of NM IIA, preventing overshoots and instead stabilising contractility, and leads to the characteristic distribution of the two isoforms in polarised cells (Shutova et al., 2017; Weißenbruch et al., 2021; Weißenbruch et al., 2022).

Together, this stresses the importance of the interplay between NM IIA and NM IIB in creating and maintaning contractility, which appears crucial for sensing and adapting to substrate geometry. In general, the roles of NM IIA and NM IIB in contact guidance appear to follow those already known from migration analysis and force studies. The fast NM IIA-mediated contractility is crucial to translate geometric cues into contractile responses. NM IIB on the other hand is required to stabilise this response and prevent overshooting reactions. Without this interplay, cells either do not respond to geometric guidance cues or exhibit too high susceptibility.

5.2.2 3D Substrates Lead to a Reduced Effect of NM IIB Knock-Out on Cell Elongation

As contact guidance was shown to be present in 3D fibre networks (J. Kim et al., 2021; Provenzano et al., 2008), the question arises whether NM IIA and NM IIB modulate the cellular response to substrate cues in the same way as on 2D substrates. Thus, in addition to 2D gelatine nanofibre substrates, 3D collagen fibre networks with parallel and orthogonal orientation were used to analyse the cell morphology.
As described in the previous section, NM IIB KO leads to a stronger elongation of cells along aGNF compared to wt cells. Interestingly, this overshooting response of NM IIB KO cells is not present for cells cultured in 3D networks. Here, they behave no different than wt cells regarding cell spreading and elongation within parallel fibre networks. In orthogonal networks, however, NM IIB KO cells appear less elongated, albeit the difference being not significant probably due to the high variation in the data points. For this case, NM IIB KO cells exhibit the same mean aspect ratio as NM IIA KO cells, which are again less elongated than wt cells. The dampening of the NM IIA-mediated contractility overshoot of NM IIB KO cells in 3D fibre networks might be due to an increased fibre thickness (see supplemental Figure S4) providing more adhesive area, as well as the added third dimension. In contrast to the 2D aGNF, cells experience resistance from the collagen fibres not only basally, but also apically and sideways. Together, this distributes the short-lived NM IIA-mediated contractility to more directions and area, thus reducing the output in the individual directions. In parallel fibre networks, this results in equal elongations as wt cells. In orthogonal

networks, again introducing more directional cues and adhesive area in form of perpendicular collagen fibres, elongation is further reduced to levels of NM IIA KO cells. As before, the latter show reduced elongation compared to the wt, with no difference between parallel or orthogonal fibre arangement. One might reason that also in the case of parallel vs. orthogonal fibres the stronger directional cue of the parallel fibres should enhance elongation as visible for the 2D case; yet no difference is visible. This is probably due to the same effect that dampens the contractile overshoot upon NM IIB KO, namely the added spatial directions and increase in adhesive area which dilute the effects observed for 2D. However, other than for the 2D case, NM IIA KO cells exhibited an increase in spreading within parallel fibre networks, reaching the same levels as wt and NM IIB KO cells. While the added third dimension reduces anisotropic effects, the added parallel adhesion sites help with stabilisation of focal contacts and thus spreading. In the case of orthogonal fibres, this parallelisation is interrupted by perpendicular fibres, resulting in overall less spread cells. Due to the nearly abolished contractility of NM IIA KO cells, they are more susceptible to the loss of stabilising factors and thus spread less than wt and NM IIB KO cells.

In summary, compared to the 2D case, the effects appear dampened in 3D, indicating a partial rescue of the knock-out induced spreading defect by the added dimension. Despite the reduced effects of the knock-outs, both isoforms appear to modulate cell spreading and elongation similarly to the 2D case. This again emphasizes the central role of NM II in contact guidance.

5.2.3 NM II Influences Golgi Apparatus Morphology *via* Actin Ordering

In addition to aligning with substrate geometry, cells were also shown to polarise and migrate in the direction of geometric cues (Leclech & Villard, 2020; Théry, Pépin, et al., 2006; Théry, Racine, et al., 2006). One indicator of such a polarisation is the positioning of the Golgi apparatus, which is positioned in front of the nucleus and towards the leading edge in mesenchymally migrating cells. This orientation in turn is postulated to stabilise cell polarisation and migration by directing vesicular transport towards the migratory direction, granting spatial control of polarisation by delivering compounds to the respective cell end (Yadav et al., 2009). In this context, a strong interdependency of microtubules and the Golgi apparatus was found. While microtubules were identified as key regulators of Golgi apparatus organisation, the Golgi apparatus itself acts as a nucleation site for microtubules which provide a network for directed vesicular transport (Rivero et al., 2009; Zhu & Kaverina, 2013). However, microtubules are not the sole regulators of Golgi apparatus localisation. The presence of actin adaptor proteins, actin crosslinkers and Rho-GTPases at the Golgi membrane, as well as defects in actin organisation additionally affecting Golgi apparatus positioning and morphology, imply a potential interdependence of actin organisation together with actomyosin contractility and the Golgi apparatus as observed for micotubules (Egea et al., 2013; Lázaro-Diéguez et al., 2006; Valderrama et al., 2001).
To shed light on whether NM IIA and NM IIB interfere differently with Golgi apparatus positioning, its relative orientation to the main direction of the cell body as well as gelatine nanofibre orientation was analysed. In agreement with the observed higher alignment of actin fibres and the increased elongation of NM IIB KO cells cultured on aGNF, both the alignment with the cell

body and fibre direction was stronger than for NM IIA KO or wt cells. The same reasoning as before can be applied here: the fast and highly dynamic properties of NM IIA translate the geometric cues, potentially relayed to the cell interior by focal adhesion ordering, into anisotropic contractility. This results in high actin ordering and consequently affects the orientation of the Golgi apparatus, effectively aligning it with the provided geometrical cue. Upon knock-out of NM IIA, cells become less susceptible to such cues, resulting in equal fractions of cells with a Golgi apparatus positioning in front of the nucleus on aGNF and rGNF.
Remarkably, NM IIA KO cells exhibit the same Golgi apparatus orientation as wt cells on aGNF despite the overall reduction in actin stress fibres as well as their ordering. While the high contractility and actin fibre ordering of NM IIB KO cells appears to enhance Golgi apparatus alignment, it is not necessary for establishing it. Furthermore, NM IIB KO cells show a less compact Golgi apparatus morphology as indicated by an increase in overall occupied area. Thus, despite in the first instance reducing alignment by dampening the activity of NM IIA, NM IIB appears to influence the Golgi morphology. However, this effect is only visible for aGNF. Cultured on rGNF, both NM IIA KO and NM IIB KO cells exhibit more compact Golgi apparatus distributions than wt cells, linking it to substrate geometry. This difference might be explained by the difference in actin ordering. Cells cultured on rGNF appear less polarised and exhibit a reduced ordering of actin fibres. Upon polarisation, the Golgi apparatus is shifted towards the direction of elongation, resulting in a positioning perpendicular to the actin fibre orientation. The high parallelisation of actin fibres results in an increase in anisotropic intracellular forces, stabilising the orientation of the Golgi apparatus in line with the nanofibre direction. Although high contractility is not necessary for Golgi apparatus positioning, as clear from the alignment present in NM IIA KO cells, it supports stretching of the Golgi apparatus along the fibre direction, enforcing its localisation. This effect is apparent for NM IIB KO cells: the overshooting NM IIA activity, due to the lack of dampening NM IIB, results in a less compact Golgi apparatus morphology elongated along the fibre direction. On the other hand, NM IIA KO cells exhibiting nearly no contractility show a more compact Golgi apparatus morphology and a slight decrease in Golgi apparatus alignment.
Such effects on Golgi morphology were previously observed for treatment of cells with inhibitors of actin and associated regulators. Disruption of actin stress fibre formation and organisation, as well as inhibition of actin regulators such as Arp2/3 or cortactin result in compact Golgi apparatus morphologies (Campellone et al., 2008; Kirkbride et al., 2012; Lázaro-Diéguez et al., 2006). However, inhibition or overexpression of formin-like 1γ (FMNL1γ) leads to dispersion rather than compaction of the Golgi apparatus (Colón-Franco et al., 2011). Further, interaction of actin with the Golgi apparatus was shown to regulate dispersion of Golgi apparatus during colletive migration of epithelial cells (Khuntia et al., 2022). These observations are in agreement with the observed effects of NM IIA KO or NM IIB KO cultured on aGNF, both affecting actin ordering and contractility. Additionally, the significantly reduced area occupied by the Golgi apparatus of NM IIA KO cells compared to wt cells further emphasizes the influence of actin stress fibres on Golgi apparatus morphology.

In conclusion, while the guidance cue of aGNF can compensate for NM IIA-mediated contractility in initiating polarisation, both NM IIA and NM IIB control Golgi apparatus morphology *via* their regulatory role in actin organisation. While NM IIA intensifies Golgi apparatus alignment and elongation, NM IIB counteracts this effect by dampening NM IIA-activity. Thus, the interplay of NM IIA and NM IIB indirectly regulates Golgi apparatus morphology due to its dependency on stress fibre organisation.

5.2.4 The Interplay of NM IIA and NM IIB is Required for Decision Making in 3D Fibre Networks with Opposing Guidance Cues

To determine whether not only cellular morphology but also polarisation is affected differently in 2D and 3D networks, the alignment of the Golgi apparatus with respect to the main cell axis was analysed. Surprisingly, in the 2D scenario previously unaffected NM IIA KO cells as well as NM IIB KO cells reacted with an increased or decreased alignment within parallel and orthogonal networks, respectively, while wt cells remained unaffected. Within parallel collagen fibres, the added third dimension provides more pre-patterned anchoring points for focal adhesions. This in turn enhances elongation of cells, as visible by the increase of aspect ratio compared to 2D observed for all cell lines. Due to these stabilising effects of the thicker 3D parallel fibres, even NM IIA KO cells are now able to align their Golgi apparatus with their cell shape in an actin stress fibre-independent way as established for the 2D case. For both knock-out cell lines, this results in a comparatively increased alignment, either due to the lack of actin stress fibres or the missing dampening effect of NM IIB on NM IIA activity. In contrast to this, the additional perpendicular direction in orthogonal fibre networks adds complementary guidance cues to those present in parallel fibres. Despite the cells still being able to elongate properly, the lack of controlled NM II-mediated contractility leads to a reduced alignment of the Golgi apparatus with the cell body. Interestingly, wt cells align their Golgi apparatus similarly within parallel and orthogonal fibre networks, indicating a role of the interplay of NM IIA and NM IIB in directional decision making. While wt cells are still perfectly capable of deciding between the two spatial directions provided by the orthogonal fibre arrangement, both knock-out lines are unable to do so. As this also affects NM IIB KO cells, which exhibit nearly undisturbed stress fibre formation and high contractility, it appears the interplay of NM IIA and NM IIB in wt cells is necessary to overcome contradictory guidance cues. Such complementary functions of NM IIA and NM IIB were already demonstrated for 3D migration. Here, NM IIB was shown to regulate nuclear translocation in confined spaces, whereas NM IIA provides the necessary forces to propel the cell forward (Thomas et al., 2015). Further, Raab and colleagues studied the influence of NM IIA and NM IIB in 2D and 3D durotaxis of MSCs. They demonstrated an increased sensitivity to relative expressed NM IIB levels, with both knock-down and overexpression of NM IIB resulting in more isotropic NM IIB distribution and reduced durotaxis. While more tolerant to NM IIA expression levels, phosphorylation levels at S1943 proved critical for durotaxis and polarisation of NM IIB, indicating that durotaxis is more dependent on other factors than contractility (Raab et al., 2012). Additionally, cancer cells rely on Rho/ROCK-mediated contractility to reorganise the ECM to provide guidance cues for migration, but this contractility was not required in aligned collagen gels (Provenzano et al., 2008). Together

with the findings on 3D migration, this emphasizes the necessity of proper NM II interplay to navigate 3D environments. While the results presented here do not provide further insight into the underlying mechanism of how exactly NM IIA and NM IIB act together to achieve such control, one might speculate that the inherently polarised distribution of NM II provides the basis for it. In contact guidance, the pre-patterning of focal adhesions can affect actin ordering. Due to the coupling of self-sorting of NM IIA and NM IIB to the retrograde actin flow (Shutova et al., 2017) together with the complementary contributions to contractility (Weißenbruch et al., 2021), both isoforms are necessary to establish anisotropic tension to translate geometric cues into cellular responses to achieve polarisation. While in less complex 2D geometries this contribution is not necessarily required to achieve polarisation, it becomes crucial within more complex 3D environments.

Together, the observed increase in sensitivity for 3D fibre network organisation of both NM IIA KO and NM IIB KO cells opposed to the insensitivity of wt cells implies that both NM II isoforms act in concert to achieve correct localisation of the Golgi apparatus. While it can be compensated by other means in 2D, the complexity of 3D networks requires both isoforms. However, how exactly the interplay of NM II isoforms regulates this process requires further investigation.

5.3 U2OS Cells Do Not Self-Invade into Microchannels with Gradually Increasing Confinement

In vivo cells need to navigate dense 3D environments. This leads to confinement of cells, once they need to pass through tight spaces. In order to do so, various cell types can adapt their migration to an amoeboid mode (Y. J. Liu et al., 2015). In the last part of this thesis, an experimental setup for the analysis of cells undergoing MAT was presented. It comprises an Insall-chamber which was modified with gradually confining microchannels (Muinonen-Martin et al., 2010). The channel widths were chosen to match degrees of confinement previously shown to induce amoeboid migration (Holle et al., 2019; Y. J. Liu et al., 2015). In these previously used settings, confinement was applied rather abruptly, hindering the analysis of the transition between migration modes. In the setup presented here, the addition of gradually confining regions, termed transition zones, adds the possibility to monitor the previously inaccessible transition process.
Although Holle and colleagues observed a self-invasion of cancer cells into their confining microchannels (Holle et al., 2019), the U2OS cells used in this work did not display such behaviour. Thus, this far the transition from mesenchymal to amoeboid migration could not be analysed. To nonetheless facilitate migration into the confining regions of the microchannels, the underlying Insall-chamber allows application of chemotactic gradients as confirmed by imaging fluorescein distribution over time. After an initial high slope of the gradient, it was reduced over time and remained stable after 18 h. This decrease in gradient strength is probably due to the initially high concentration difference, as only one reservoir contains fluorescein. Over time, this difference becomes lesser due to the continuous diffusion of fluorescein along this gradient, resulting in gradual increase of concentration in the other reservoir and stabilisation of the gradient.
Next, monocyte chemoattractant protein-1 (MCP-1) and stromal cell-derived factor 1 (SDF-1) were identified as suitable chemoattractors for U2OS cells (Dillenburg-Pilla et al., 2015; B. Li et al., 2018; J. F. Liu et al., 2020). As the difference in fluorescein intensity was roughly doubled at the beginning of the gradient compared to the end, double the concentration of MCP-1 or SDF-1 shown to be chemotactic was added to the outer reservoir of the chamber. However, neither condition proved sufficient to induce directional migration. This might be explained by the different size of fluorescein and the chemoattractants. While the latter possess molecular masses above 8 kDa, fluorescein is a comparatively small molecule with only 332 Da. As such, fluorescein diffuses faster than MCP-1 and SDF-1, resulting in different gradient formation of the latter two. Thus, the chosen concentrations might be too low to establish a chemotactic gradient or may have needed more time to form a stable one. Unfortunately, due to time restrictions, further testing of conditions could not be performed in the course of this thesis.

Chapter 6

Conclusion and Outlook

The work presented here aimed at elucidating how different aspects of the cellular microenvironment affect cellular behaviour and how especially NM II is involved in the adaptation process. These aspects, namely the influence of material parameters on the mechanoresponse as well as the role of NM II in sensing and adapting to substrate geometry and confinement were analysed by three different approaches. The individual approaches together with the obtained findings and insights as well as future perspectives are given in the following.

Soft Elastic Metamaterials Allow for Mechanoregulation of Cells

First, a metamaterial-based workflow centered around soft and deformable metamaterials was developed in collaboration with Dr. Yi Chen (Wegener group, Institute for Applied Physics, KIT, Karlsruhe), which allows spatial and temporal analysis of cellular forces in unprecedented detail. The analysis includes determining cell-induced displacements of metamaterials during LCI and their conversion into force fields *via* FEM under consideration of material properties. In collaboration with Natalie Munding (Tanaka group, Institute of Physical Chemistry, Heidelberg University, Heidelberg), hMSCs were subjected to this workflow, providing a proof-of-concept of mechanoregulation of cells by effective material properties (Munding et al., 2023). To the best of my knowledge, this collaborative effort provided the currently most detailed analysis of the influence of metamaterial properties on the cellular mechanoresponse, going beyond previously published morphological descriptions.
In the course of this work, said workflow was applied to analyse REF cells and their respective mechanoresponse. In contrast to hMSCs, these cells remain unaffected by effective metamaterial properties. While the main observable difference appears to be the capability to deform the metamaterials to a larger degree, it is not clear whether this insensibility is due to a difference in contractile forces or another cell type-specific effect. To test these hypotheses, other cell lines should be subjected to the metamaterial geometries used here and their response evaluated. Additionally, other material properties as well as isotropic and anisotropic distributions of those could be analysed to determine which factors influence the cellular mechanoresponse.
Furthermore, the direct comparison of REF cells cultured on soft and stiff metamaterials revealed that REF cells sense the induced micropatterning in a stiffness-dependent manner rather than the effective metamaterial properties. Although the effect of micropatterns on mechanosensing was demonstrated previously (Kassianidou et al., 2019; Lehnert et al., 2004), further experimental evi-

dence is needed to understand in detail how exactly this stiffness-dependent geometry sensing is achieved. For this, soft and stiff micropatterns with varying adhesion angles and distance could be fabricated by 3D laser microprinting. The direct comparison of focal adhesion geometry with respect to material stiffness would provide a comprehensive approach from which this potential mechanism could be elucidated.

NM IIA and NM IIB Contribute to Contact Guidance Based on Their Respective Dynamic Properties and Role in Actin Ordering

In the second part of this thesis, differently oriented nanofibre substrates were employed to analyse the ambiguously reported role of NM II in contact guidance in 2D and 3D. By using knock-out cell lines of either NM IIA or NM IIB, an altered morphological adaptation and polarisation within fibrous networks was characterised. The observed altered cell spreading, elongation and polarisation can be attributed to the different dynamics of both isoforms and their specific contributions to actin ordering and contractiliy. According to its fast turnover and initiation of minifilament formation, NM IIA facilitates highly parallel actin fibres in aligned fibre networks, whereas NM IIB counteracts this by dampening NM IIA activity and stabilising actin stress fibres. Although Golgi apparatus positioning could still be achieved in absence of NM IIA or NM IIB, it appeared more dispersed for NM IIA KO. As the knock-out of NM IIA results in a drastic reduction of actin stress fibres and contractility, this confirms previous reports of a regulatory role of actin on Golgi apparatus morphology. Furthermore, the increased responsiveness of either knock-out cell line to 3D fibre network organisation compared to wt cells, implies a previously unidentified role of the interplay of NM IIA and NM IIB on polarisation decision making in 3D.
To further determine this regulatory role, the alignment analysis conducted in this work should be complemented by an analysis of actin ordering and Golgi apparatus alignment with fibres as performed for the 2D case, as well as one of focal adhesion distribution and size. This would allow determining the effect of the 3D environment on adhesion formation and actin ordering. Thus, this might further help to distinguish between the effects of actin and NM II-mediated contractility. Furthermore, analysis of cell migration might provide further insights how NM IIA and NM IIB modulate navigation in complex 3D environments.

Development of a Modified Insall-Chamber for Analysis of MAT

The last part of this thesis focussed on providing an experimental setup for imaging cells during MAT. For this, chemotaxis chambers based on the Insall-chamber (Muinonen-Martin et al., 2010) were fabricated and combined with gradually confining microchannels. The chambers were tested for optical properties and the formation of gradients, both proofing sufficient for experimental use. Unfortunately, due to time restrictions, thus far no suitable condition for facilitating directional migration into the microchannels by chemotaxis was found.
Once such a condition is determined, knock-out cell lines for NM IIA and NM IIB can be subjected to the microchannels. While both isoforms were shown to play a role in facilitating migration through dense 3D networks, their role in transitioning to amoeboid movement remains unknown

(Dey et al., 2017; Ghosh et al., 2021; Taneja & Burnette, 2019). By visualisation of the gradual transition process by LCI of knock-out cells migrating in the confining microchannels, conclusions on the individual isoforms' role could be obtained. This analysis could also be extended to other intracellular factors associated with MAT such as actin, if respective reporter cell lines or transfection constructs are available.

In conclusion, within this thesis three approaches were presented to study the effect of the cellular microenvironment on the cellular mechanoresponse. This includes an unprecedented analysis of the influence of effective material properties on the cellular mechanoresponse based on metamaterials. Further, the interplay of NM IIA and NM IIB was characterised as crucial for determining polarisation directions in 3D and a new experimental setup was developed for analysis of migration under increasing confinement. Together, the results presented here provide new perspectives and opportunities for further mechanobiological studies aiming at disentangling the effect of the microenvironment on cellular behaviour.

Chapter A

Appendix

A.1 Supplementary Data

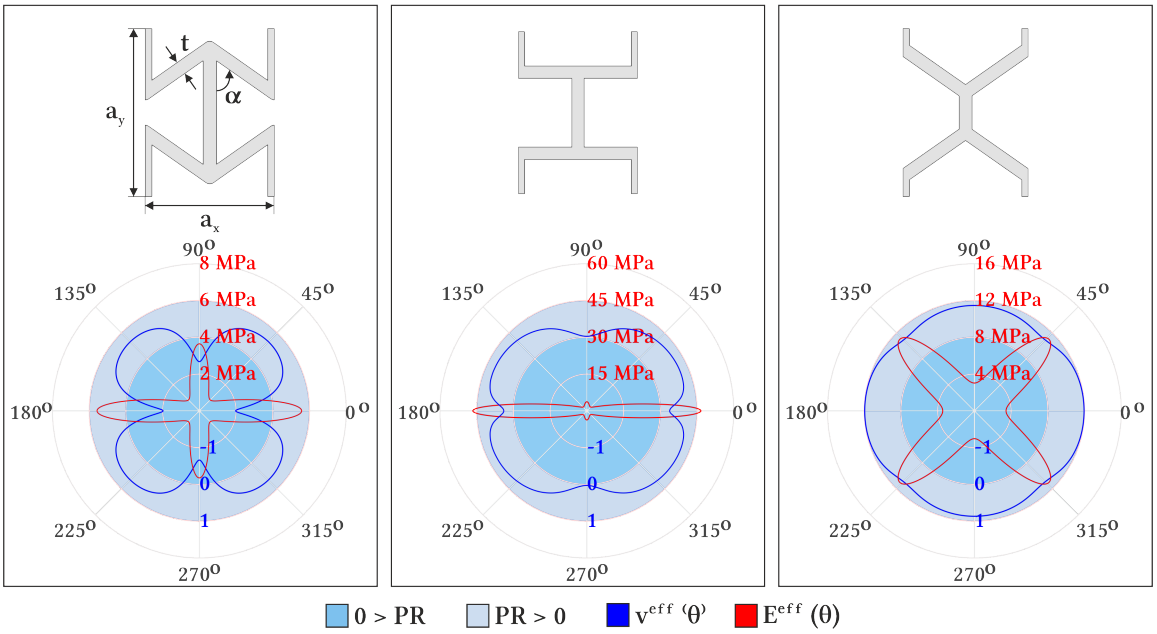

Figure S1: Physical characterisation of stiff metamaterial geometries.
Calculated Young's moduli (red) and Poisson's ratios (blue) of metamaterials fabricated from PETA in dependency of the angle in which the force is applied. The distribution of Poisson's ratios and Young's moduli resemble those of soft metamaterials. Whereas soft metamaterials do not exhibit Young's moduli above 170 kPa, the repective values for the Young's modulus of PETA geometries range from 800 kPa to 45 MPa. This renders the individual geometries above 200 times stiffer than their soft pendant. Poisson-negative and -positive regions are coloured in light blue and medium blue, respectively. Calculations were provided by Yi Chen (Wegener group, Institute of Applied Physics, KIT, Karlsruhe).

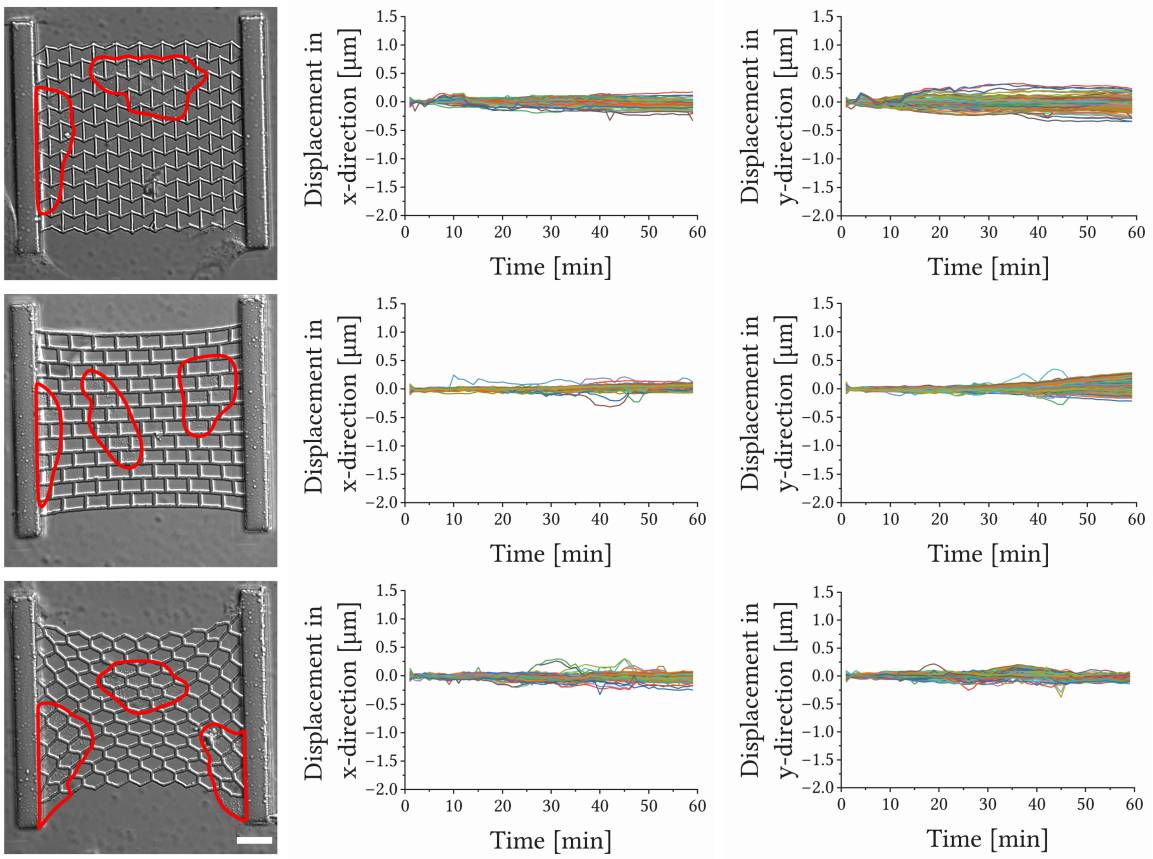

Figure S2: Deformation of stiff PETA metamaterial geometries.
DIC images of REF cells cultured on stiff metamaterial geometries acquired during LCI are given on the left. The outline of each cell was manually traced (red line). The corresponding extracted displacements in x- and y-direction over time with respect to the initial marker position are given next to each image. For all geometries, a neglectible deformation below 0.25 µm is present. As these deformations remain constant over time, they are likely due to alignment errors of the timelapse image series. Thus, stiff geometries can be considered non-deformable by REF cells. Scale bar: 20 µm.

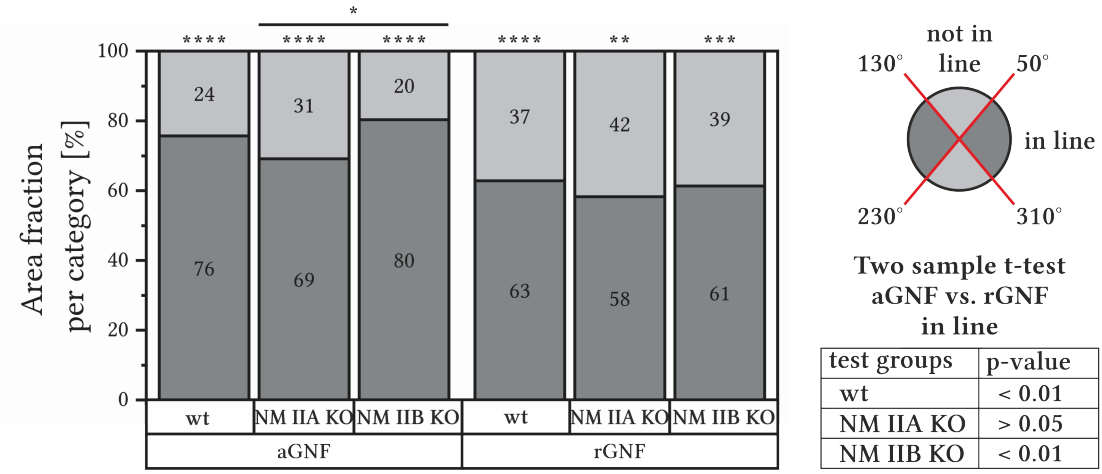

Two sample t-test aGNF vs. rGNF in line

test groups	p-value
wt	< 0.01
NM IIA KO	> 0.05
NM IIB KO	< 0.01

Figure S3: Percentile fractions of Golgi apparatus area in line with fibre direction.
The radial distribution of the Golgi apparatus area was divided into the categories 'in line' (dark grey) and 'not in line' (light grey) as depicted on the top right. For all cells, significantly more Golgi apparatus area is categorised as 'in line'. Both wt and NM IIB KO cells are significantly more polarised on aGNF than on rGNF (right table). When comparing the cell lines with each other on each substrate, merely the Golgi apparatus area of NM IIB KO cells appears significantly more 'in line' than for NM IIA KO cells. N≥3, n≥27.

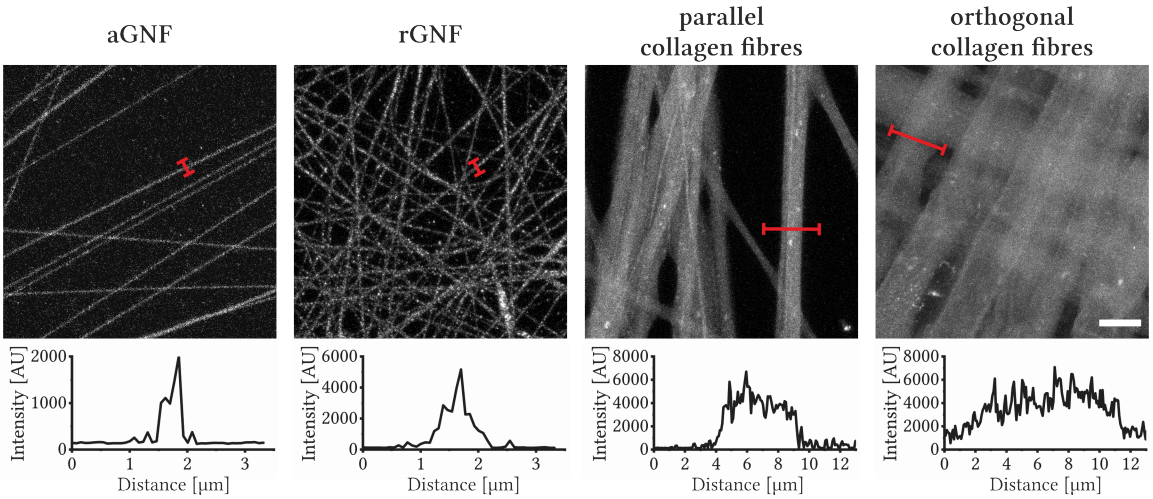

Figure S4: Thickness of different nanofibres.
Flourescence microscopy images of gelatine nanofibres and collagen networks. The fluorescence profile of the area indicated in red is given below each image. From this, a fibre thickness of 0.6-1 µm and 6-10 µm can be estimated for gelatine nanofibres and collagen networks, respectively. Thus, gelatine nanofibres are at least 6 times thinner than collagen fibres. Scale bar: 10 µm.

A.2 Abbreviations

1PA	one-photon absorption
2PA	two-photon absorption
ACD	assembly competent domain
ADP	adenosine diphosphate
aGNF	aligned gelatine nanofibres
Arp	actin-related protein
ATP	adenosine triphosphate
BSA	bovine serum albumin
CKII	casein kinase II
DIC	differential interference contrast
DMSO	dimethyl sulfoxide
ECM	extracellular matrix
ELC	essential light chain
FAK	focal adhesion kinase
FBS	fetal bovine serum
FEM	finite element method
FERM	protein 4.1, ezrin, radixin and moesin
FMNL1γ	formin-like 1γ
FRAP	fluorescence recovery after photobleaching
GPCR	G-protein coupled receptor
HC	heavy chain
hMSC	human mesenchymal stem cell
KO	knock-out
LATS	large tumor suppressor
LCI	live cell imaging
LINC	linker of nucleoskeleton and cytoskeleton
MAPK	mitogen-activated protein kinase
MAT	mesenchymal-to-amoeboid transition
MCP-1	monocyte chemoattractant protein-1
MLCK	myosin light chain kinase
MLCP	myosin light chain phosphatase

MSC	mesenchymal stem cell
MST	mammalian Ste20-like kinase
MTOC	microtubule organising centre
NHT	non-helical tailpiece
NM II	non-muscle myosin II
NM IIA	non-muscle myosin IIA
NM IIB	non-muscle myosin IIB
NM IIC	non-muscle myosin IIC
PBS	phosphate buffered saline
PBS-T	PBS containing 0.1% Triton-X100
PEGDA	polyethylene glycol diacrylate
PETA	pentaerythritol triacrylate
PFA	*para*-formaldehyde
PGMEA	propylene glycol methyl ether acetate
PKC	protein kinase C
REF	rat embryonic fibroblast
rGNF	random gelatine nanofibres
RLC	regulatory light chain
ROCK	Rho-associated coil kinase
SDF-1	stromal cell-derived factor 1
TAZ	transcriptional co-activator with PDZ-binding motif
TEAD	transcriptional enhanced associated domain
TPETA	trimethylolpropane ethoxylate triacrylate
wt	wildtype
YAP	Yes-associated protein

A.3 List of Figures

A.4 List of Tables

Bibliography

Abbe, E. (1873). Beiträge zur Theorie des Mikroskops und der mikroskopischen Wahrnehmung: I. Die Construction von Mikroskopen auf Grund der Theorie. *Archiv für mikroskopische Anatomie*, *9*, 413–418. https://doi.org/10.1007/BF02956173

Amano, M., Ito, M., Kimura, K., Fukata, Y., Chihara, K., Nakano, T., Matsuura, Y., & Kaibuchi, K. (1996). Phosphorylation and activation of myosin by Rho-associated kinase (Rho- kinase). *Journal of Biological Chemistry*, *271*(34), 20246–20249. https://doi.org/10.1074/jbc.271.34.20246

Bachmann, M., Schäfer, M., Mykuliak, V. V., Ripamonti, M., Heiser, L., Weisenßruch, K., Krübel, S., Franz, C. M., Hytönen, V. P., Wehrle-Haller, B., & Bastmeyer, M. (2020). Induction of ligand promiscuity of αVβ3 integrin by mechanical force. *Journal of Cell Science*, *133*(9), jcs242404. https://doi.org/10.1242/jcs.242404

Bagheri, A., & Jin, J. (2019). Photopolymerization in 3D Printing. *ACS Applied Polymer Materials*, *1*(4), 593–611. https://doi.org/10.1021/acsapm.8b00165

Baldacchini, T. (2015). *Three-Dimensional Microfabrication Using Two-Photon Polymerization*. William Andrew.

Bangasser, B. L., Shamsan, G. A., Chan, C. E., Opoku, K. N., Tüzel, E., Schlichtmann, B. W., Kasim, J. A., Fuller, B. J., McCullough, B. R., Rosenfeld, S. S., & Odde, D. J. (2017). Shifting the optimal stiffness for cell migration. *Nature Communications*, *8*, 15313. https://doi.org/10.1038/ncomms15313

Barner-Kowollik, C., Bastmeyer, M., Blasco, E., Delaittre, G., Müller, P., Richter, B., & Wegener, M. (2017). 3D Laser Micro- and Nanoprinting: Challenges for Chemistry. *Angewandte Chemie International Edition*, *56*(50), 15828–15845. https://doi.org/10.1002/ANIE.201704695

Beach, J. R., Shao, L., Remmert, K., Li, D., Betzig, E., & Hammer, J. A. (2014). Nonmuscle myosin II isoforms coassemble in living cells. *Current Biology*, *24*(10), 1160–1166. https://doi.org/10.1016/j.cub.2014.03.071

Belay, B., Mäntylä, E., Maibohm, C., Silvestre, O. F., Hyttinen, J., Nieder, J. B., & Ihalainen, T. O. (2023). Substrate microtopographies induce cellular alignment and affect nuclear force transduction. *Journal of the Mechanical Behavior of Biomedical Materials*, *146*, 106069. https://doi.org/10.1016/J.JMBBM.2023.106069

Billington, N., Wang, A., Mao, J., Adelstein, R. S., & Sellers, J. R. (2013). Characterization of three full-length human nonmuscle myosin II paralogs. *Journal of Biological Chemistry*, *288*(46), 33398–33410. https://doi.org/10.1074/jbc.M113.499848

Breckenridge, M. T., Dulyaninova, N. G., & Egelhoff, T. T. (2009). Multiple regulatory steps control mammalian nonmuscle myosin II assembly in live cells. *Molecular Biology of the Cell*, *20*(1), 338–347. https://doi.org/10.1091/mbc.E08-04-0372

Cai, Y., Rossier, O., Gauthier, N. C., Biais, N., Fardin, M. A., Zhang, X., Miller, L. W., Ladoux, B., Cornish, V. W., & Sheetz, M. P. (2010). Cytoskeletal coherence requires myosin-IIA contractility. *Journal of Cell Science*, *123*(3), 413–423. https://doi.org/10.1242/jcs.058297

Califano, J. P., & Reinhart-King, C. A. (2010). Substrate stiffness and cell area predict cellular traction stresses in single cells and cells in contact. *Cellular and Molecular Bioengineering*, *3*, 68–75. https://doi.org/10.1007/s12195-010-0102-6

Callens, S. J., Uyttendaele, R. J., Fratila-Apachitei, L. E., & Zadpoor, A. A. (2020). Substrate curvature as a cue to guide spatiotemporal cell and tissue organization. *Biomaterials*, *232*, 119739. https://doi.org/10.1016/j.biomaterials.2019.119739

Campellone, K. G., Webb, N. J., Znameroski, E. A., & Welch, M. D. (2008). WHAMM Is an Arp2/3 Complex Activator That Binds Microtubules and Functions in ER to Golgi Transport. *Cell*, *134*, 148–161. https://doi.org/10.1016/j.cell.2008.05.032

Carisey, A., & Ballestrem, C. (2011). Vinculin, an adapter protein in control of cell adhesion signalling. *European Journal of Cell Biology*, *90*, 157–163. https://doi.org/10.1016/J.EJCB.2010.06.007

Casingal, C. R., Descant, K. D., & Anton, E. S. (2022). Coordinating cerebral cortical construction and connectivity: Unifying influence of radial progenitors. *Neuron*, *110*(7), 1100–1115. https://doi.org/10.1016/j.neuron.2022.01.034

Chan, C. E., & Odde, D. J. (2008). Traction dynamics of filopodia on compliant substrates. *Science*, *322*(5908), 1687–1691. https://doi.org/10.1126/science.1163595

Chen, B., Kumar, G., Co, C. C., & Ho, C. C. (2013). Geometric Control of Cell Migration. *Scientific Reports*, *3*, 2827. https://doi.org/10.1038/srep02827

Colón-Franco, J. M., Gomez, T. S., & Billadeau, D. D. (2011). Dynamic remodeling of the actin cytoskeleton by FMNL1γ is required for structural maintenance of the Golgi complex. *Journal of Cell Science*, *124*(18), 3118–3126. https://doi.org/10.1242/JCS.083725

Conti, M. A., & Adelstein, R. S. (2008). Nonmuscle myosin II moves in new directions. *Journal of Cell Science*, *121*(1), 11–18. https://doi.org/10.1242/jcs.007112

Coyle, S., Doss, B., Huo, Y., Singh, H. R., Quinn, D., Jimmy Hsia, K., & LeDuc, P. R. (2022). Cell alignment modulated by surface nano-topography – Roles of cell-matrix and cell-cell interactions. *Acta Biomaterialia*, *142*, 149–159. https://doi.org/10.1016/J.ACTBIO.2022.01.057

Curtis, A., & Clark, P. (1990). The Effects of Topographic and Mechanical-Properties of Materials on Cell Behavior. *Critical Reviews in Biocompatibility*, *5*(4), 343–362.

Curtis, A., & Wilkinson, C. (1997). Topographical control of cells. *18*, 1573–1583.

Dasgupta, I., & McCollum, D. (2019). Control of cellular responses to mechanical cues through YAP/TAZ regulation. *Journal of Biological Chemistry*, *294*(46), 17693–17706. https://doi.org/10.1074/JBC.REV119.007963

De Bellis, I., Nocentini, S., Giulia, M., Santi, D., Martella, D., Parmeggiani, C., Zanotto, S., & Wiersma, D. S. (2021). Two-Photon Laser Writing of Soft Responsive Polymers via Temperature-Controlled Polymerization. *Laser & Photonics Reviews*, *15*(8), 2100090. https://doi.org/10.1002/LPOR.202100090

Decker, C., & Jenkins, A. D. (1985). Kinetic Approach of Oxygen Inhibition in Ultraviolet and Laser-Induced Polymerizations. *Macromolecules*, *18*(6), 1241–1244. https://doi.org/10.1021/ma00148a034

Desroches, S., & Harris, A. R. (2023). Quantifying cytoskeletal organization from optical microscopy data. *Frontiers in Cell and Developmental Biology*, *11*, 1327994. https://doi.org/10.3389/fcell.2023.1327994

de Visser, K. E., & Joyce, J. A. (2023). The evolving tumor microenvironment: From cancer initiation to metastatic outgrowth. *Cancer Cell*, *41*(3), 374–403. https://doi.org/10.1016/j.ccell.2023.02.016

Dey, S. K., Singh, R. K., Chattoraj, S., Saha, S., Das, A., Bhattacharyya, K., Sengupta, K., Sen, S., & Jana, S. S. (2017). Differential role of nonmuscle myosin II isoforms during blebbing of MCF-7 cells. *Molecular Biology of the Cell*, *28*(8), 1034–1042. https://doi.org/10.1091/mbc.e16-07-0524

Di Campli, A., Valderrama, F., Babià, T., De Matteis, M. A., Luini, A., & Egea, G. (1999). Morphological Changes in the Golgi Complex Correlate With Actin Cytoskeleton Rearrangements. *Cell Motility and the Cytoskeleton*, *43*, 334–348. https://doi.org/10.1002/(SICI)1097-0169(1999)43:4<334::AID-CM6>3.0.CO;2-3

Dillenburg-Pilla, P., Patel, V., Mikelis, C. M., Zárate-Bladés, C. R., Doçi, C. L., Amornphimoltham, P., Wang, Z., Martin, D., Leelahavanichkul, K., Dorsam, R. T., Masedunskas, A., Weigert, R., Molinolo, A. A., & Gutkind, J. S. (2015). SDF-1/CXCL12 induces directional cell migration and spontaneous metastasis via a CXCR4/Gαi/mTORC1 axis. *The FASEB Journal*, *29*(3), 1056–1068. https://doi.org/10.1096/FJ.14-260083

Diller, R. B., & Tabor, A. J. (2022). The Role of the Extracellular Matrix (ECM) in Wound Healing: A Review. *Biomimetics*, *7*(3), 87. https://doi.org/10.3390/BIOMIMETICS7030087

Discher, D. E., Janmey, P., & Wang, Y. L. (2005). Tissue cells feel and respond to the stiffness of their substrate. *Science*, *310*(5751), 1139–1143. https://doi.org/10.1126/science.1116995

Dominguez, R., & Holmes, K. C. (2011). Actin Structure and Function. *Annual Review of Biophysics*, *40*(1), 169–186. https://doi.org/10.1146/annurev-biophys-042910-155359

Dong, Z., Ren, X., Jia, B., Zhang, X., Wan, X., Wu, Y., & Huang, H. (2024). Composite patch with negative Poisson's ratio mimicking cardiac mechanical properties: Design, experiment and simulation. *Materials Today Bio*, *26*, 101098. https://doi.org/10.1016/J.MTBIO.2024.101098

Doss, B. L., Pan, M., Gupta, M., Grenci, G., Mège, R. M., Lim, C. T., Sheetz, M. P., Voituriez, R., & Ladoux, B. (2020). Cell response to substrate rigidity is regulated by active and passive cytoskeletal stress. *Proceedings of the National Academy of Sciences of the United States of America*, *117*(23), 12817–12825. https://doi.org/10.1073/pnas.1917555117

Dulyaninova, N. G., & Bresnick, A. R. (2013). The heavy chain has its day. *BioArchitecture*, *3*(4), 77–85. https://doi.org/10.4161/BIOA.26133

Dupont, S., Morsut, L., Aragona, M., Enzo, E., Giulitti, S., Cordenonsi, M., Zanconato, F., Le Digabel, J., Forcato, M., Bicciato, S., Elvassore, N., & Piccolo, S. (2011). Role of YAP/TAZ in mechanotransduction. *Nature*, *474*, 179–183. https://doi.org/10.1038/nature10137

Durán, J. M., Valderrama, F., Castel, S., Magdalena, J., Tomás, M., Hosoya, H., Renau-Piqueras, J., Malhotra, V., & Egea, G. (2003). Myosin motors and not actin comets are mediators of the

actin-based Golgi-to-endoplasmic reticulum protein transport. *Molecular Biology of the Cell*, *14*(2), 445–459. https://doi.org/10.1091/mbc.e02-04-0214

Edwards, M., Zwolak, A., Schafer, D. A., Sept, D., Dominguez, R., & Cooper, J. A. (2014). Capping protein regulators fine-tune actin assembly dynamics. *Nature Reviews Molecular Cell Biology*, *15*, 677–689. https://doi.org/10.1038/nrm3869

Egea, G., Serra-Peinado, C., Salcedo-Sicilia, L., & Gutiérrez-Martínez, E. (2013). Actin acting at the Golgi. *Histochemistry and Cell Biology 2013*, *140*, 347–360. https://doi.org/10.1007/S00418-013-1115-8

Elosegui-Artola, A., Oria, R., Chen, Y., Kosmalska, A., Pérez-González, C., Castro, N., Zhu, C., Trepat, X., & Roca-Cusachs, P. (2016). Mechanical regulation of a molecular clutch defines force transmission and transduction in response to matrix rigidity. *Nature Cell Biology*, *18*, 540–548. https://doi.org/10.1038/ncb3336

Elosegui-Artola, A., Andreu, I., Beedle, A. E., Lezamiz, A., Uroz, M., Kosmalska, A. J., Oria, R., Kechagia, J. Z., Rico-Lastres, P., Le Roux, A. L., Shanahan, C. M., Trepat, X., Navajas, D., Garcia-Manyes, S., & Roca-Cusachs, P. (2017). Force Triggers YAP Nuclear Entry by Regulating Transport across Nuclear Pores. *Cell*, *171*(6), 1397–1410.e14. https://doi.org/10.1016/J.CELL.2017.10.008

Elosegui-Artola, A., Trepat, X., & Roca-Cusachs, P. (2018). Control of Mechanotransduction by Molecular Clutch Dynamics. *Trends in Cell Biology*, *28*(5), 356–367. https://doi.org/10.1016/j.tcb.2018.01.008

Engler, A. J., Sen, S., Sweeney, H. L., & Discher, D. E. (2006). Matrix Elasticity Directs Stem Cell Lineage Specification. *Cell*, *126*, 677–689. https://doi.org/10.1016/j.cell.2006.06.044

Even-Faitelson, L., & Ravid, S. (2006). PAK1 and aPKCζ regulate myosin II-B phosphorylation: A novel signaling pathway regulating filament assembly. *Molecular Biology of the Cell*, *17*(7), 2869–2881. https://doi.org/10.1091/mbc.e05-11-1001

Faurobert, E., Bouin, A. P., & Albiges-Rizo, C. (2015). Microenvironment, tumor cell plasticity, and cancer. *Current Opinion in Oncology*, *27*(1), 64–70. https://doi.org/10.1097/CCO.0000000000000154

Fee, T., Surianarayanan, S., Downs, C., Zhou, Y., & Berry, J. (2016). Nanofiber Alignment Regulates NIH3T3 Cell Orientation and Cytoskeletal Gene Expression on Electrospun PCL+Gelatin Nanofibers. *PLOS ONE*, *11*(5), e0154806. https://doi.org/10.1371/journal.pone.0154806

Fischer, J., & Wegener, M. (2013). Three-dimensional optical laser lithography beyond the diffraction limit. *Laser & Photonics Reviews*, *7*(1), 22–44. https://doi.org/10.1002/LPOR.201100046

Flamourakis, G., Spanos, I., Vangelatos, Z., Manganas, P., Papadimitriou, L., Grigoropoulos, C., Ranella, A., Farsari, M., Flamourakis, G., Spanos, I., Manganas, P., Papadimitriou, L., Ranella, A., Farsari, M., Vangelatos, Z., & Grigoropoulos, C. (2020). Laser-made 3D Auxetic Metamaterial Scaffolds for Tissue Engineering Applications. *Macromolecular Materials and Engineering*, *305*(7), 2000238. https://doi.org/10.1002/MAME.202000238

Flemming, R. G., Murphy, C. J., Abrams, G. A., Goodman, S. L., & Nealey, P. F. (1999). Effects of synthetic micro- and nano-structured surfaces on cell behavior. *Biomaterials*, *20*(6), 573–588. https://doi.org/10.1016/S0142-9612(98)00209-9

Fortunato, I. C., & Sunyer, R. (2022). The Forces behind Directed Cell Migration. *Biophysica*, *2*(4), 548–563. https://doi.org/10.3390/BIOPHYSICA2040046

Frenzel, T., Köpfler, J., Naber, A., & Wegener, M. (2021). Atomic scale displacements detected by optical image cross-correlation analysis and 3D printed marker arrays. *Scientific Reports*, *11*, 2304. https://doi.org/10.1038/s41598-021-81712-8

Fu, M., Hu, Y., Lan, T., Guan, K. L., Luo, T., & Luo, M. (2022). The Hippo signalling pathway and its implications in human health and diseases. *Signal Transduction and Targeted Therapy*, *7*, 376. https://doi.org/10.1038/s41392-022-01191-9

Gatt, R., Vella Wood, M., Gatt, A., Zarb, F., Formosa, C., Azzopardi, K. M., Casha, A., Agius, T. P., Schembri-Wismayer, P., Attard, L., Chockalingam, N., & Grima, J. N. (2015). Negative Poisson's ratios in tendons: An unexpected mechanical response. *Acta Biomaterialia*, *24*, 201–208. https://doi.org/10.1016/J.ACTBIO.2015.06.018

Ghibaudo, M., Saez, A., Trichet, L., Xayaphoummine, A., Browaeys, J., Silberzan, P., Buguin, A., & Ladoux, B. (2008). Traction forces and rigidity sensing regulate cell functions. *Soft Matter*, *4*, 1836–1843. https://doi.org/10.1039/B804103B

Ghosh, I., Singh, R. K., Mishra, M., Kapoor, S., & Jana, S. S. (2021). Switching between blebbing and lamellipodia depends on the degree of non-muscle myosin II activity. *Journal of Cell Science*, *134*(1), jcs248732. https://doi.org/10.1242/jcs.248732

Giuseppe, M. D., Law, N., Webb, B., A. Macrae, R., Liew, L. J., Sercombe, T. B., Dilley, R. J., & Doyle, B. J. (2018). Mechanical behaviour of alginate-gelatin hydrogels for 3D bioprinting. *Journal of the Mechanical Behavior of Biomedical Materials*, *79*, 150–157. https://doi.org/10.1016/J.JMBBM.2017.12.018

Golomb, E., Ma, X., Jana, S. S., Preston, Y. A., Kawamoto, S., Shoham, N. G., Goldin, E., Conti, M. A., Sellers, J. R., & Adelstein, R. S. (2004). Identification and Characterization of Nonmuscle Myosin II-C, a New Member of the Myosin II Family. *Journal of Biological Chemistry*, *279*(4), 2800–2808. https://doi.org/10.1074/JBC.M309981200

Gupton, S. L., & Waterman-Storer, C. M. (2006). Spatiotemporal Feedback between Actomyosin and Focal-Adhesion Systems Optimizes Rapid Cell Migration. *Cell*, *125*(7), 1361–1374. https://doi.org/10.1016/J.CELL.2006.05.029

Gurel, P. S., Hatch, A. L., & Higgs, H. N. (2014). Connecting the cytoskeleton to the endoplasmic reticulum and Golgi. *Current Biology*, *24*(14), R660–R672. https://doi.org/10.1016/j.cub.2014.05.033

Hahn, V., Messer, T., Bojanowski, N. M., Curticean, E. R., Wacker, I., Schröder, R. R., Blasco, E., & Wegener, M. (2021). Two-step absorption instead of two-photon absorption in 3D nanoprinting. *Nature Photonics 2021*, *15*(12), 932–938. https://doi.org/10.1038/s41566-021-00906-8

Hakeem, R. M., Subramanian, B. C., Hockenberry, M. A., King, Z. T., Butler, M. T., Legant, W. R., & Bear, J. E. (2023). A Photopolymerized Hydrogel System with Dual Stiffness Gradients Reveals Distinct Actomyosin-Based Mechano-Responses in Fibroblast Durotaxis. *ACS Nano*, *17*(1), 197–211. https://doi.org/10.1021/acsnano.2c05941

Handrea-Dragan, I. M., Botiz, I., Tatar, A. S., & Boca, S. (2022). Patterning at the micro/nano-scale: Polymeric scaffolds for medical diagnostic and cell-surface interaction applications. *Col-*

loids and Surfaces B: Biointerfaces, *218*, 112730. https://doi.org/10.1016/j.colsurfb.2022.112730

Harrison, R. G. (1912). The cultivation of tissues in extraneous media as a method of morphogenetic study. *The Anatomical Record*, *6*(4), 181–193. https://doi.org/10.1002/ar.1090060404

Heissler, S. M., & Sellers, J. R. (2016). Various Themes of Myosin Regulation. *Journal of Molecular Biology*, *428*(9), 1927–1946. https://doi.org/10.1016/j.jmb.2016.01.022

Hippler, M., Weißenbruch, K., Richler, K., Lemma, E. D., Nakahata, M., Richter, B., Barner-Kowollik, C., Takashima, Y., Harada, A., Blasco, E., Wegener, M., Tanaka, M., & Bastmeyer, M. (2020). Mechanical stimulation of single cells by reversible host-guest interactions in 3D microscaffolds. *Science Advances*, *6*(39), eabc2648. https://doi.org/10.1126/sciadv.abc2648

Holle, A. W., Govindan Kutty Devi, N., Clar, K., Fan, A., Saif, T., Kemkemer, R., & Spatz, J. P. (2019). Cancer Cells Invade Confined Microchannels via a Self-Directed Mesenchymal-to-Amoeboid Transition. *Nano Letters*, *19*(4), 2280–2290. https://doi.org/10.1021/acs.nanolett.8b04720

Hotulainen, P., & Lappalainen, P. (2006). Stress fibers are generated by two distinct actin assembly mechanisms in motile cells. *Journal of Cell Biology*, *173*(3), 383–394. https://doi.org/10.1083/jcb.200511093

Huang, Y., Su, J., Liu, J., Yi, X., Zhou, F., Zhang, J., Wang, J., Meng, X., Si, L., & Wu, C. (2022). YAP Activation in Promoting Negative Durotaxis and Acral Melanoma Progression. *Cells*, *11*(22), 3543. https://doi.org/10.3390/cells11223543

Humphries, J. D., Wang, P., Streuli, C., Geiger, B., Humphries, M. J., & Ballestrem, C. (2007). Vinculin controls focal adhesion formation by direct interactions with talin and actin. *Journal of Cell Biology*, *179*(5), 1043–1057. https://doi.org/10.1083/jcb.200703036

Hwang, W., & Lang, M. J. (2009). Mechanical Design of Translocating Motor Proteins. *Cell biochemistry and biophysics*, *54*, 11–22. https://doi.org/10.1007/S12013-009-9049-4

Hytönen, V. P., & Wehrle-Haller, B. (2016). Mechanosensing in cell–matrix adhesions – Converting tension into chemical signals. *Experimental Cell Research*, *343*, 35–41. https://doi.org/10.1016/J.YEXCR.2015.10.027

Ikebe, M., & Hartshorne, D. J. (1985). Phosphorylation of smooth muscle myosin at two distinct sites by myosin light chain kinase. *Journal of Biological Chemistry*, *260*(18), 10027–10031. https://doi.org/10.1016/s0021-9258(17)39206-2

Ikebe, M., Koretz, J., & Hartshorne, D. J. (1988). Effects of phosphorylation of light chain residues threonine 18 and serine 19 on the properties and conformation of smooth muscle myosin. *Journal of Biological Chemistry*, *263*(13), 6432–6437. https://doi.org/10.1016/s0021-9258(18)68804-0

Inoue, S., Frank, V., Hörning, M., Kaufmann, S., Yoshikawa, H. Y., Madsen, J. P., Lewis, A. L., Armes, S. P., & Tanaka, M. (2015). Live cell tracking of symmetry break in actin cytoskeleton triggered by abrupt changes in micromechanical environments. *Biomaterials Science*, *3*, 1539–1544. https://doi.org/10.1039/C5BM00205B

Iozzo, R. V., & Gubbiotti, M. A. (2018). Extracellular matrix: The driving force of mammalian diseases. *Matrix Biology*, *71-72*, 1–9. https://doi.org/10.1016/J.MATBIO.2018.03.023

Ishihara, S., Kurosawa, H., & Haga, H. (2023). Stiffness-Modulation of Collagen Gels by Genipin-Crosslinking for Cell Culture. *Gels*, *9*(2), 148. https://doi.org/10.3390/gels9020148

Isomursu, A., Park, K. Y., Hou, J., Cheng, B., Mathieu, M., Shamsan, G. A., Fuller, B., Kasim, J., Mahmoodi, M. M., Lu, T. J., Genin, G. M., Xu, F., Lin, M., Distefano, M. D., Ivaska, J., & Odde, D. J. (2022). Directed cell migration towards softer environments. *Nature Materials*, *21*(9), 1081–1090. https://doi.org/10.1038/s41563-022-01294-2

Janmey, P. A., Fletcher, D. A., & Reinhart-King, C. A. (2020). Stiffness sensing by cells. *Physiological Reviews*, *100*, 695–724. https://doi.org/10.1152/physrev.00013.2019

Jeon, H., Hidai, H., Hwang, D. J., Healy, K. E., & Grigoropoulos, C. P. (2010). The effect of micron-scale anisotropic cross patterns on fibroblast migration. *Biomaterials*, *31*(15), 4286–4295. https://doi.org/10.1016/j.biomaterials.2010.01.103

Ji, C., & Huang, Y. (2023). Durotaxis and negative durotaxis: where should cells go? *Communications Biology*, *6*, 1169. https://doi.org/10.1038/s42003-023-05554-y

Jiang, X., Bruzewicz, D. A., Wong, A. P., Piel, M., & Whitesides, G. M. (2005). Directing cell migration with asymmetric micropatterns. *Proceedings of the National Academy of Sciences of the United States of America*, *102*(4), 975–978. https://doi.org/10.1073/pnas.0408954102

Kassianidou, E., Probst, D., Jäger, J., Lee, S., Roguet, A. L., Schwarz, U. S., & Kumar, S. (2019). Extracellular Matrix Geometry and Initial Adhesive Position Determine Stress Fiber Network Organization during Cell Spreading. *Cell Reports*, *27*, 1897. https://doi.org/10.1016/J.CELREP.2019.04.035

Khuntia, P., Rawal, S., Marwaha, R., & Das, T. (2022). Actin-driven Golgi apparatus dispersal during collective migration of epithelial cells. *Proceedings of the National Academy of Sciences of the United States of America*, *119*(26), e2204808119. https://doi.org/10.1073/pnas.2204808119

Kiefer, P., Hahn, V., Nardi, M., Yang, L., Blasco, E., Barner-Kowollik, C., & Wegener, M. (2020). Sensitive Photoresists for Rapid Multiphoton 3D Laser Micro- and Nanoprinting. *Advanced Optical Materials*, *8*(19), 2000895. https://doi.org/10.1002/ADOM.202000895

Kim, J., Cao, Y., Eddy, C., Deng, Y., Levine, H., Rappel, W. J., & Sun, B. (2021). The mechanics and dynamics of cancer cells sensing noisy 3D contact guidance. *Proceedings of the National Academy of Sciences of the United States of America*, *118*(10), e2024780118. https://doi.org/10.1073/pnas.2024780118

Kim, T. J. (2021). Mechanobiology: A New Frontier in Biology. *Biology*, *10*, 570. https://doi.org/10.3390/biology10070570

Kirkbride, K. C., Hong, N. H., French, C. L., Clark, E. S., Jerome, W. G., & Weaver, A. M. (2012). Regulation of late endosomal/lysosomal maturation and trafficking by cortactin affects Golgi morphology. *Cytoskeleton*, *69*(9), 625–643. https://doi.org/10.1002/CM.21051

Kodaka, M., & Hata, Y. (2015). The mammalian Hippo pathway: regulation and function of YAP1 and TAZ. *Cellular and Molecular Life Sciences*, *72*(2), 285–306. https://doi.org/10.1007/S00018-014-1742-9

Kolega, J. (2003). Asymmetric Distribution of Myosin IIB in Migrating Endothelial Cells Is Regulated by a rho-dependent Kinase and Contributes to Tail Retraction. *Molecular Biology of the Cell*, *14*(12), 4745–4757. https://doi.org/10.1091/mbc.E03-04-0205

Kovács, M., Wang, F., Hu, A., Zhang, Y., & Sellers, J. R. (2003). Functional Divergence of Human Cytoplasmic Myosin II: Kinetic Characterization of the Non-Muscle IIA Isoform. *Journal of Biological Chemistry*, *278*(40), 38132–38140. https://doi.org/10.1074/JBC.M305453200

Kubow, K. E., Shuklis, V. D., Sales, D. J., & Horwitz, A. R. (2017). Contact guidance persists under myosin inhibition due to the local alignment of adhesions and individual protrusions. *Scientific Reports*, *7*, 14380. https://doi.org/10.1038/s41598-017-14745-7

Kuo, J. C., Han, X., Hsiao, C. T., Yates, J. R., & Waterman, C. M. (2011). Analysis of the myosin-II-responsive focal adhesion proteome reveals a role for β-Pix in negative regulation of focal adhesion maturation. *Nature Cell Biology*, *13*, 383–393. https://doi.org/10.1038/ncb2216

Kuragano, M., Murakami, Y., & Takahashi, M. (2018). Nonmuscle myosin IIA and IIB differentially contribute to intrinsic and directed migration of human embryonic lung fibroblasts. *Biochemical and Biophysical Research Communications*, *498*, 25–31. https://doi.org/10.1016/J.BBRC.2018.02.171

Kuroda, M., Wada, H., Kimura, Y., Ueda, K., & Kioka, N. (2017). Vinculin promotes nuclear localization of TAZ to inhibit ECM stiffness-dependent differentiation into adipocytes. *Journal of Cell Science*, *130*(5), 989–1002. https://doi.org/10.1242/jcs.194779

Kwon, K. W., Park, H., Song, K. H., Choi, J.-C., Ahn, H., Park, M. J., Suh, K.-Y., & Doh, J. (2012). Nanotopography-Guided Migration of T Cells. *The Journal of Immunology*, *189*(5), 2266–2273. https://doi.org/10.4049/JIMMUNOL.1102273

Ladoux, B., & Mège, R. M. (2017). Mechanobiology of collective cell behaviours. *Nature Reviews Molecular Cell Biology*, *18*(12), 743–757. https://doi.org/10.1038/nrm.2017.98

LaFratta, C. N., Fourkas, J. T., Baldacchini, T., & Farrer, R. A. (2007). Multiphoton Fabrication. *Angewandte Chemie International Edition*, *46*(33), 6238–6258. https://doi.org/10.1002/ANIE.200603995

Lappalainen, P., Kotila, T., Jégou, A., & Romet-Lemonne, G. (2022). Biochemical and mechanical regulation of actin dynamics. *Nature Reviews Molecular Cell Biology*, *23*, 836–852. https://doi.org/10.1038/s41580-022-00508-4

Lavrentieva, A., Fleischhammer, T., Enders, A., Pirmahboub, H., Bahnemann, J., & Pepelanova, I. (2020). Fabrication of Stiffness Gradients of GelMA Hydrogels Using a 3D Printed Micromixer. *Macromolecular Bioscience*, *20*(7), 2000107. https://doi.org/10.1002/MABI.202000107

Lázaro-Diéguez, F., Jiménez, N., Barth, H., Koster, A. J., Renau-Piqueras, J., Llopis, J. L., Burger, K. N., & Egea, G. (2006). Actin filaments are involved in the maintenance of Golgi cisternae morphology and intra-Golgi pH. *Cell Motility and the Cytoskeleton*, *63*, 778–791. https://doi.org/10.1002/CM.20161

Leclech, C., & Barakat, A. I. (2021). Is there a universal mechanism of cell alignment in response to substrate topography? *Cytoskeleton*, *78*(6), 284–292. https://doi.org/10.1002/CM.21661

Leclech, C., & Villard, C. (2020). Cellular and Subcellular Contact Guidance on Microfabricated Substrates. *Frontiers in Bioengineering and Biotechnology*, *8*, 551505. https://doi.org/10.3389/fbioe.2020.551505

Lee, K., Kim, E. H., Oh, N., Tuan, N. A., Bae, N. H., Lee, S. J., Lee, K. G., Eom, C. Y., Yim, E. K., & Park, S. (2016). Contribution of actin filaments and microtubules to cell elongation and alignment depends on the grating depth of micrograting. *Journal of Nanobiotechnology*, *14*, 35. https://doi.org/10.1186/s12951-016-0187-8

Lees, C., Vincent, J. F., & Hillerton, J. E. (1991). Poisson's ratio in skin. *Bio-Medical Materials and Engineering*, *1*(1), 19–23. https://doi.org/10.3233/BME-1991-1104

Lehnert, D., Wehrle-Haller, B., David, C., Weiland, U., Ballestrem, C., Imhof, B. A., & Bastmeyer, M. (2004). Cell behaviour on micropatterned substrata: limits of extracellular matrix geometry for spreading and adhesion. *Journal of Cell Science*, *117*(1), 41–52. https://doi.org/10.1242/JCS.00836

Li, B., Wang, Z., Wu, H., Xue, M., Lin, P., Wang, S., Lin, N., Huang, X., Pan, W., Liu, M., Yan, X., Qu, H., Sun, L., Li, H., Wu, Y., Teng, W., Wang, Z., Zhou, X., Chen, H., … Ye, Z. (2018). Epigenetic regulation of CXCL12 plays a critical role in mediating tumor progression and the immune response in osteosarcoma. *Cancer Research*, *78*(14), 3938–3953. https://doi.org/10.1158/0008-5472.CAN-17-3801

Li, Q., Makhija, E., Hameed, F. M., & Shivashankar, G. V. (2015). Micropillar displacements by cell traction forces are mechanically correlated with nuclear dynamics. *Biochemical and Biophysical Research Communications*, *461*(2), 372–377. https://doi.org/10.1016/j.bbrc.2015.04.041

Lin, C. H., Espreafico, E. M., Mooseker, M. S., & Forscher, P. (1996). Myosin Drives Retrograde F-Actin Flow in Neuronal Growth Cones. *Neuron*, *16*, 769–782. https://doi.org/10.1016/S0896-6273(00)80097-5

Lin, T., Zeng, L., Liu, Y., DeFea, K., Schwartz, M. A., Chien, S., & Shyy, J. Y. (2003). Rho-ROCK-LIMK-cofilin pathway regulates shear stress activation of sterol regulatory element binding proteins. *Circulation Research*, *92*(12), 1296–1304. https://doi.org/10.1161/01.RES.0000078780.65824.8B

Linke, P., Suzuki, R., Yamamoto, A., Nakahata, M., Kengaku, M., Fujiwara, T., Ohzono, T., & Tanaka, M. (2019). Dynamic Contact Guidance of Myoblasts by Feature Size and Reversible Switching of Substrate Topography: Orchestration of Cell Shape, Orientation, and Nematic Ordering of Actin Cytoskeletons. *Langmuir*, *35*(23), 7538–7551. https://doi.org/10.1021/acs.langmuir.8b02972

Liu, J. F., Chen, P. C., Chang, T. M., & Hou, C. H. (2020). Monocyte Chemoattractant Protein-1 promotes cancer cell migration via c-Raf/MAPK/AP-1 pathway and MMP-9 production in osteosarcoma. *Journal of Experimental and Clinical Cancer Research*, *39*, 254. https://doi.org/10.1186/s13046-020-01756-y

Liu, Y. J., Le Berre, M., Lautenschlaeger, F., Maiuri, P., Callan-Jones, A., Heuzé, M., Takaki, T., Voituriez, R., & Piel, M. (2015). Confinement and Low Adhesion Induce Fast Amoeboid

Migration of Slow Mesenchymal Cells. *Cell*, *160*(4), 659–672. https://doi.org/10.1016/J.CELL.2015.01.007

Lo, C. M., Wang, H. B., Dembo, M., & Wang, Y. L. (2000). Cell Movement Is Guided by the Rigidity of the Substrate. *Biophysical Journal*, *79*(1), 144–152. https://doi.org/10.1016/S0006-3495(00)76279-5

Lomakin, A. J., Cattin, C. J., Cuvelier, D., Alraies, Z., Molina, M., Nader, G. P., Srivastava, N., Saez, P. J., Garcia-Arcos, J. M., Zhitnyak, I. Y., Bhargava, A., Driscoll, M. K., Welf, E. S., Fiolka, R., Petrie, R. J., de Silva, N. S., González-Granado, J. M., Manel, N., Lennon-Duménil, A. M., … Piel, M. (2020). The nucleus acts as a ruler tailoring cell responses to spatial constraints. *Science*, *370*(6514), eaba2894. https://doi.org/10.1126/science.aba2894

Low, B. C., Pan, C. Q., Shivashankar, G. V., Bershadsky, A., Sudol, M., & Sheetz, M. (2014). YAP/TAZ as mechanosensors and mechanotransducers in regulating organ size and tumor growth. *FEBS Letters*, *588*(16), 2663–2670. https://doi.org/10.1016/j.febslet.2014.04.012

Lowe, D. G. (2004). Distinctive image features from scale-invariant keypoints. *International Journal of Computer Vision*, *60*(2), 91–110. https://doi.org/10.1023/B:VISI.0000029664.99615.94

Lutolf, M. P., Doyonnas, R., Havenstrite, K., Koleckar, K., & Blau, H. M. (2009). Perturbation of single hematopoietic stem cell fates in artificial niches. *Integrative Biology*, *1*(1), 59–69. https://doi.org/10.1039/B815718A

Lvov, V. A., Senatov, F. S., Veveris, A. A., Skrybykina, V. A., & Lantada, A. D. (2022). Auxetic Metamaterials for Biomedical Devices: Current Situation, Main Challenges, and Research Trends. *Materials*, *15*(4), 1439. https://doi.org/10.3390/MA15041439

Maekawa, M., Ishizaki, T., Boku, S., Watanabe, N., Fujita, A., Iwamatsu, A., Obinata, T., Ohashi, K., Mizuno, K., & Narumiya, S. (1999). Signaling from Rho to the actin cytoskeleton through protein kinases ROCK and LIM-kinase. *Science*, *285*(5429), 895–898. https://doi.org/10.1126/science.285.5429.895

Mao, A. S., Shin, J. W., & Mooney, D. J. (2016). Effects of substrate stiffness and cell-cell contact on mesenchymal stem cell differentiation. *Biomaterials*, *98*, 184–191. https://doi.org/10.1016/j.biomaterials.2016.05.004

Maruo, S., Nakamura, O., & Kawata, S. (1997). Three-dimensional microfabrication with two-photon-absorbed photopolymerization. *Optics Letters*, *22*(2), 132–134. https://doi.org/10.1364/OL.22.000132

Matsumura, F. (2005). Regulation of myosin II during cytokinesis in higher eukaryotes. *Trends in Cell Biology*, *15*(7), 371–377. https://doi.org/10.1016/j.tcb.2005.05.004

Maupin, P., Phillips, C., Adelstein, R., & Pollard, T. (1994). Differential localization of myosin-II isozymes in human cultured cells and blood cells. *Journal of Cell Science*, *107*(11), 3077–3090. https://doi.org/10.1242/jcs.107.11.3077

Mierke, C. T. (2021). Bidirectional Mechanical Response Between Cells and Their Microenvironment. *Frontiers in Physics*, *9*, 749830. https://doi.org/10.3389/fphy.2021.749830

Miller, P. M., Folkmann, A. W., Maia, A. R., Efimova, N., Efimov, A., & Kaverina, I. (2009). Golgi-derived CLASP-dependent microtubules control Golgi organization and polarized trafficking in motile cells. *Nature Cell Biology*, *11*(9), 1069–1080. https://doi.org/10.1038/ncb1920

Mitchison, T., & Kirschner, M. (1988). Cytoskeletal dynamics and nerve growth. *Neuron*, *1*(9), 761–772. https://doi.org/10.1016/0896-6273(88)90124-9

Muinonen-Martin, A. J., Veltman, D. M., Kalna, G., & Insall, R. H. (2010). An Improved Chamber for Direct Visualisation of Chemotaxis. *PLOS ONE*, *5*(12), e15309. https://doi.org/10.1371/journal.pone.0015309

Munding, N., Fladung, M., Chen, Y., Hippler, M., Ho, A. D., Wegener, M., Bastmeyer, M., & Tanaka, M. (2023). Bio-Metamaterials for Mechano-Regulation of Mesenchymal Stem Cells. *Advanced Functional Materials*, 2301133. https://doi.org/10.1002/ADFM.202301133

Müsch, A., Cohen, D., & Rodriguez-Boulan, E. (1997). Myosin II Is Involved in the Production of Constitutive Transport Vesicles from the TGN. *Journal of Cell Biology*, *138*, 291–306. https://doi.org/10.1083/JCB.138.2.291

Nakasawa, T., Takahashi, M., Matsuzawa, F., Aikawa, S., Togashi, Y., Saitoh, T., Yamagishi, A., & Yazawa, M. (2005). Critical regions for assembly of vertebrate nonmuscle myosin II. *Biochemistry*, *44*(1), 174–183. https://doi.org/10.1021/bi048807h

Nardone, G., Oliver-De La Cruz, J., Vrbsky, J., Martini, C., Pribyl, J., Skládal, P., Pešl, M., Caluori, G., Pagliari, S., Martino, F., Maceckova, Z., Hajduch, M., Sanz-Garcia, A., Pugno, N. M., Stokin, G. B., & Forte, G. (2017). YAP regulates cell mechanics by controlling focal adhesion assembly. *Nature Communications*, *8*, 15321. https://doi.org/10.1038/ncomms15321

Newell-Litwa, K. A., Horwitz, R., & Lamers, M. L. (2015). Non-Muscle myosin II in disease: Mechanisms and therapeutic opportunities. *DMM Disease Models and Mechanisms*, *8*(12), 1495–1515. https://doi.org/10.1242/dmm.022103

Niederman, R., & Pollard, T. D. (1975). Human platelet myosin. II. In vitro assembly and structure of myosin filaments. *Journal of Cell Biology*, *67*(1), 72–92. https://doi.org/10.1083/JCB.67.1.72

O'Halloran, S., Pandit, A., Heise, A., & Kellett, A. (2023). Two-Photon Polymerization: Fundamentals, Materials, and Chemical Modification Strategies. *Advanced Science*, *10*(7), 2204072. https://doi.org/10.1002/ADVS.202204072

Ovsianikov, A., Deiwick, A., Van Vlierberghe, S., Pflaum, M., Wilhelmi, M., Dubruel, P., & Chichkov, B. (2011). Laser Fabrication of 3D Gelatin Scaffolds for the Generation of Bioartificial Tissues. *Materials 2011*, *4*(1), 288–299. https://doi.org/10.3390/MA4010288

Pagliara, S., Franze, K., McClain, C. R., Wylde, G. W., Fisher, C. L., Franklin, R. J., Kabla, A. J., Keyser, U. F., & Chalut, K. J. (2014). Auxetic nuclei in embryonic stem cells exiting pluripotency. *Nature Materials*, *13*, 638–644. https://doi.org/10.1038/nmat3943

Panciera, T., Azzolin, L., Cordenonsi, M., & Piccolo, S. (2017). Mechanobiology of YAP and TAZ in physiology and disease. *Nature Reviews Molecular Cell Biology*, *18*, 758–770. https://doi.org/10.1038/nrm.2017.87

Pang, X., He, X., Qiu, Z., Zhang, H., Xie, R., Liu, Z., Gu, Y., Zhao, N., Xiang, Q., & Cui, Y. (2023). Targeting integrin pathways: mechanisms and advances in therapy. *Signal Transduction and Targeted Therapy*, *8*(1), 1–42. https://doi.org/10.1038/s41392-022-01259-6

Pao, Y. H., & Rentzepis, P. M. (1965). Multiphoton Absorption and Optical-Harmonic Generation in Highly Absorbing Molecular Crystals. *The Journal of Chemical Physics*, *43*(4), 1281–1286. https://doi.org/10.1063/1.1696915

Pathak, M. M., Nourse, J. L., Tran, T., Hwe, J., Arulmoli, J., Le, D. T. T., Bernardis, E., Flanagan, L. A., & Tombola, F. (2014). Stretch-activated ion channel Piezo1 directs lineage choice in human neural stem cells. *Proceedings of the National Academy of Sciences of the United States of America*, *111*(45), 16148–16153. https://doi.org/10.1073/pnas.1409802111

Pellegrin, S., & Mellor, H. (2007). Actin stress fibres. *Journal of Cell Science*, *120*, 3491–3499. https://doi.org/10.1242/JCS.018473

Peng, Y., Chen, Z., He, Y., Li, P., Chen, Y., Chen, X., Jiang, Y., Qin, X., Li, S., Li, T., Wu, C., Yang, H., You, F., & Liu, Y. (2022). Non-muscle myosin II isoforms orchestrate substrate stiffness sensing to promote cancer cell contractility and migration. *Cancer Letters*, *524*, 245–258. https://doi.org/10.1016/J.CANLET.2021.10.030

Plotnikov, S. V., Pasapera, A. M., Sabass, B., & Waterman, C. M. (2012). Force fluctuations within focal adhesions mediate ECM-rigidity sensing to guide directed cell migration. *Cell*, *151*(7), 1513–1527. https://doi.org/10.1016/j.cell.2012.11.034

Pollard, T. D. (1986). Rate constants for the reactions of ATP- and ADP-actin with the ends of actin filaments. *Journal of Cell Biology*, *103*(6), 2747–2754. https://doi.org/10.1083/JCB.103.6.2747

Pollard, T. D., & Cooper, J. A. (2009). Actin, a central player in cell shape and movement. *Science*, *326*(5957), 1208–1212. https://doi.org/10.1126/science.1175862

Pouthas, F., Girard, P., Lecaudey, V., Ly, T. B. N., Gilmour, D., Boulin, C., Pepperkok, R., & Reynaud, E. G. (2008). In migrating cells, the Golgi complex and the position of the centrosome depend on geometrical constraints of the substratum. *Journal of Cell Science*, *121*(14), 2406–2414. https://doi.org/10.1242/JCS.026849

Provenzano, P. P., Inman, D. R., Eliceiri, K. W., Trier, S. M., & Keely, P. J. (2008). Contact Guidance Mediated Three-Dimensional Cell Migration is Regulated by Rho/ROCK-Dependent Matrix Reorganization. *Biophysical Journal*, *95*(11), 5374–5384. https://doi.org/10.1529/biophysj.108.133116

Raab, M., Swift, J., Dingal, P. C. P., Shah, P., Shin, J. W., & Discher, D. E. (2012). Crawling from soft to stiff matrix polarizes the cytoskeleton and phosphoregulates myosin-II heavy chain. *Journal of Cell Biology*, *199*(4), 669–683. https://doi.org/10.1083/jcb.201205056

Ravichandran, Y., Goud, B., & Manneville, J. B. (2020). The Golgi apparatus and cell polarity: Roles of the cytoskeleton, the Golgi matrix, and Golgi membranes. *Current Opinion in Cell Biology*, *62*, 104–113. https://doi.org/10.1016/J.CEB.2019.10.003

Ray, A., Lee, O., Win, Z., Edwards, R. M., Alford, P. W., Kim, D. H., & Provenzano, P. P. (2017). Anisotropic forces from spatially constrained focal adhesions mediate contact guidance directed cell migration. *Nature Communications*, *8*, 14923. https://doi.org/10.1038/ncomms14923

Reggiani, F., Gobbi, G., Ciarrocchi, A., & Sancisi, V. (2021). YAP and TAZ Are Not Identical Twins. *Trends in Biochemical Sciences*, *46*(2), 154–168. https://doi.org/10.1016/J.TIBS.2020.08.012

Rehfeldt, F., Engler, A. J., Eckhardt, A., Ahmed, F., & Discher, D. E. (2007). Cell responses to the mechanochemical microenvironment—Implications for regenerative medicine and drug

delivery. *Advanced Drug Delivery Reviews*, *59*, 1329–1339. https://doi.org/10.1016/j.addr.2007.08.007

Rens, E. G., & Merks, R. M. (2020). Cell Shape and Durotaxis Explained from Cell-Extracellular Matrix Forces and Focal Adhesion Dynamics. *iScience*, *23*, 101488. https://doi.org/10.1016/J.ISCI.2020.101488

Reversat, A., Gaertner, F., Merrin, J., Stopp, J., Tasciyan, S., Aguilera, J., de Vries, I., Hauschild, R., Hons, M., Piel, M., Callan-Jones, A., Voituriez, R., & Sixt, M. (2020). Cellular locomotion using environmental topography. *Nature*, *582*, 582–585. https://doi.org/10.1038/s41586-020-2283-z

Ridley, A. J., Schwartz, M. A., Burridge, K., Firtel, R. A., Ginsberg, M. H., Borisy, G., Parsons, J. T., & Horwitz, A. R. (2003). Cell Migration: Integrating Signals from Front to Back. *Science*, *302*(5651), 1704–1709. https://doi.org/10.1126/science.109205

Rivero, S., Cardenas, J., Bornens, M., & Rios, R. M. (2009). Microtubule nucleation at the cis-side of the golgi apparatus requires AKAP450 and GM130. *EMBO Journal*, *28*, 1016–1028. https://doi.org/10.1038/emboj.2009.47

Rosenfeld, S. S., Xing, J., Chen, L. Q., & Sweeney, H. L. (2003). Myosin IIB is unconventionally conventional. *Journal of Biological Chemistry*, *278*(30), 27449–27455. https://doi.org/10.1074/jbc.M302555200

Sandquist, J. C., Swenson, K. I., DeMali, K. A., Burridge, K., & Means, A. R. (2006). Rho kinase differentially regulates phosphorylation of nonmuscle myosin II isoforms A and B during cell rounding and migration. *Journal of Biological Chemistry*, *281*(47), 35873–35883. https://doi.org/10.1074/jbc.M605343200

Sato, Y., Kamijo, K., Tsutsumi, M., Murakami, Y., & Takahashi, M. (2020). Nonmuscle myosin IIA and IIB differently suppress microtubule growth to stabilize cell morphology. *The Journal of Biochemistry*, *167*(1), 25–39. https://doi.org/10.1093/jb/mvz082

Schindelin, J., Arganda-Carreras, I., Frise, E., Kaynig, V., Longair, M., Pietzsch, T., Preibisch, S., Rueden, C., Saalfeld, S., Schmid, B., Tinevez, J. Y., White, D. J., Hartenstein, V., Eliceiri, K., Tomancak, P., & Cardona, A. (2012). Fiji: an open-source platform for biological-image analysis. *Nature Methods*, *9*(7), 676–682. https://doi.org/10.1038/nmeth.2019

Schoen, I., Hu, W., Klotzsch, E., & Vogel, V. (2010). Probing cellular traction forces by micropillar arrays: Contribution of substrate warping to pillar deflection. *Nano Letters*, *10*(5), 1823–1830. https://doi.org/10.1021/nl100533c

Shutova, M. S., & Svitkina, T. M. (2018). Mammalian nonmuscle myosin II comes in three flavors. *Biochemical and Biophysical Research Communications*, *506*(2), 394–402. https://doi.org/10.1016/j.bbrc.2018.03.103

Shutova, M. S., Spessott, W. A., Giraudo, C. G., & Svitkina, T. (2014). Endogenous species of mammalian nonmuscle myosin IIA and IIB include activated monomers and heteropolymers. *Current Biology*, *24*(17), 1958–1968. https://doi.org/10.1016/j.cub.2014.07.070

Shutova, M. S., Asokan, S. B., Talwar, S., Assoian, R. K., Bear, J. E., & Svitkina, T. M. (2017). Self-sorting of nonmuscle myosins IIA and IIB polarizes the cytoskeleton and modulates cell motility. *Journal of Cell Biology*, *216*(9), 2877–2889. https://doi.org/10.1083/jcb.201705167

Skinner, B. F. (1971). *Beyond Freedom & Dignity*. Penguin Books Ltd.

Solon, J., Levental, I., Sengupta, K., Georges, P. C., & Janmey, P. A. (2007). Fibroblast Adaptation and Stiffness Matching to Soft Elastic Substrates. *Biophysical Journal*, *93*, 4453–4461. https://doi.org/10.1529/BIOPHYSJ.106.101386

Sunyer, R., & Trepat, X. (2020). Durotaxis. *Current Biology*, *30*(9), R383–R387. https://doi.org/10.1016/J.CUB.2020.03.051

Sunyer, R., Jin, A. J., Nossal, R., & Sackett, D. L. (2012). Fabrication of Hydrogels with Steep Stiffness Gradients for Studying Cell Mechanical Response. *PLOS ONE*, *7*(10), e46107. https://doi.org/10.1371/journal.pone.0046107

Taneja, N., & Burnette, D. T. (2019). Myosin IIA drives membrane bleb retraction. *Molecular Biology of the Cell*, *30*(9), 1051–1059. https://doi.org/10.1091/mbc.E18-11-0752

Teixeira, A. I., Abrams, G. A., Bertics, P. J., Murphy, C. J., & Nealey, P. F. (2003). Epithelial contact guidance on well-defined micro- and nanostructured substrates. *Journal of Cell Science*, *116*(10), 1881–1892. https://doi.org/10.1242/JCS.00383

Tenney, R. M., & Discher, D. E. (2009). Stem cells, microenvironment mechanics, and growth factor activation. *Current Opinion in Cell Biology*, *21*(5), 630–635. https://doi.org/10.1016/j.ceb.2009.06.003

Théry, M., Pépin, A., Dressaire, E., Chen, Y., & Bornens, M. (2006). Cell distribution of stress fibres in response to the geometry of the adhesive environment. *Cell Motility and the Cytoskeleton*, *63*, 341–355. https://doi.org/10.1002/CM.20126

Théry, M., Racine, V., Piel, M., Pépin, A., Dimitrov, A., Chen, Y., Sibarita, J. B., & Bornens, M. (2006). Anisotropy of cell adhesive microenvironment governs cell internal organization and orientation of polarity. *Proceedings of the National Academy of Sciences of the United States of America*, *103*(52), 19771–19776. https://doi.org/10.1073/pnas.0609267103

Thomas, D. G., Yenepalli, A., Denais, C. M., Rape, A., Beach, J. R., li Wang, Y., Schiemann, W. P., Baskaran, H., Lammerding, J., & Egelhoff, T. T. (2015). Non-muscle myosin IIB is critical for nuclear translocation during 3D invasion. *The Journal of Cell Biology*, *210*(4), 583. https://doi.org/10.1083/jcb.201502039

Tirella, A., Liberto, T., & Ahluwalia, A. (2012). Riboflavin and collagen: New crosslinking methods to tailor the stiffness of hydrogels. *Materials Letters*, *74*, 58–61. https://doi.org/10.1016/j.matlet.2012.01.036

Tojkander, S., Gateva, G., & Lappalainen, P. (2012). Actin stress fibers - Assembly, dynamics and biological roles. *Journal of Cell Science*, *125*(8), 1855–1864. https://doi.org/10.1242/jcs.098087

Tong, M. H., Huang, N., Ngan, A. H. W., Du, Y., & Chan, B. P. (2017). Preferential sensing and response to microenvironment stiffness of human dermal fibroblast cultured on protein micropatterns fabricated by 3D multiphoton biofabrication. *Scientific Reports*, *7*, 12402. https://doi.org/10.1038/s41598-017-12604-z

Totsukawa, G., Yamakita, Y., Yamashiro, S., Hartshorne, D. J., Sasaki, Y., & Matsumura, F. (2000). Distinct roles of ROCK (Rho-kinase) and MLCK in spatial regulation of MLC phosphory-

lation for assembly of stress fibers and focal adhesions in 3T3 fibroblasts. *Journal of Cell Biology*, *150*(4), 797–806. https://doi.org/10.1083/jcb.150.4.797

Tse, J. R., & Engler, A. J. (2011). Stiffness Gradients Mimicking In Vivo Tissue Variation Regulate Mesenchymal Stem Cell Fate. *PLOS ONE*, *6*(1), e15978. https://doi.org/10.1371/JOURNAL.PONE.0015978

Turner, C. E. (2000). Paxillin and focal adhesion signalling. *Nature Cell Biology*, *2*, E231–E236. https://doi.org/10.1038/35046659

Valderrama, F., Babià, T., Ayala, I., Kok, J. W., Renau-Piqueras, J., & Egea, G. (1998). Actin microfilaments are essential for the cytological positioning and morphology of the Golgi complex. *European Journal of Cell Biology*, *76*, 9–17. https://doi.org/10.1016/S0171-9335(98)80012-5

Valderrama, F., Durán, J. M., Babià, T., Barth, H., Renau-Piqueras, J., & Egea, G. (2001). Actin Microfilaments Facilitate the Retrograde Transport from the Golgi Complex to the Endoplasmic Reticulum in Mammalian Cells. *Traffic*, *2*(10), 717–726. https://doi.org/10.1034/j.1600-0854.2001.21006.x

Vale, R. D., & Milligan, R. A. (2000). The way things move: Looking under the hood of molecular motor proteins. *Science*, *288*(5463), 88–95. https://doi.org/10.1126/science.288.5463.88

Vazquez-Martel, C., Florido Martins, L., Genthner, E., Almeida, C., Martel Quintana, A., Bastmeyer, M., Gómez Pinchetti, J. L., & Blasco, E. (2024). Printing Green: Microalgae-Based Materials for 3D Printing with Light. *Advanced Materials*, *36*(33), 2402786. https://doi.org/10.1002/ADMA.202402786

Vicente-Manzanares, M., Zareno, J., Whitmore, L., Choi, C. K., & Horwitz, A. F. (2007). Regulation of protrusion, adhesion dynamics, and polarity by myosins IIA and IIB in migrating cells. *Journal of Cell Biology*, *176*(5), 573–580. https://doi.org/10.1083/jcb.200612043

Vicente-Manzanares, M., Ma, X., Adelstein, R. S., & Horwitz, A. R. (2009). Non-muscle myosin II takes centre stage in cell adhesion and migration. *Nature Reviews Molecular Cell Biology*, *10*, 778–790. https://doi.org/10.1038/nrm2786

Vicente-Manzanares, M., Newell-Litwa, K., Bachir, A. I., Whitmore, L. A., & Horwitz, A. R. (2011). Myosin IIA/IIB restrict adhesive and protrusive signaling to generate front-back polarity in migrating cells. *Journal of Cell Biology*, *193*(2), 381–396. https://doi.org/10.1083/jcb.201012159

Vincent, L. G., Choi1, Suk, Y., Alonso-Latorre, B., del Álamo, J. C., & Engler, A. J. (2013). Mesenchymal stem cell durotaxis depends on substrate stiffness gradient strength. *Biotechnology Journal*, *8*, 472–484. https://doi.org/10.1002/BIOT.201200205

Vogel, V., & Sheetz, M. (2006). Local force and geometry sensing regulate cell functions. *Nature Reviews Molecular Cell Biology*, *7*(4), 265–275. https://doi.org/10.1038/nrm1890

Wada, K. I., Itoga, K., Okano, T., Yonemura, S., & Sasaki, H. (2011). Hippo pathway regulation by cell morphology and stress fibers. *Development*, *138*, 3907–3914. https://doi.org/10.1242/DEV.070987

Wang, C., Vangelatos, Z., Winston, T., Sun, S., Grigoropoulos, C. P., & Ma, Z. (2022). Remodeling of Architected Mesenchymal Microtissues Generated on Mechanical Metamaterials. *3D Printing and Additive Manufacturing*, *9*(6), 483–489. https://doi.org/10.1089/3DP.2021.0091

Wang, F., Harvey, E. V., Conti, M. A., Wei, D., & Sellers, J. R. (2000). A conserved negatively charged amino acid modulates function in human nonmuscle myosin IIA. *Biochemistry*, *39*(18), 5555–5560. https://doi.org/10.1021/bi000133x

Wang, F., Kovács, M., Hu, A., Limouze, J., Harvey, E. V., & Sellers, J. R. (2003). Kinetic Mechanism of Non-muscle Myosin IIB: Functional Adaptations for Tension Generation and Maintenance. *Journal of Biological Chemistry*, *278*(30), 27439–27448. https://doi.org/10.1074/JBC.M302510200

Wang, J., & Schneider, I. C. (2017). Myosin phosphorylation on stress fibers predicts contact guidance behavior across diverse breast cancer cells. *Biomaterials*, *120*, 81–93. https://doi.org/10.1016/j.biomaterials.2016.11.035

Weiss, P. (1934). In vitro experiments on the factors determining the course of the outgrowing nerve fiber. *Journal of Experimental Zoology*, *68*(3), 393–448. https://doi.org/10.1002/JEZ.1400680304

Weißenbruch, K., Grewe, J., Hippler, M., Fladung, M., Tremmel, M., Stricker, K., Schwarz, U. S., & Bastmeyer, M. (2021). Distinct roles of nonmuscle myosin ii isoforms for establishing tension and elasticity during cell morphodynamics. *eLife*, *10*, e71888. https://doi.org/10.7554/eLife.71888

Weißenbruch, K., Fladung, M., Grewe, J., Baulesch, L., Schwarz, U. S., & Bastmeyer, M. (2022). Nonmuscle myosin IIA dynamically guides regulatory light chain phosphorylation and assembly of nonmuscle myosin IIB. *European Journal of Cell Biology*, *101*(2), 151213. https://doi.org/10.1016/J.EJCB.2022.151213

Williams, J. L., & Lewis, J. L. (1982). Properties and an Anisotropic Model of Cancellous Bone From the Proximal Tibial Epiphysis. *Journal of Biomechanical Engineering*, *104*(1), 50–56. https://doi.org/10.1115/1.3138303

Wolf, K., Müller, R., Borgmann, S., Bröcker, E. B., & Friedl, P. (2003). Amoeboid shape change and contact guidance: T-lymphocyte crawling through fibrillar collagen is independent of matrix remodeling by MMPs and other proteases. *Blood*, *102*(9), 3262–3269. https://doi.org/10.1182/BLOOD-2002-12-3791

Yadav, S., Puri, S., & Linstedt, A. D. (2009). A primary role for golgi positioning in directed secretion, cell polarity, and wound healing. *Molecular Biology of the Cell*, *20*(6), 1728–1736. https://doi.org/10.1091/mbc.e08-10-1077

Yamamoto, K., Otomo, K., Nemoto, T., Ishihara, S., Haga, H., Nagasaki, A., Murakami, Y., & Takahashi, M. (2019). Differential contributions of nonmuscle myosin IIA and IIB to cytokinesis in human immortalized fibroblasts. *Experimental Cell Research*, *376*(1), 67–76. https://doi.org/10.1016/j.yexcr.2019.01.020

Yan, Y., Li, Y., Song, L., Zeng, C., & Li, Y. (2017). Pluripotent stem cell expansion and neural differentiation in 3-D scaffolds of tunable Poisson's ratio. *Acta Biomaterialia*, *49*, 192–203. https://doi.org/10.1016/J.ACTBIO.2016.11.025

Yang, L., Münchinger, A., Kadic, M., Hahn, V., Mayer, F., Blasco, E., Barner-Kowollik, C., & Wegener, M. (2019). On the Schwarzschild Effect in 3D Two-Photon Laser Lithography. *Advanced Optical Materials*, *7*(22), 1901040. https://doi.org/10.1002/ADOM.201901040

Yao, M., Goult, B. T., Chen, H., Cong, P., Sheetz, M. P., & Yan, J. (2014). Mechanical activation of vinculin binding to talin locks talin in an unfolded conformation. *Scientific Reports*, *4*, 4610. https://doi.org/10.1038/srep04610

Yeoman, B., Shatkin, G., Beri, P., Banisadr, A., Katira, P., & Engler, A. J. (2021). Adhesion strength and contractility enable metastatic cells to become adurotactic. *Cell Reports*, *34*(10), 108816. https://doi.org/10.1016/J.CELREP.2021.108816

Yoshikawa, H. Y., Kawano, T., Matsuda, T., Kidoaki, S., & Tanaka, M. (2013). Morphology and adhesion strength of myoblast cells on photocurable gelatin under native and non-native micromechanical environments. *Journal of Physical Chemistry B*, *117*(15), 4081–4088. https://doi.org/10.1021/jp4008224

Zanconato, F., Forcato, M., Battilana, G., Azzolin, L., Quaranta, E., Bodega, B., Rosato, A., Bicciato, S., Cordenonsi, M., & Piccolo, S. (2015). Genome-wide association between YAP/TAZ/TEAD and AP-1 at enhancers drives oncogenic growth. *Nature Cell Biology*, *17*(9), 1218–1227. https://doi.org/10.1038/ncb3216

Zenker, J., White, M. D., Gasnier, M., Alvarez, Y. D., Lim, H. Y. G., Bissiere, S., Biro, M., & Plachta, N. (2018). Expanding Actin Rings Zipper the Mouse Embryo for Blastocyst Formation. *Cell*, *173*(3), 776–791.e17. https://doi.org/10.1016/j.cell.2018.02.035

Zhang, J., & Xiao, P. (2018). 3D printing of photopolymers. *Polymer Chemistry*, *9*(13), 1530–1540. https://doi.org/10.1039/C8PY00157J

Zhang, W., Soman, P., Meggs, K., Qu, X., & Chen, S. (2013). Tuning the Poisson's Ratio of Biomaterials for Investigating Cellular Response. *Advanced Functional Materials*, *23*(25), 3226–3232. https://doi.org/10.1002/ADFM.201202666

Zhao, F., Zhang, M., Nizamoglu, M., Kaper, H. J., Brouwer, L. A., Borghuis, T., Burgess, J. K., Harmsen, M. C., & Sharma, P. K. (2024). Fibroblast alignment and matrix remodeling induced by a stiffness gradient in a skin-derived extracellular matrix hydrogel. *Acta Biomaterialia*, *182*, 67–80. https://doi.org/10.1016/J.ACTBIO.2024.05.018

Zhao, X., & Guan, J. L. (2011). Focal adhesion kinase and its signaling pathways in cell migration and angiogenesis. *Advanced Drug Delivery Reviews*, *63*, 610–615. https://doi.org/10.1016/J.ADDR.2010.11.001

Zhovmer, A. S., Tabdanov, E. D., Miao, H., Wen, H., Chen, J., Luo, X., Ma, X., Provenzano, P. P., & Adelstein, R. S. (2019). The role of nonmuscle myosin 2A and 2B in the regulation of mesenchymal cell contact guidance. *Molecular Biology of the Cell*, *30*(16), 1961–1973. https://doi.org/10.1091/mbc.E19-01-0071

Zhu, X., & Kaverina, I. (2013). Golgi as an MTOC: Making microtubules for its own good. *Histochemistry and Cell Biology*, *140*, 361–367. https://doi.org/10.1007/s00418-013-1119-4

Publications

Fladung, M., Berkes, A., Alletzhaeusser, T., Chen, Y., Munding, N., Tanaka, M., Wegener, M., & Bastmeyer, M. (2025). What lies beyond—Insights into elastic microscaffolds with metamaterial properties for cell studies. *Current Opinion in Biomedical Engineering*, *33*, 100568. https://doi.org/10.1016/J.COBME.2024.100568.

Mainik, P., Aponte-Santamaría, C., Fladung, M., Curticean, R. E., Wacker, I., Hofhaus, G., Bastmeyer, M., Schröder, R. R., Gräter, F., & Blasco, E. (2024). Responsive 3D Printed Microstructures Based on Collagen Folding and Unfolding. *Small*, 2408597. https://doi.org/10.1002/SMLL.202408597.

Munding, N., Fladung, M., Chen, Y., Hippler, M., Ho, A. D., Wegener, M., Bastmeyer, M., & Tanaka, M. (2023). Bio-Metamaterials for Mechano-Regulation of Mesenchymal Stem Cells. *Advanced Functional Materials*, 2301133. https://doi.org/10.1002/ADFM.202301133
Note: Munding and Fladung contributed equally

Weißenbruch, K., Fladung, M., Grewe, J., Baulesch, L., Schwarz, U. S., & Bastmeyer, M. (2022). Nonmuscle myosin IIA dynamically guides regulatory light chain phosphorylation and assembly of nonmuscle myosin IIB. *European Journal of Cell Biology*, *101*(2), 151213. https://doi.org/10.1016/J.EJCB.2022.151213

Weißenbruch, K., Grewe, J., Hippler, M., Fladung, M., Tremmel, M., Stricker, K., Schwarz, U. S., & Bastmeyer, M. (2021). Distinct roles of nonmuscle myosin ii isoforms for establishing tension and elasticity during cell morphodynamics. *eLife*, *10*, e71888. https://doi.org/10.7554/eLife.71888

Acknowledgements

First, I would like to thank Prof. Dr. Martin Bastmeyer for giving me the opportunity to conduct my PhD thesis at his institute. I want to thank him for entrusting me with the metamaterial project; I greatly benefitted from the interdisciplinary work on a scientific and personal level. Further, I want to thank him for giving me the freedom to pursue my own ideas and supporting me in their realisation.

Next, I want to thank Prof. Dr. Martin Wegener for agreeing to be co-referee for my work. I greatly benefitted from the shared projects with him and his group members. Especially his keen insights and patience in discussing physics with a biologist significantly contributed to this work. Furthermore, I want to thank Prof. Dr. Motomu Tanaka for the continuous collaborative work and for welcoming me at his institute in Kyoto.

Another big thank you goes towards all my colleagues at the Zoological Institute. The warm atmosphere, stimulating scientific exchange and occasional private chit-chat made the years fly by. The continued testing of my IT skills remains a welcome distraction (at times). A special thanks goes to my desk neighbours Elisa Genthner and Annemarie Lange who always enriched my workday with their energetic personalities. The shared lunchtime and talks about science, rabbits and life in general will always be enjoyable memories. On this note, also a special thank you to Kai Richler for keeping up with us.

Additionally I want to thank the members of the Wegener group for providing all sorts of support with 3D laser microprinting, especially Pascal Kiefer, Jannis Weinacker and Sebastian Kalt. You definitely deserved more than the few cakes in return for your help.

I also want to thank Jan Fricke and Michela Stortigagi for their great work during their theses. Thank you for letting me use your data in this dissertation. It was a pleasure supervising and discussing your work.

Furthermore, I want to thank Nicolai Schäfer, Pascal Kiefer, Felix Jung and Kai Weißenbruch for proofreading my thesis. Your constructive comments and keen eyes in spotting the tiniest typos were highly appreciated!

I want to thank the Cluster of excellence 3DMM2O for supporting my work and providing me with the opportunity to connect with other researchers, as well as putting my scientific communication skills to the test during the Science Days.

As (part-time) colleagues and mostly dear friends, I want to thank Elisa Genthner and Pascal Kiefer for always being at my side. Both of you really helped getting my mind off work - be it at the gym or relaxing on the sofa. Although it now takes more effort than hopping on a bike to meet, I promise to still bother you with my presence.

Lastly, I want to thank my family for their undying support. Having a second place to call home and being welcomed at at any time means a lot to me. Finally, I want to thank my partner Felix Jung from the bottom of my heart for always having my back and being my never-ending resource of calmness. I am deeply grateful that chemistry brought us together, although I tried to get as far away as possible from it. Without you, this journey would not have been possible for too many reasons to list them all. I look forward to enjoying the next chapter together.